Ignition Capability of CO_2 in Hybrid Rockets for Mars Ascent Vehicles

by

Ozan Kara

A Dissertation Submitted to the
Graduate School of Sciences and Engineering
in Partial Fulfillment of the Requirements for
the Degree of

Doctor of Philosophy

in

Mechanical Engineering

KOÇ ÜNİVERSİTESİ

March 29, 2021

Ignition Capability of CO_2 in Hybrid Rockets for Mars Ascent Vehicles

Koç University

Graduate School of Sciences and Engineering

This is to certify that I have examined this copy of a doctoral dissertation by

Ozan Kara

and have found that it is complete and satisfactory in all respects,
and that any and all revisions required by the final
examining committee have been made.

Committee Members:

_____

Assoc. Prof. Arif Karabeyoğlu

_____

Prof. Dr. Metin Muradoğlu

_____

Prof. Dr. Ísmail Lazoğlu

_____

Prof. Dr. Onur Tunçer

_____

Assoc. Prof. Murat Çelik

Date: _____

To my family,

To the Future Martians

ABSTRACT

Ignition Capability of CO_2 in Hybrid Rockets
for Mars Ascent Vehicles
Ozan Kara
Doctor of Philosophy in Mechanical Engineering
March 29, 2021

CO_2 is a major combustion product arises from the combination of carbon as the fuel and oxygen as the oxidizer. However, CO_2 can burn with metallic powders that makes it interesting compound for the combustion applications. Metals have high reactivity levels compared to carbon thus breaks the carbon oxygen bond. This reaction releases significant amount of energy. Although $Metal/CO_2$ combustion has been studied by many researchers, process has not been evaluated for practical rocket applications. Therefore, this thesis aims to understand the ignition characteristics of the CO_2 in hybrid rocket motors. Propellant combination of $Paraffin/Metal/N_2O/CO_2$ is selected to accomplish the combustion.

Preliminary experiments are performed by using lab-scale hybrid motors. In addition, a scale up motor is used to better understand the ignition capability of the CO_2. Micron sized aluminum and magnesium is casted within the paraffin wax as the additive. Motor operating in "blowdown" mode uses N_2O/CO_2 oxidizer mixture in saturated liquid state. Results indicate that magnesium has better ignition capability with CO_2 than aluminium. The maximum successful combustion is achieved up to 75% CO_2 by weight percentage in the oxidizer mixture for 60% Mg by mass in the paraffin wax. CO_2 slows down the chemical kinetics thus adiabatic flame temperature has significant role on ignitibility limit. Ignitions are quenched at T_{flame} below 1600 K for scale up motor.

$Paraffin/Mg/N_2O/CO_2$ propellant combination is a feasible candidate for Mars Ascent Vehicles. In-situ CO_2 and Mg usage for propulsion systems significantly reduces mass that is needed to brought from the Earth. Although high level of CO_2 seems more efficient for in-situ MAV, the minimum mass is needed to be brought from the Earth is found at 60% CO_2 80% Mg propellant combination.

ÖZETÇE

Doktora Tez Başlığı
Ozan Kara
Makina Mühendisliği, Doktora
29 Mart 2021

CO_2, yakıt olarak karbonun ve oksitleyici olarak oksijenin kombinasyonundan kaynaklanan önemli bir yanma ürünüdür. CO_2 bir yanma ürünü olmasına rağmen sadece metalik tozlarla yanabilir ve bu özellik CO_2 'i yanma uygulamaları için ilginç kılmaktadır. Metaller, karbona kıyasla yüksek reaktivite seviyelerine sahiptir, bu nedenle CO_2 'deki karbon oksijen bağını kırarlar ve önemli miktarda enerji açığa çıkarır. $Metal/CO_2$ yanması bir çok araştırmacı tarafından çalışılsa da pratik roket uygulamaları için yeterince değerlendirilmemiştir. Bu nedenle, bu tez hibrit roket motorlarında CO_2'in yanma karakteristiğini anlamayı amaçlamaktadır. Yanmayı gerçekleştirmek için $Parafin/Mg/N_2O/CO_2$ yakıt kombinasyonu kullanılmıştır.

İlk testler laboratuar ölçekli hibrit motor kullanılarak yapılmıştır. Ek olarak, CO_2 'in ateşleme kapasitesini daha iyi anlamak için büyük ölçekli motor kullanılmıştır. Katkı maddesi olarak parafin mumu içine mikron boyutlu alüminyum ve magnezyum eklenir. Motor " blowdown " modunda çalışan doymuş sıvı halde N_2O/CO_2 oksitleyici karışımı kullanır.

Sonuçlar, magnezyumun alüminyumdan CO_2 ile daha iyi yanma özelliğine sahip olduğunu göstermektedir. Parafin mumunda kütlece $60\% Mg$ için oksitleyici karışımında ağırlıkça yüzde 75% CO_2 'a kadar maksimum başarılı yanma elde edilir. CO_2 kimyasal kinetiği yavaşlatır, bu nedenle adyabatik alev sıcaklığı yanma limiti üzerinde önemli bir role sahiptir. Ateşlemeler, büyük ölçekli ateşlemelerde 1600 K'nin altındaki T_{flame} 'da sönmüştür.

$Parafin/Mg/N_2O/CO_2$ yakıt kombinasyonu, Mars Kalkış Araçları (MAV) için uygun bir adaydır. İtki sistemleri için yerinde CO_2 ve Mg kullanımı, Dünya'dan getirilmesi gereken kütleyi önemli ölçüde azaltır. Yerinde MAV için yüksek CO_2 seviyesi daha verimli görünse de, Dünya'dan getirilmesi gereken minimum kütle 60% CO_2 80% Mg itici kombinasyonunda bulunur.

ACKNOWLEDGMENTS

I would like to express my deepest gratitude to my advisor, Assoc. Prof. M. Arif Karabeyoglu bringing me to this project. His support, guidance and insights in rocket field have always inspired me during my thesis project. I am extremely grateful to work with him.

In addition, I take this opportunity to thank my thesis jury members; Prof. Dr. Metin Muradoğlu, Prof. Dr. Onur Tunçer, Prof. Dr. İsmail Lazoğlu and Assoc. Prof. Dr. Murat Çelik. Their supports and interest on my project encouraged me to present my research better.

I would like to say a special thank you to my colleagues in DeltaV Space Technologies Inc., Hakkı Karakas and Mehmet Kahraman. We have made many discussions on how to improve hybrid rocket technologies in our PhD studies. I would particularly acknowledge some of my colleagues who helped me to improve my rocket motor test bench; Kutlay Hanlı, Bertan Kaynaroğlu and Mikail Tanrikuli. Their supports on control and data acquisition systems have made a great contribution to this project. Above ground, I would like to thank my special collegue Miray Karpat for supporting me during the experiments. Her dedication to her work inspired me during this project.

Furthermore, special thanks to technicians in DeltaV Space Technologies due to their contributions such as fuel machining, and test bench improvements; Ersin Solmaz, Erkan Solmaz, Cengiz Uygun, Erol Özdemir, Tuncay Duman, Yasir Barış Çelebi, Hasan Sönmez, and Tarık Tiryaki. Last but not least, thank you all Kebap based restaurants around test facility. They saved our lives after tiring experiments!

We are all experiencing the COVID-19 pandemic. This study is also conducted during the pandemic. The activity I had the most fun apart from this thesis during

the pandemic was playing Minecraft with my valuable friend Hüseyin Fırat Güldür. Thank you so much for sharing your time with me during quarantine days. We definitely have an architect spirit in Minecraft! In addition, there are two significant people I would like to specially thank; Umuralp Kaytaz and Yashar Esmaelian. I can write another PhD thesis with the memories we have shared. You are like brother to me.

In addition, Special thanks to KOC University Drop-in Volley community. We have had many enjoyable volleyball games together. Hour after hour! I would like to share special thanks to my good friend Ali Şardağ. It was pleasure to play volleyball with you!

From the bottom of my heart I would like to say big thank to my family; My father Ekrem Kara, my mother Songül Kara, my sister Damla Nur Kara and my uncle Erdoğan Kara. Thank you for supporting me spiritually throughout writing this thesis and my life in general.

TABLE OF CONTENTS

LIST OF TABLES

LIST OF FIGURES

ABBREVIATIONS

CAD	Computer Aided Design
CCP	Condensed Combustion Product
CEA	Chemical Equilibrium Analysis
DAQ	Data Acquisition System
DOF	Degree of Freedom
HEM	Homogeneous Equilibrium Model
HTPB	Hydroxyl-Terminated Polybutadiene
HTPE	Hydroxyl-Terminated Polyether
LOX	Liquid Oxygen
MAV	Mars Ascent Vehicle
MHRM	Mars Hybrid Rocket Motor
MMT	Mars Motor Test
NIST	National Institute of Standards and Technology
NPT	National Standard Pipe Thread
PCT	Propellant Characterisation Test
PMMA	Poly methylmethacrylate
PE	Polyethylene
A_{inj}	Injector hole area
A_{th}	Nozzle throat area
A_{port}	Fuel port area
Az	Initial azimuth
a	Regression rate coefficient
C_F	Thrust coefficient

c_d	Injector discharge coefficient
c^*_{exp}	Experimental characteristic velocity
c^*_{theo}	Theoretical characteristic velocity
D	Drag force
d_f, d_i	Final and Initial fuel port diameter
d_{th}	Nozzle throat diameter
d_{vc}	Fuel grain port diameter at valve closing (at thrust termination)
E	Relative error
E_A	Activation energy
E_{df}	Relative error due to final port diameter
E_{dvc}	Relative error due to thrust termination
E_{gox}	Relative error due to oxidizer mass flux
E_{Mox}	Relative error due to oxidizer mass flow rate
E_{reg}	Relative error due to regression rate
E_{prop}	Released energy per kg of propellant
$f_{R,T}$	Sensitivity coefficients
$\dot{G}_{ox}$	Oxidizer mass flux
h	The target altitude
$\Delta\hat{H}_{f@25℃}$	Heat of formation at $25°C$
I_{sp}	Specific impulse
i	Inclination
L	Fuel grain length
La	Initial Latitude
$\dot{m}_f,\ \dot{m}_{ox}$	Fuel and oxidizer flow rates
Δm	Difference between initial and final fuel grain masses

MW	Molecular weight
M_{f_i}	Initial fuel grain mass
M_{f_f}	Final fuel grain mass
M_{ox_i}	Initial oxidizer mass
M_{ox_f}	Final oxidizer mass
$M_{ox_{fac}}$	Final actual oxidizer mass
M_{bo}	Burn-out mass of the rocket
$M_{initial}$	Initial rocket mass
ΔM_{ox}	Difference between initial and final oxidizer masses
n	Mass flux exponent
n_m	Mole number
n_s	structural mass ratio
N_{inj}	Number of injector holes
O/F	Oxidizer to fuel ratio
P_{ch}	Motor chamber pressure (injector downstream pressure)
P_{inj}	Injector upstream pressure
P_{tank}	Oxidizer tank pressure
$\overline{P}_{ch}$	Average motor chamber pressure
$\overline{P}_{tank}$	Average tank pressure
$\overline{P}_{N_2O}$	Average nitrous oxide pressure
$\overline{P}_{CO_2}$	Average carbon dioxide pressure
$\overline{\Delta P}$	Tank and chamber pressure difference
R_{mars}	Radius of Mars
R_p	Radius of Metal Powder Particle

$r_{i,},\ r_f$	Initial and final fuel grain port radius
$\dot{r}$	Regression rate (burn rate)
$\dot{r}_{SP1}, \dot{r}_{SP7}$	Regression rate values of SP1 and SP7 fuels
T	Thrust
T_{tank}	Oxidizer tank temperature
T_{flame}	Adiabatic flame temperature
t_{av}	Average test time
t_{burn}	Ignition burn time
t_f	Thrust termination time
V_{feed}	Volume of the oxidizer feed system
V_M	Rotation Velocity of the planet
V_M^m	Mars velocity factor
Q_R	Heat of reaction (released energy)
$\hat{Q}_c$	Heat of formation of products minus reactants
ΔV_{del}	Delivered delta-V
ΔV_{rot}	Rotational delta-V
ΔV_{req}	Required delta-V
ΔV_{pot}	Potential energy delta-V
ΔV_{drag}	Drag delta-V
ΔV_{co}	Orbital velocity

α	Mass fraction used in Mars Vehicle Optimization
α_{TVC}	The thrust vector angle
ϵ	Structural mass ratio used in Mars Vehicle Optimization
γ	Ratio of the specific heats
γ_{tvc}	Trajectory angle with respect to local horizon
η	Mass ratio used in Mars Vehicle Optimization
η_{comb}	Combustion efficiency
η_{nozzle}	Nozzle efficiency
μ_{mars}	Gravitational constant of Mars
υ_{CO_2}	Specific volume of carbon dioxide
υ_{N_2O}	Specific volume of nitrous oxide
$\overline{v}_{liquid}$	Specific volume of the liquid oxidizer mixture
ρ_{CO_2}	Density of carbon dioxide in saturated liquid state
ρ_{N_2O}	Density of nitrous oxide in saturated liquid state
ρ_f	Fuel density
$\overline{\rho}_{liquid}$	Density of oxidizer mixture in liquid state
τ_{fs}	Characteristic timescale of the feed system
χ	Mass fraction

Chapter 1

INTRODUCTION

Mars is known to have the most suitable geological features and atmospheric conditions for the future human spaceflight. Based on the data from orbiters and rovers sent through deep space, Mars has the most active volcanic mountains and the highest impact craters of all the planets. Strong evidences via rover measurements moot that liquid water may have poured across the surface of Mars billions of years ago [1]. The latest dynamical models for the formation and evolution of the solar system support the water formation on the Red Planet. A recent study on Mars crater chronology focuses on the Jezero crater's dark terrain by using radioactivity measurements [2]. Jezero is the landing site of the Mars 2020 Perseverance rover. This updated model put forward that ancient water activities can be hundreds of millions of years older than previously thought. A recent study by Galofre [3] emphasizes that valley networks are formed by glacial erosion under the surface of the Mars. They used principal-component-based analysis with several erosion based models. They analyzed that valley formation was formed by water melting not by free-flowing rivers as previously thought. There is also evidence of methane leakage between rocks. Curiosity rover detected high methane concentration during the northern spring [4]. This may be an indication of microbial life just like on Earth.

Furthermore, the location of Mars smooths the way of long-term human spaceflight. Mars is relatively close to Earth compared to other possible planets that may be explored such as Saturn and Jupiter. Venus is closer candidate however it has very harsh atmospheric conditions. High temperature, high density and corrosive nature of environment makes surface of the Venus challenging to survive. Detailed

features of the Mars as a potential candidate for two-way human spaceflight can be found in NASA's Mars Exploration program [5].

Although Mars is considered as the best candidate for human exploration, there are some challenges during a two-way mission. Mars atmosphere has a density of 0.014 kg/m^3 and pressure of 610 Pa at the surface level. Low atmospheric density indicates that if Mars have had liquid water on its surface, it would have been evaporated immediately. In other words, the atmospheric pressure of Mars should be increased in order to capture water molecules in atmosphere (above the 6.25 kPa; The Armstrong Limit). The Armstrong Limit is a crucial factor for the human body. At 6.25 kPa, water boils at human body temperature. Breathable oxygen cannot be delivered to body more than a few minutes. Body fluids such as saliva, urine, tear, and alveoli in the lungs would boil away without a special pressurized body suit [6]. According to the NASA [7], increasing the atmospheric pressure to 19 kPa, would allow humans to sustain on Martian surface without a pressurized suit. Astronauts would only need to wear an oxygen mask. The value of 19 kPa corresponds the 1/5 th of the pressure on Earth at sea level.

Human spaceflight to the Red Planet takes at least 18 months with at least six months stay on the surface. Therefore, Martian air vehicles are needed both for surface operations and to return to the Earth. Mars has a hundred times thinner atmosphere compared to Earth. The low density and low Reynolds number of the atmosphere indicates that only air vehicles such as micro helicopters or gliders can operate on Mars's atmosphere [8, 9]. However, these vehicles can only be used for observation purposes and are not feasible for transportation of large payloads. An advanced propulsion system is needed to fulfill mission requirements for long term two-way missions.

Current propulsion systems are quite expensive and technologically not feasible to fulfill two-way mission. In-situ Resources Utilization (ISRU) technologies are required for low cost and practical propulsion systems. Both air breathing and rocket engines can be used as an ISRU based system. However, air-breathing engines need extremely large inlet areas due to the low atmospheric pressure of the Red

Planet. Moreover, the condensed phase combustion products make the turbojet engine impractical. All these circumstances make rocket propulsion systems more practical for Martian operations. And chemical rockets are more convenient for ISRU based propulsion systems [10]. Chemical propulsion systems are classified into three group due to propellant storage types; solid, liquid and hybrid propulsion [11, 12]. Hybrid propulsion offers safe, reliable, non-hazardous and cost-effective system compared to both liquid and solid systems. Hybrids can also operate at really low temperatures that features makes hybrids quite practical for Martian operations. Details of hybrid propulsion system advantages over solids and liquids are explained in Chapter 2.

This thesis aims to design in-situ propellant using hybrid rockets on Mars. Propellant combination is based on CO_2 and metal additives as in-situ propellant source. Using carbon dixode as an oxidizer is quite promising since 96% of Mars atmosphere consist of CO_2. Martian soil consist of Mg and Al that can be used as fuel grain additive. The performance of propellant design is analyzed by actual hybrid motor experiments. In addition, experiments present the ignition characteristics and flammability limit of the CO_2 with paraffin/metal fuel mixture. Because, carbon dioxide is known as a natural combustion product. It has also fire extinguisher feature. However, CO_2 can burn with metallic powders. High free energy level of metallic powders realises combustion with the carbon dioxide. Metals have higher reactivity series (with oxygen) than the carbon. Therefore, metals remove the carbon oxygen bond in CO_2.

In this thesis, two types of hybrid rocket motors are used. Primary experiments are performed using a small scale rocket motor. Then, scale up tests are evaluated for performance analysis. Small scale experiments are classified as PCT (Propellant Characterisation Test). Scale up experiments are presented as MMT (Mars Motor Test). Both rockets use circular port paraffin wax based fuel. Paraffin is used as major binder with metallic additives. It is difficult to ignite pure carbon dioxide (in saturated liquid state) with metals. Therefore, mixed oxides of N_2O/CO_2 is used as the main oxidizer. Combustion process is as follows; nitrous oxide reacts with the

paraffin thus breaks the oxide layer of the metallic additive. Then carbon dioxide burns with metal to complete the combustion.

The fuel grain of the PCT motor has the following dimensions; 70 mm length, 15 mm inner diameter and 31 mm outer diameter. Paraffin/Aluminum mixture is the primary fuel. The motor operates with 200 grams of N_2O/CO_2 oxidizer mixture up to 50 grams/seconds flow rate [10]. PCT motor provides around 50 N of thrust. The MMT motor that is Mars Hybrid Rocket Motor (MHRM), consists of following dimensions such as 24 mm inner port diameter, 48 mm outer diameter and 180 mm fuel length. Micron sized spherical shape aluminum and magnesium powder are casted into the paraffin-based fuel. Motor uses N_2O/CO_2 oxidizer mixture with up to 250 grams per seconds flow rate. Thrust range is changing between 80 and 320 N.

Scale up experiments indicate successful combustion at %75 CO_2 by mass using magnesium-based fuel. Combustion capability is studied with averaged oxidizer mass flux versus CO_2 weight percentage in the oxidizer mixture. Increasing carbon dioxide fraction slows down the chemical kinetics. This makes the combustion unstable and the ignition quenches at a certain point. In addition, motor chamber temperature decreases from 3500 K to 1700 K due to carbon dioxide addition. Therefore, adiabatic flame temperature reduction is also discussed in this thesis. MHRM experiments also showed that Mg has better ignition capability with CO_2 than aluminum due to weak oxide layer and lower ignition temperature of 1000 K. In addition, In-situ mass optimization shows that Mg 80% CO_2 60% combination minimizes the mass is needed to taken from the Earth. It means that only 30% of total propellant mass is needed to brought from the Earth. Therefore $Paraffin/Magnesium/CO_2$ /N_2O propellant combination seems a feasible candidate for Mars Ascent Vehicles.

In this thesis, Chapter 2 explains fundamentals of hybrid rocket propulsion. Common fuel and oxidizer combinations are presented in detail. Advantages of hybrid systems over other chemical rockets are emphasized for Martian environment. Chapter 3 explains the propellant design and manufacturing. Oxidizer mixture process, metallic additive selection and fuel grain casting the major sections of Chapter

3. Thermochemical analysis of selected propellant is explained in Chapter 4 using NASA Chemical Equilibrium Analysis (CEA) software [13]. Optimum oxidizer to fuel ratio versus specific impulse values are plotted. Heat of reactions per kg of propellants are presented. Metal oxide formation is discussed in this chapter.

Designs of hybrid rocket motors are presented in Chapter 5. This chapter shows both lab scale motor and MHRM. CAD drawing and motor parts such as injector, nozzle and measurement devices are illustrated in this chapter. The complete test bench (feed line, plumbing, tanks and valves) is explained in detail. Process and Instrumentation (P&ID) diagram is shown. Derivations of the hybrid motor performance parameter such as oxidizer flow rate, specific impulse and regression rate are presented in Chapter 6. Related equations for motor ignition data analysis are explained in detail. Moreover, Chapter 7 illustrates the test results including the pressure time traces of motor ignitions. PCT results are explained at first. Then the scale up experiments are presented in detail. Scale up experiments include combustion boundary of CO_2 with respect to oxidizer mass flux. Adiabatic flame temperature is discussed to identify the "maximum flammability limit" of the carbon dioxide. Motor performance parameters such as regression rate and combustion efficiency are presented. The relative errors on motor ignitions are explained.

Chapter 8 includes literature survey for the Mars Ascent Vehicle propulsion systems. Performance of $Paraffin/Magnesium/CO_2\ /N_2O$ propellant combination is presented for a Martian Sounding Rocket. 2-DOF analysis results are briefly mentioned. In addition, O/F effect on rocket mass that is brought from the Earth is also discussed. Earth based mass minimization is the main objective of this research. Conclusion is presented as Chapter 9. The Future Work is explained in Chapter 10. Future work consists of internal ballistics improvements in order to achieve higher carbon dioxide mass fractions during the combustion.

Chapter 2

HYBRID ROCKET PROPULSION FUNDAMENTALS

This chapter provides fundamental information related to hybrid rocket propulsion. Hybrid rockets provide safety, reliability and environment friendly manufacturing compared to other conventional rockets. It stores propellants in separate phases as in Figure 2.1 [14]. Usually, the oxidizer is in liquid (or gaseous) phase and fuel is in solid phase.

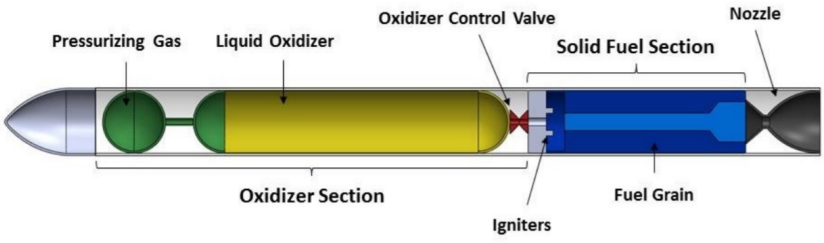

Figure 2.1: Hybrid Rocket Lay-out [14]

The oxidizer is stored inside an aluminum tank. The oxidizer is driven through a main valve into the solid fuel. An injector is used in order to control the oxidizer flow rate. Brass is the common material for the injector due to material properties. Brass is quite durable and resistant to high temperatures. The pressure of the oxidizer is regulated by a pressurization system. Helium gas is mostly used as the pressurizing agent. Composite is commonly used for the pressurizing tank manufacturing. There is an igniter which is placed near the injector manifold for initiating the ignition inside the motor. Igniter compounds mostly consist of potassium nitrate based solid pyrogen. However, larger rocket motors requires additional igniter motors as presented in [15]. Hybrid rocket motors mostly use circular port grain design. Circular port grains provide easy manufacturing and high regression rates [11, 15].

Combustion occurs inside the grain port by the oxidizer flow and eventually exits through the nozzle. Nozzle throat diameter is designed in order to provide particular chamber pressure inside the motor. Graphite is mostly used for the nozzle. There are wide range of propellants available for hybrid rockets. Available propellants provide economical, simple and safe solutions compared to other propulsion systems.

This chapter presents propellant types for hybrid rocket motors. Chemical and physical features of propellants are briefly discussed.

2.1 Hybrid Propulsion History

Hybrid rocket studies date back to 1930s. In 1933, Russian engineers Sergei Korolev and Mikhail Tikhonravov developed the first hybrid rocket as 2.4 meters long and 0.17 meter diameter. They built gelled gasoline/LOX type rocket with a thrust of 500 N for 15 seconds. In 1937, Leonid Andrussow developed 10 kN hybrid motor by using coal and gaseous nitrous oxide in Germany. However, this study resulted in failure due to the high heat of sublimation for carbon. Hermann Oberth also worked on LOX based hybrid rockets. Oberth used graphite as the fuel [16, 17].

The mid-1940s witnessed the flight of hybrid rockets. California Pacific Rocket Society performed LOX based tests using wood, wax-filled carbon black and rubber based fuels. Their rocket successfully flew to 9 km altitude in 1951 by using rubber/LOX propellant. In addition, General Electric (GE) Company studied hybrids by using hypergolic propellants in the 40s and 50s. GE focused on polyethylene as the fuel and hydrogen peroxide as the oxidizer. Their fuel grain had uniform burning without pressure spikes as in liquid engines. Fuel surface acts as flame holder that creates stable combustion. On the other hand, low burning rates and thermal instability were the two significant issue during the combustion [16, 17].

NASA participated in hybrid motor studies in 1960s. NASA sponsored United Technologies Corporation (UTC) to develop high energy motors. UTC worked on target drone project was named as Sandpiper in 1968. Sandpiper used MON-25 (mixed 25% NO, 75% N_2O_4) as the oxidizer and polymethyl methacrylate (PMM)/Mg mixture as the fuel. Drone achieved 160 km altitude in 300 seconds. The improved

version of Sandpiper was named as HAST PB/PMM/IRFNA propellant with O/F ratio of 10. Furthermore, Chemical Systems Division (CSD) developed similar rocket to HAST in 80s. CSD used hydroxyl-terminated polybutadiene (HTPB)/Fluorine propellant. However, they casted lithium in HTPB and oxygen in flourine (FLOX) to increase the energy content of the motor. Motor diameter was 1.07 meters and had 11-port wagon wheel grain configuration. Successful burn was achieved with 93% combustion efficiency. Specific impulse was 380 seconds [17].

In 60s, two significant institutes in Europe were working on hybrid rockets; ONERA in France and Volvo Flygmotor in Sweden. ONERA used amine/nitric acid propellant. They performed 8 tests between 1964 and 1967 with the flight range of 100km. Volvo also performed two successful flights by using nitric acid in their hybrid rocket. They used Tagaform as the fuel. Tagaform is a mixture of aromatic amine and polybutadiene (PB). Volvo achieved 80 km altitude in 1969 and loft 20 kg payload [17].

Americam Rocket Company (AMROC) developed the largest hybrid rockets ever manufactured in the late 80s and early 90s. The first version of their rocket used $HTPB/LOX$ and produced 312 kN of thrust for 70 seconds. The second version of their rocket called as H-250F with one millions of thrust value [17].

Environmental Aeroscience Corporation (eAc) fired first gaseous oxygen and rubber hybrid rocket in 1982. Korey Kline was the pioneer engineer in eAc. In addition, eAc developed Hyperion Sounding Rocket using $HTPB/N_2O$. Hyperion rocket achieved an altitude of 36.5 km. It was the first rocket that used self-pressurizing oxidizer. Lockheed Martin also flew with $HTPB/LOX$ based rocket through an altitude of 71 km with 267 kN [17].

In 1994, US Air Force Academy flew hybrid sounding rocket to 5 km altitude. The rocket was 6 meters long and used $HTPB/LOX$. The thrust value was 4400 Newtons for 16 seconds [17].

2.1.1 Commercial Companies

SpaceDev (Sierra Nevada Corporation's Space Systems) was the first company performed over 200 hybrid motor firings in the 90s [18]. SpaceDev acquired all patents of AMROC related to hybrid rocket rocket testing, manufacturing and performance analysis. SpaceShipOne was the first private manned spacecraft produced by Scaled Composites. SpaceShipOne used $HTPB/N_2O$ that was developed by SpaceDev. Unfortunate explosion of SpaceShipOne killed three people in the development phase of the propulsion system in 2007. Virgin Galactic took over the flag with SpaceShipTwo as commercial suborbital spaceplane.

SpaceDev developed launch vehicles which are called Streaker and DreamCheaser. Both system use nitrous oxide as the oxidizer and HTPB as the fuel. In 2009 Sierra Nevada Corporation acquired the SpaceDev and developed hybrid rocket motors for SpaceShipTwo. In addition, U.S. Rockets company developed $HTPB/Nitrous$ based rockets. They also developed H_2O_2 86% and HTPB/Al hybrids.

Space Propulsion Group (SPG) is founded in 1999, the company is based in Sunnyvale, California [19]. SPG aims to be a global market leader and trusted partner offering world-class, reliable and innovative solutions in hybrid propulsion. They had successfully launched $Paraffin/LOX$ and $Paraffin/N_2O$ rockets.

Hybrid propulsion systems has been considered an option for low cost launch vehicles. Many other companies are founded as recently to make the space more affordable and accessible.

Rocket Lab is one of the significant companies that is founded in 2006 [20]. They've developed two rockets Electron and Neutron. Electron is 18 m long and 1.2 m in diameter. Electron is a two stage system with Kerosene/LOX propellant. First stage has 190 kN lift-off thrust with 311 seconds I_{sp}. The second stage operates in vacuum environment with 25.8 kN thrust and 343 seconds of specific impulse. It can transfer 200 kg payload to the Low Earth Orbit (LEO). Neutron rocket has the first launch date of 2024. Neutron will be 40 m long, 4.5 m in diameter. Rocket Lab. aims to make reusable first stage for the Neutron. It planned to provide 8000 kg to LEO and 1500 kg to the near by planets such as Venus or Mars.

Gilmour Space Technologies is developing nitrous oxide based systems with wax-HTPB mixture. Orbitec is another company that developed "Vortex Hybrid" concept. Rocket Crafters Inc. (RCI) performed over 40 experiments with STAR-3D engine in Florida. RCI used 3D printed ABS (Acrylonitrile butadiene styrene) plastic fuel with nitrous oxide (in liquid phase). The Reaction Research Society (RRS), Comphenhagen Suborbitals, and blueShift Aerospace are other start up companies in the hybrid rocket field. T4i is an Italian company also working on hybrids. Furthermore, TiSpace (from Taiwan), HyImpulse (from Germany) and DeltaV Space Technologies (from Turkey) are developing Paraffin/LOX hybrid sounding rockets.

2.1.2 University Contributions

Stanford University has done some of the pioneering work in this field. At Stanford, Arif Karabeyoglu and Brian Cantwell founded Space Propulsion Group in 1999. They developed high regression rate liquefying fuel which is paraffin wax. They worked with NASA Ames Research Center to develop Peregrine sounding rocket for 100 km altitude.

University of Tennessee Knoxville collaborated with NASA Marshall Space Flight Center for component development in hybrid rockets. They developed water-cooled 3-D printed nozzle and 3-D printed green ABS fuel.

Delft Aerospace Rocket Engineering (DARE) group developed and launched Stratos II sounding rocket in 2015. Stratos II had paraffin/nitrous propellant including aluminum powder in the fuel grain.

Many other universities are also working in hybrid motors such as Florida Institute of Technology, Boston University, University of Utah, University of California, Purdue University, Technical University of Munich, Brigham Young University, University of Brasilia, University of Toronto, University of Calgary, Istanbul Technical University, University of Padua, University of Stuttgart, and TU Graz.

A detailed list of commercial companies and universities is found in the literature [12, 15].

2.2 Hybrid Propulsion Advantageous

This section presents hybrid propulsion system advantages over solid motors and liquid engines. Operation feasibility at low temperatures, long oxidizer storage capability with non-hazardous manufacturing make the hybrids more practical for Mars missions.

In the solid rocket motors, oxidizer and fuel are mixed as single solid phase. Combustion occurs by heating the solid fuel grain to reach the ignition temperature. Ignition of solid fuel cannot be stopped when it is started thus causes explosive danger. Thrust cannot be adjusted in solid motors that additional control systems are required for the rocket.

Liquid motors keep the oxidizer and the fuel in separate tanks that combustion occurs by mixing propellant in a combustion chamber. Intimate mixture of propellant in a single chamber may cause explosion hazard. Propellant storage also requires exceptional cooling system in pumps, feed system and nozzle.

Hybrid rocket motors, however keeps oxidizer in liquid phase and fuel in solid phase [11, 12]. The hybrid burning creates turbulent diffusion flame where the oxidizer-to-fuel ratio varies down the length of the chamber.

Oxidizer delivery system (by using single oxidizer tank) reduce the complexity of plumbing compared to liquids. The ignition can be throttled by a main valve unlike solid motors. Hybrids have inert solid fuel grain; the grain manufacturing is safer than solid motors. Besides, it is easy to cast metallic additives in fuel grains to improve the combustion performance.

2.3 Hybrid Propulsion Propellant Evaluation

Classical hybrid rockets commonly use polymeric fuels such as PB (polybutadiene) monomers such as PB–acrylonitrile (PBAN) and PB–acrylic acid (PBAA), PMMA Poly(methyl methacrylate), PE (Polyethylene), HTPB (Hydroxyl-Terminated Polybutadiene), HTPE (Hydroxyl-terminated polyether), Plexiglas (Lucite) and metatoluene diamine/nylon. In hybrid motors, a turbulent boundary layer is formed

by oxidizer injection over the polymeric fuel surface [12]. Thus, the diffusion flame occurs during the ignition at the boundary layer. Diffusion flame is transported on the surface by oxidizer flow. Radiation and convection heat transfer play an important role during this process. Thereby, vaporized fuel on the grain surface reacts with atomized liquid oxidizer causing "blocking effect" at the wall. This blocking effect limits the burn rate of the motor [12]. This phenomena is based on Marxman diffusion limited model [Marxman]. Heat transfer limited theory is developed by Marxman, Gilbert, Wooldridge, and Muzzy during the 1960s.

Paraffin wax is another fuel commonly used in hybrid motors. Karabeyoglu performed several significant studies related to the combustion theory of the paraffin wax [21, 22]. Karabeyoglu stated that burning paraffin fuel produces a liquid layer over the fuel grain with low viscosity and low surface tension [21]. The liquid melt layer consists of liquified paraffin fuel droplets. This layer merges with the oxidizer flow becomes hydrodynamically unstable in the fuel port. Unstable ignition creates an instability; it lifts-off paraffin fuel droplets from the grain surface that foster the mass transfer rate of fuels into the oxidizer gas flow. This is called as "liquid entrainment mass transfer mechanism".

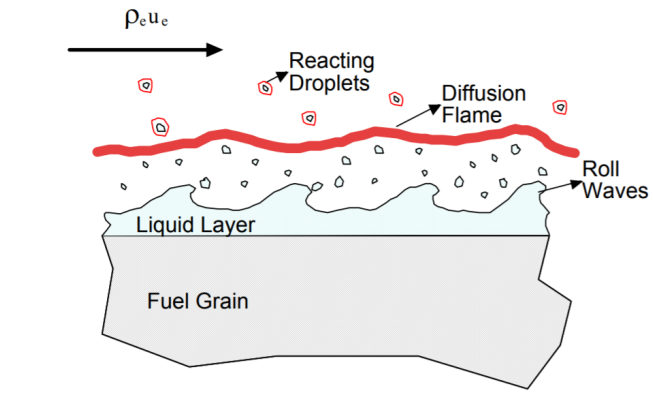

Figure 2.2: Paraffin Wax Liquid Entrainment Mechanism [22]

Figure 2.2 shows the "liquid entrainment mass transfer mechanism" for the paraffin wax [22]. Entrainment mass transfer is an additional physics to the classical gasification mechanism. Droplet entrainment dominates gasification, thus it is not

affected by the blocking phenomena during the combustion. Entrainment mass transfer mechanism shows that paraffin enables 3 to 5 times higher regression rate at the same oxidizer mass flux compared to classical polymeric fuels [21, 22]. Specific burning area of droplets leads to the increased regression rate. In addition, pyrolysis of paraffin based fuels is another factor for high regression rate. Paraffin wax based fuels melt above 40℃ thus droplet evaporation fosters the combustion. Convective heat transfer is less impeded than it is with classical hybrid fuels. This means that the blocking effect is lower compared to non-liquefying fuels.

Detailed analysis of the liquid layer hybrid combustion theory for pentane, paraffin wax and polyethylene are presented in Karabeyoglu [22].

Hybrid rockets commonly use N_2O_4 (dinitrogen tetraoxide), H_2O_2 (hydrogen peroxide), gaseous (GOX) or liquid oxygen (LOX) and N_2O (nitrous oxide) as the oxidizer [23]. Nitrogen tetraoxide is storable high-density oxidizer that is used in early launch vehicles. N_2O_4 provides moderate I_{sp} with performance additives. However, it's a highly toxic chemical. Hydrogen peroxide is also a storable and high-density agent. H_2O_2 is an aggressive chemical at high concentrations. It has leaning to self-decompose, thus causes detonation hazard. Typical rocket applications use over 80% concentration levels of H_2O_2 that makes the distillation and handling quite critical for human skin. Liquid oxygen is the most common high-performance oxidizer in the rocket industry. LOX is highly stable due to diatomic oxygen bond and provides high specific impulse. It provides lower oxidizer to fuel ratio that reduces the fraction of oxidizer used in the propulsion system. It is also cost-effective compound. However, LOX is cryogenic material with boiling temperature of 90 K. Cryogenic nature of LOX makes it challenging during surface operations on the Mars. It requires complex plumbing and valve systems as well as advanced insulation systems. Moreover, liquid oxygen is not self-pressurizing agent due to its low density and it needs an additional pressurization system via Helium or Nitrogen. This increases complexity and the cost of a possible Martian rocket.

Nitrous oxide is another agent that has been used mostly in small rocket systems. Nitrous oxide has self-pressurizing capability at saturated liquid state [10, 23].

Self-pressurization eliminates the need of pressurizing system to feed the oxidizer. Thus, it reduces the complexity, weight and cost of the propulsion system. Self-pressurization feature also makes nitrous aoxide n efficient candidate for Mars environment. N_2O is non-toxic and easy to handle compared to N_2O_4, H_2O_2 and LOX. Nitrous oxide also creates a highly exothermic decomposition reaction during the combustion. Therefore, it provides stable and efficient ignition in the rocket systems. Nitrous oxide in liquid phase is quite safe and easy to store at room temperature. Highly storable feature makes launch operations quite easy compared to other oxidizer options. Also, it is readily available in chemical industry. On the other hand, reduced specific impulse, low density at higher temperatures and strong dependence of the temperature are among the several disadvantages of N_2O. It should be noted that N_2O has a positive heat of formation. Thus, self-decomposition of "vapor phase" N_2O in feed lines, oxidizer tank and combustion chamber result in disruptive damage [24].

2.4 CO_2 as a Novel Oxidizer Agent

Carbon dioxide is known as a natural combustion product from hydrocarbons or explosions. However, metals have high free energy that can burn with carbon dioxide. Metals can remove the carbon-oxygen bond in the CO_2. That is to say metals have higher reactivity series compared to carbon thus removes the carbon oxygen bond. This reaction produces a substantial energy release. Various metals and metal hydrides have been studied in order to understand the combustion characteristics of carbon dioxide as explained in [10, 25, 26, 27].

Kara and Karabeyoglu [10] provides practical experiments using CO_2 as the oxidizer in lab scale hybrid motors. CO_2 is mixed with the nitrous oxide to understand the combustion characteristics. Paraffin based fuel consist of 40% aluminum powder by mass. The aluminum powder has 3 micron spherical shape. Al has two purity levels 98.75% and 99.99%. The purity level has no significant effect on carbon dioxide combustion. According to [10], successful combustion is achieved up to 45% by mass in the oxidizer mixture. In his comprehensive study, Boiron [25] ex-

plains the in-situ resources utilization techniques for hybrid propulsion based Mars Ascent Vehicles. Boiron promotes high performance liquid oxygen/paraffin based hybrid rocket system. He proposes two concept missions; Mars Sample Return (36 kg payload mass) and Medium-scale (500 kg payload) Rocket. Borion explains background on in-situ propellant production techniques and uses electrolysis methods. He discusses advantages and disadvantages of Paraffin/Aluminum/O_2/CO_2 propellant combination for Martian rockets. Finally, Boiron presents details of Zirconia cell hardware and electrochemical mechanism. Other fundamental studies related to carbondioxide combustion are studied by Shafirovich, Gokalp and Zubrin [26, 27]. Shafirovich and Gokalp presents the concept of a metal/carbon dioxide propellant for Mars Sample Return missions. They provide a detailed thermochemical analysis of CO_2 combustion with various metals and metal hydrides in rockets. In addition, they provide lab scale combustion experiments with magnesium. Shafirovich and Gokalp compares several designs for their ascent/decent vehicle such as hybrid engine, liquid monopropellant engine and bipropellant engine. Robert Zubrin who is one of the pioneer scientists in the field of Mars missions proposes diborane and silane for Mars Ascent Vehicles.

Although there are many theoretical studies on $Metal/CO_2$ combustion, it has not been tested an actual hybrid rocket motor. There is an experimental study on combustion characteristics of carbon dioxide with magnesium rocket engines. Yue Lie uses magnesium fuel in powder form with multiple gas injection mechanisms into the combustion chamber at high pressures [28]. Yue presented the thermodynamic calculations for the combustion process of the multiphase flow environment in a lab scale rocket engine used in the experiments. However, this design seems impractical that gas phase oxidizer needs pressurizing system to create high levels of motor chamber pressures.

Chapter 3

PROPELLANT DESIGN AND MANUFACTURING

This chapter explains the manufacturing process of paraffin/metal based propellant. Paraffin is the main binder in the fuel. Fuel grain consists of metallic powder additives in order to accomplish carbon dioxide combustion. Aluminum and magnesium powders in micron sizes are used in the fuel grain. Advantages of both compounds over other possible metallic powders are explained in detail. Main suppliers for metal powders are explained. The unit cost of the fuel per experiment is also stated.

This chapter also explains the mixing process of N_2O/CO_2. Both compounds are stored in saturated liquid state. Nitrous oxide and carbon dioxde have similar physical properties with respect to temperature or pressure. In other words, both compounds have almost same density (or specific volume) due to particular pressure or temperature level. Physical properties of oxidizers are taken in NIST database [29].

It is worth to note that both N_2O and CO_2 demonstrate two-phase flow characteristics. Therefore, calculation of the discharge coefficient and the oxidizer mass flow rate is a sensitive process. So, this chapter explains the fundamentals of the two-phase flow.

3.1 Metallic Additives Evaluation

Metallic powders serve as excellent fuel additives due to their significant volumetric and gravimetric heat release during the combustion process [23]. Purity, size and shape of metallic powders directly affect the combustion performance as they control the ignition delay and the formation of the condensed combustion product (CCP). High purity compound makes the ignition easier. Small sized metal powder (such

as nano size) reduces ignition delay in the motor. Flake shaped powder has larger surface area than spherical shape that also provides easier ignition.

Wide range of additives have been studied for CO_2 combustion in rocket motors such as lithium (Li), boron (B), berillyum (Be), aluminum (Al), magnesium (Mg), magnesium hydride (MgH_2), diborane (B_2H_6) and silane (SiH_4). Lithium is highly reactive alkali metal, however it shows low volumetric heat release (means low specific impulse) due to its low density. Boron is commonly used as a solid propellant additive. Even tough it has high combustion energy per unit mass, it delivers poor combustion efficiencies. Major concern of boron is that it reveals high CCP in the nozzle. Magnesium hydride increases specific impulse, however not practical for longer lifetime missions due to its poor dehydrogenation kinetic and hydrogen storage. Casting and lifetime are major issue for all other metal hydrides.

Figure 3.1 shows the theoretical specific impulse values with respect to oxidizer to fuel ratio. Figure is taken from the [30]. Calculations are made by [30] with 10 bars of chamber pressure.

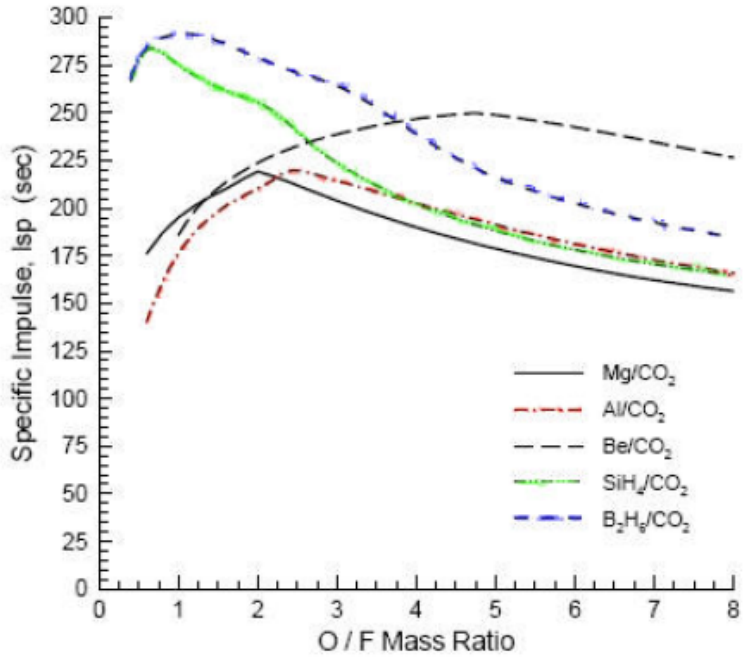

Figure 3.1: O/F Ratio versus Specific Impulse – Various of Additive

Diborane is storable at 5 bars in Martian conditions. Diborane produces high mass fraction of CCP that reduces the specific impulse. Boron oxide formation in liquid form generates a significant risk for slag formation in the nozzle throat. Decomposition is another factor for diborane. Silane has silicon oxide as the major CCP. It provides lower mass fraction of CCP than diborane. However, silane is quite toxic there is not enough reliable data for SiH_4/CO_2 combustion [25, 26].

Therefore, analysis shows that beryllium, aluminum and magnesium are the most prominent candidates for carbon dioxide combustion due to performance and safety aspects. Beryllium is extremely toxic despite its high performance. All in all, magnesium and aluminum are left as major additives that can be casted with the paraffin wax.

3.2 Aluminum Particle Combustion in CO_2 Regime

Aluminum is low cost and widely used in micron/nano sized powder form. Aluminum combustion in carbon dioxide environment reveals alumina (Al_2O_3). Alumina is not in gas phase. However, Al produces several gas phase oxides. Al particle (droplet) combustion involves several gas phase reactions on the droplet surface. Thus, a liquid oxide cap occurs in Al surface during the burning. CO_2 makes Al droplet combustion complicated compared to oxygen and air [31]. For the Al/CO_2 environment, if both agents are initially at 298 K, the T_{flame} is similar to Al boiling temperature at 1 atm. Adiabatic flame temperature becomes less than Al boiling point if pressure increases to 5 atm [31]. This creates thinner flame zone and surface reactions have significant role on the combustion. Process of Al particle combustion in CO_2 is as follows; carbon occurs in the particle surface. Then carbon dissolves in liquid Al. Droplet size decreases and carbon concentration reaches the saturation limit. Either carbon or aluminum oxycarbide layer covers the particle surface. Thus, Al vaporization is blocked.

Figure 3.2 shows the Al combustion mechanism in various of environments. Figure is taken from [31]. Al/O_2 combustion has distinct feature compared to CO_2 environment. Adiabatic flame temperature is much higher than the Al boiling point

at any pressure level. This makes vapor-phase reactions dominant at the particle surface.

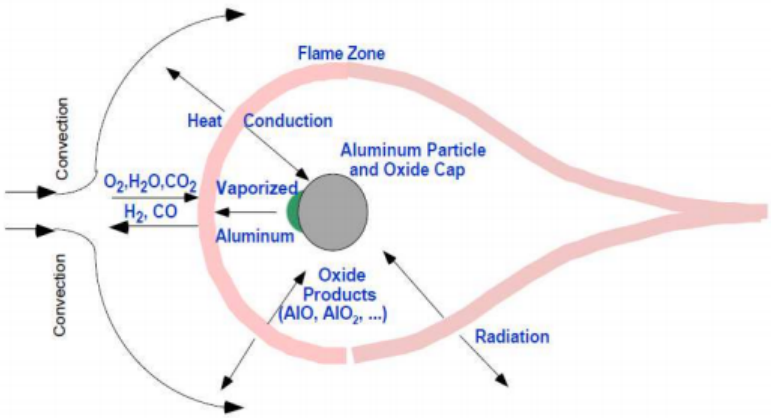

Figure 3.2: Al Particle Combustion Mechanism in CO_2

The particle size is a significant factor influencing the combustion characteristics. As the particle size decreases, combustion gets from diffusion to kinetic controlled regime. For Al/CO_2, combustion is controlled by diffusion for more than 200 micron sizes [31]. No pressure effect is observed during the combustion. However, kinetics of reactions on the particle surface is dominant below 80 micron size.

The major drawback of Al is the high ignition temperature with the carbon dioxide environment. Micron scale Al must be at least 2000 K to accomplish the combustion in CO_2 environment, whereas Mg has 1000 K ignition temperature with carbon dioxide. Ignition temperature becomes a critical factor for high CO_2 environments as studied in this thesis. For CO_2 based hybrid systems, the igniter of the motor should provide at least 2000 K to initiate the ignition. Stable ignition is needed using hybrid propulsion system for in-situ Mars applications.

In addition, both spherical and flake shaped aluminum can be casted easily within paraffin wax. Aluminum provides high specific impulse with the CO_2. However, Al/CO_2 combustion produce severe slag formation resulting in nozzle blockage due to alumina (Al_2O_3) formation.

Shafirovich and Varna [31] presented several improvements for Al/CO_2 combus-

tion. Using Nickel coated Al could be one method. Ni reacts with the Al at high temperatures. Exothermic reaction between Ni layer and Al core triggers the ignition at 1600 K, rather than the 2000 K. Another method could be using nano sized aluminum. Nano sized Al reduces the ignition temperature, ignition delay time and solid oxide (also called as condensed combustion product) formation.

3.3 Magnesium Particle Combustion in CO_2 Regime

Magnesium has been considered the most promising compound for CO_2 combustion. It has larger heat per unit mass of fuel. It shows rapid ignition characteristics in carbon dioxide environment due to its low ignition temperature of 1000 K. Low toxicity of Mg is another factor that it is chosen as the main candidate for Martian applications [32]. It is also found broadly in the market with low cost.

Shafirovich conducted several experiments with Varna and Goldshleger [31, 33] with spherical particles around 2 mm in diameter. They observed that the ignition occurs if CO_2 temperature is higher than Mg melting point of 923 K. They performed thermogravimetric analysis that slow heteregeneous combustion regime at temperature range of 950 K. The ignition leads a fast vapor-phase combustion at higher temperature regimes. A well-developed flame zone occurs at Mg particle surface.

Shafirovich observed that Mg/CO_2 combustion mechanism forms a porous solid shell that is almost the same size as the initial particle. This shell consist of MgO and carbon. Carbon formation near the particle surface is due to the thermodynamic analysis in the vapor-phase flame zone. Shafirovich presents that the thermodynamics of Mg/CO_2 allows carbon to be formed by Mg-CO reaction at low temperatures (at the particle surface). It is worth to note that reducing the Mg particle size produces combustion above the Mg boiling point, thus reduces the carbon formation.

In addition, Yuasa and Isoda [34] studied combustion of large Mg disks in CO_2 atmosphere. They showed that Mg had easy ignitability and faster combustion rates than other metallic particles in CO_2 environment.

The combustion mechanism of Mg in CO_2 atmosphere is shown in Figure 3.3 [34].

The combustion is defined as a quasi-state diffusion controlled mechanism. In this model, two separated chemical reactions occur simultaneously. The first reaction is $Mg + CO_2 \rightarrow MgO + CO$. This is between Mg vapor and CO_2 in gas phase. The second reaction occurs near the surface between Mg and CO. This heterogeneous reaction occurs as $Mg + CO \rightarrow MgO + C$.

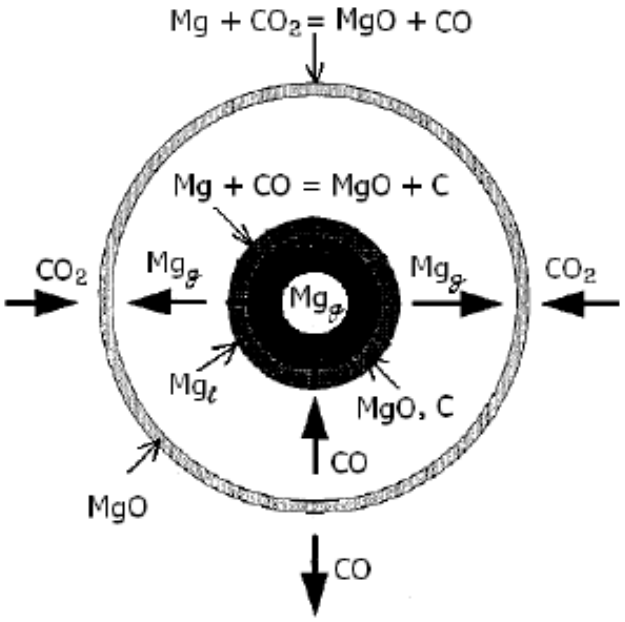

Figure 3.3: Mg Particle Combustion in CO_2

CO mass transfer is a significant factor for the combustion. Heat release in both reactions play an important role in the process of metal droplet evaporation during CO_2 combustion [31].

In Figure 3.3, carbon dioxide diffuses toward the spherical Mg droplet that reacts with Mg vapor that diffuses away from the particle. At the same time, the second heterogeneous reaction occurs. Thus, as CO occurs CO_2 mass fraction decreases.

Following, CO diffuses both towards the surface and away from the surface through the infinity as seen in Figure 3.3.

Diffused carbon monoxide at the droplet surface reacts with the Mg. This het-

erogeneous reaction forms carbon and MgO in condensed form. According to [34], the reaction mechanism of Mg/CO_2 is presented in Figure 3.4. In this table, details of empirical parameters A, β and E_A are given in [34]. Unit of E_A is in calories per mole. Unit of A is in $(cm^3/gmol - s)$. β is a constant.

Reaction	Reaction no.	A	β	E_A
$Mg + CO_2 = MgO + CO$	11	2.00E+14	0.0	34847.0
$Mg + CO = MgO + C$	12	2.00E+11	0.0	30000.0
$Mg + O_2 = MgO + O$	1	4.44E+12	0.5	30500.0
$Mg + O + M = MgO + M$	2	1.90E+14	0.5	0.0
$MgO = MgO(l)$	3	6.11E+11	−2.0	17268.6
$MgO(l) = MgO(s)$	4	1.00E+15	0.0	0.0
$2O + M = O_2 + M$	5	1.89E+13	0.0	−1788.0
$CO + O + M = CO_2 + M$	13	6.02E+14	0.0	3000.0
$CO + O_2 = CO_2 + O$	14	2.50E+12	0.0	47800.0
$C + O_2 = CO + O$	15	5.80E+13	0.0	576.0

Figure 3.4: Reaction Mechanism for Mg/CO_2

Briefly, metal oxide layer of a magnesium powder sphere is not strong as in aluminium that is easily breakable during combustion. Therefore, magnesium oxide (MgO) formation by Mg/CO_2 reaction is not as severe as in aluminum oxide. It shows less particle agglomeration and two-phase losses in the nozzle compared to the Al/CO_2 combustion.

3.4 Metallic Powder Additives Selection

Lab-scale motor experiments (PCT) use spherical shaped aluminum casted up to 40% by mass in the paraffin. Scale up tests (MMT) use both aluminum and magnesium are used for experiments. 3-micron spherical shape aluminum has 99.99% purity level. Spherical shaped aluminum is casted up to 40% by mass in the paraffin. In addition, flake shaped aluminum powder is also tested. Combination of 20% flake 40% spherical aluminum-based fuels have higher carbon dioxide concentration during the combustion. Surface area of flake shape is larger than spherical shape.

Larger surface are makes the combustion easier. Magnesium powder is 44-micron and has 99.99% purity level. Mg amount in paraffin is 60% by mass.

3.5 Metallic Powder Suppliers

Nanokar [35] is the main supplier for metallic powders. Flake shaped aluminum is bought from the Egenanotek [36]. Table 3.1 shows the price and properties of metallic powders.

Table 3.1: Metallic Powder Suppliers and Properties

Supplier	**Size (μm)**	**Purity (%)**	**Price $/kg**
Nanokar	3 Al	98.75, 99.99	20, 66
Egenanotek	3 Al flake	99.99	250
Nanokar	44 Mg	99,99	5

In scale up experiments, overall mass of the 40% Aluminum 60% Paraffin fuel grain is 280 grams. That means 112 grams aluminum powder and 168 grams of paraffin. The cost of paraffin wax is $3/kg. Therefore, it corresponds 2.74 dollars per fuel grain. 60% Mg and 40% Paraffin formulation is 300 grams and it costs 1.3 dollars per grain.

3.6 Fuel Grain Manufacturing

Paraffin wax ($C_{32}H_{66}$) is the main binder of the solid fuel grain. Hydrophobic nature of the paraffin protects the metal additives from water vapor. It is nontoxic thus produces water and carbon dioxide as the combustion products. Paraffin has low glass transition temperature ($-180℃$) that is quite feasible for colder periods of Mars atmosphere. Also, inert feature of the paraffin wax is feasible for long duration Mars missions.

Mixing metallic powders up to 40% by mass is achieved using Silverson L5M

high shear mixer [37]. High shear mixer uses square shaped blades. Mixing metal additive with paraffin binder is as follows,

- The required quantity of pure paraffin wax is heated and liquified through a beaker. Then, desired structural additives are added in the paraffin wax
- Paraffin based formulation mixed again with the High Shear Mixer for 2 minutes at 5000 rpm in order to provide a homogeneous mixture.
- The required quantity of metallic powder is added to the molten paraffin fuel
- Silverson L5M High Shear Mixer at 6000 rpm is used to mix powders uniformly in the molten paraffin at 120℃ for 5 minutes to ensure homogeneity
- Liquid binder/additive mixture is casted axially into a phenolic mold that is kept around 80℃. Thus the fuel grain is allowed for cooling to room temperature. The cooling process takes around 5 hours.
- Finally, fuel grain is machined to the intended circular port and outer diameters.

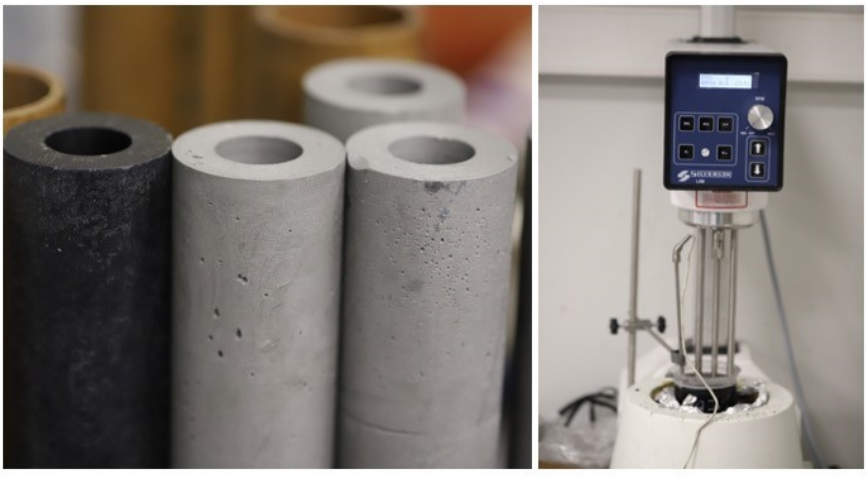

Figure 3.5: Fuel Samples and Silverson L5M High Shear Mixer

Figure 3.5 shows several fuel samples that are casted by using the L5M High Shear Mixer. It is worth to note that, although high shear mixer allows homogenous mixture of paraffin and metal powders, increasing magnesium amount to 60% cannot be casted by using high shear mixer due to high viscosity. The structure of 60% magnesium 40% paraffin mixture is like mud that only be casted by hand-mixing in a phenolic mold.

3.7 Fuel Grain Quality

Paraffin wax has a density of approximately 920 kg/m^3 in the solid phase. Magnesium density is 1738 kg/m^3 and aluminum has a bulk density of 2700 kg/m^3, that both are significantly denser than the paraffin. Theoretical density of metal powder (aluminum or magnesium for this thesis) loaded fuel is calculated using Eq. 3.1 χ_{par} *and* χ_{me} are the mass fraction of paraffin and metal in the mixture. ρ_{par} *and* ρ_{Me} are densities in kg/m^3.

$$\rho_{fuel} = \left[\frac{\chi_{par}}{\rho_{par}} + \frac{\chi_{me}}{\rho_{me}}\right]^{-1} \tag{3.1}$$

Theoretical density of 60% magnesium 40% paraffin fuel is obtained as 1282 kg/m^3. Measured densities of casted grains are 1203 kg/m^3 on average means 6.5% of error obtained in the casting process. The density error of 40% aluminum-based fuels are 2%. This is because higher metal powder addition makes the casting process harder. Thus it directly affects the uniformity.

In addition, uniformity of axially casted grains are determined using "piece by piece density measurement" technique as follows; (i) the casted fuel is cut into three main pieces as top, middle and bottom, (ii) densities of three parts of the fuel grain are measured to evaluate the metallic powder settling in the paraffin wax fuel. The overall density variation between pieces in grain sections is 20 kg/m^3 that is acceptable for our testing purposes.

Particle drop time in the liquid paraffin is a significant factor for the grain quality. Stoke's law is used to determine the drop rate by Eq. 3.2. The ρ_p is particle density and ρ_{fuel} is theoretical fuel density in kg/m^3. In addition, g is the gravitational acceleration in m/s^2. R_P is the metallic particle radius in meters. The dynamic viscosity of the molten fuel (metal/paraffin mixture) is μ_{fuel} in centipoise (cP).

$$v_p = \frac{2}{9} \times \frac{(\rho_p - \rho_{fuel})}{\mu_{fuel}} g R_p^2 \tag{3.2}$$

Particle drop rate of aluminium and magnesium particles in the molten paraffin wax are presented in Table 3.2.

Table 3.2: Metallic Particle Drop Rate in Molten Paraffin

Additive	Additive % by weight	$R_P; \mu m$	$\rho_{fuel},\ kg/m^3$	$\mu_{fuel},\ cP$ @ 75℃	$v_p,\ mm/h$
Mg	40	44	1133	230	9.72
Al	40	3	1250	220	0.117

Magnesium 60% Paraffin 40% fuel grain quality is verified by using thermogravimetric analysis (TGA). Figure 3.6 shows the TGA of the grain samples.

Perkin Elmer TGA4000 [38] is used with following settings (i) holding the grain sample at 50℃ for one minute, (ii) heating the sample between 50℃ and 550℃ with 5℃/min, (iii) holding the sample 2 minutes at 550℃ and (iv) heating the excess sample up to 900℃ with 5℃/min [34]. Three samples are analyzed by TGA presented in Figure 3.6. Sample masses are around 30 milligrams. First sample is pure paraffin wax that nitrogen gas decomposes paraffin completely around 500℃. Upper and side sections of magnesium casted samples are also analyzed. 38% of samples in weight percentage decomposes around 500℃. That means 62% of sample mass corresponds to the excess magnesium in the sample. TGA verifies the accuracy of the axially casting method.

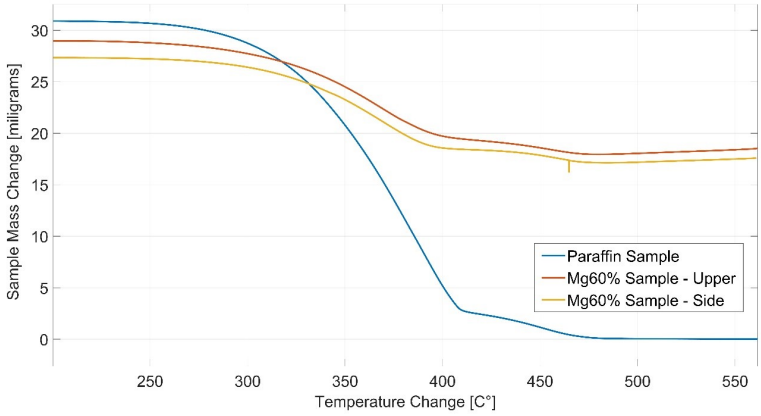

Figure 3.6: Mg Mass Fraction Change within the Paraffin Wax

3.8 Oxidizer Mixing Process

Hybrid rocket motor experiments use CO_2 /N_2O oxidizer mixture in blowdown mode. Self-pressurizing capability of both oxidizers makes Martian operations quite practical. The mixture displays several advantages such as (i) improved I_{sp} performance compared to pure CO_2 , (ii) decreased two-phase losses due to reduced mass fraction of condensed phase products (CO_2 allows additional burning with the condensed phase species), (iii) low freezing point of the oxidizer mixture is ideal for Martian environment (iv) both agents has self-pressurizing feature that they don't require any additional pressurizing system in the rocket, (v) low cost, less complicated and lighter compared to liquid bipropellant engines.

Uniform mixture of N_2O and CO_2 is achieved due to similar fluidic characteristics of two agents. Table 3.3 summarizes physical characteristics that is taken from the NIST database [29].

Table 3.3: Saturation Properties of N_2O and CO_2

T_{tank}, ℃	P_{tank}, *bar* N_2O	P_{tank}, *bar* CO_2	ρ_{N_2O} kg/m^3	ρ_{CO_2} kg/m^3	υ_{N_2O} m^3/kg	υ_{CO_2} m^3/kg
0	31.21	34.85	909	927	0.0011037	0.0010782
5	35.40	39.69	884.28	897.26	0.0011354	0.0011160
10	39.99	45.01	856.48	863.64	0.0011735	0.0011613
15	45.03	50.87	824.11	823.33	0.0012185	0.0012177
20	50.55	57.29	785.27	772.28	0.0012737	0.0012930
25	56.60	64.35	737.61	705.05	0.0013460	0.0014075
30	63.25	72.10	678.29	614.56	0.0014533	0.0016855

Figure 3.7 and Figure 3.8 explains the thermophysical properties due to temperature change. Uniform mixture of the two compounds is physically viable for the experiments.

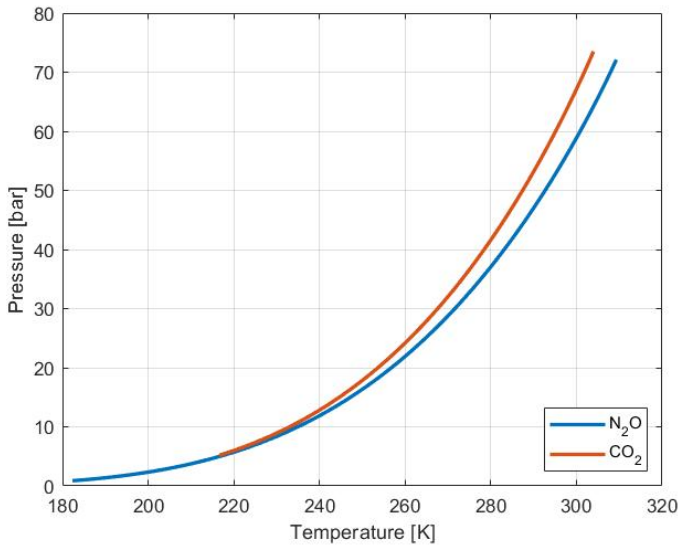

Figure 3.7: Pressure versus Temperature in Saturated Liquid State

Figure 3.7 shows the pressure versus temperature correlation of N_2O and CO_2

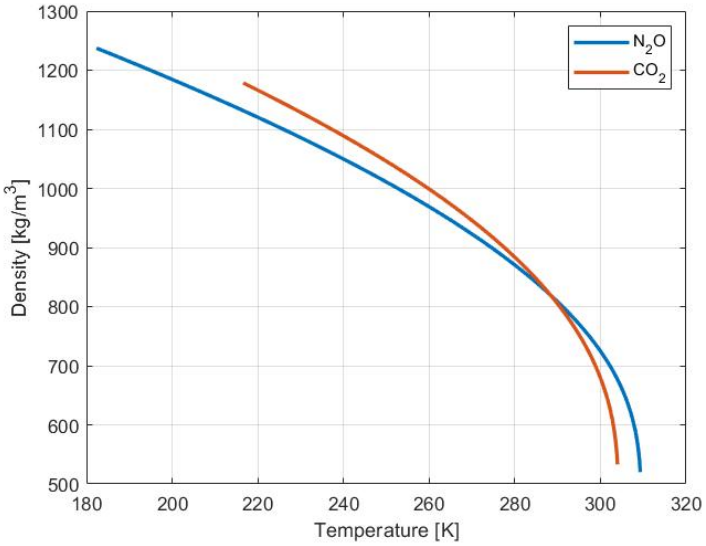

Figure 3.8: Density versus Temperature in Saturated Liquid State

in saturated liquid states. Figure 3.8 shows the density versus temperature of N_2O and CO_2 in saturated liquid states.

Mixing two self-pressurizing saturated liquids requires a careful process. Therefore, oxidizer tank has the safety factor of 6. PCT (lab scale) experiments uses 200 grams of oxidizers mixture. Mixture operates at around 50 bars. N_2O and CO_2 requires sensitive scales.

MMT (scale up) experiments use 10 liters aluminum scuba tank with maximum operating pressure of 200 bars as the main oxidizer tank. The oxidizer compound that has higher mass fraction is first filled in the scuba tank. Then, the tank is vented to cool the oxidizer and, to reduce the tank pressure to around 30 bars. The reduced tank pressure allows second oxidizer (source tank that has higher pressure) compound to be added to the scuba tank. Therefore, the second oxidizer compound is then added to the main tank.

Saturation properties of liquid N_2O and CO_2 are calculated by using NIST database as explained in Figure 3.7 and Figure 3.8. Saturation properties are saved in the text format and read into Matlab to perform a 5^{th} order polynomial curve fitting.

For example, oxidizer mixture density is the major parameter for the performance analysis of the ignition. Eq. 3.3 calculates the specific volume of the mixture with respect to mass fractions. υ_{N_2O} and υ_{CO_2} are found from Figure 3.7 and Figure 3.8. χ is the mass fraction of the nitrous oxide in the oxidizer mixture.

$$\overline{v}_{liquid} = \upsilon_{N_2O}\chi + \upsilon_{CO_2}(1-\chi) \tag{3.3}$$

Then the overall oxidizer density is calculated, by assuming an ideal mixture, using the simple formula,

$$\overline{\rho}_{liquid} = 1/\overline{v}_{liquid} \tag{3.4}$$

Liquid N_2O and CO_2 mixture operates in blow-down mode during the experiments. The oxidizer mixture has two-phase flow characteristics in the feed system through the injector. The oxidizer flow is choked at the injector, thus the downstream pressure (motor chamber pressure) has no effect in the flow rate. Figure 3.9 verifies this by showing the injector pressure versus oxidizer flow rate distribution.

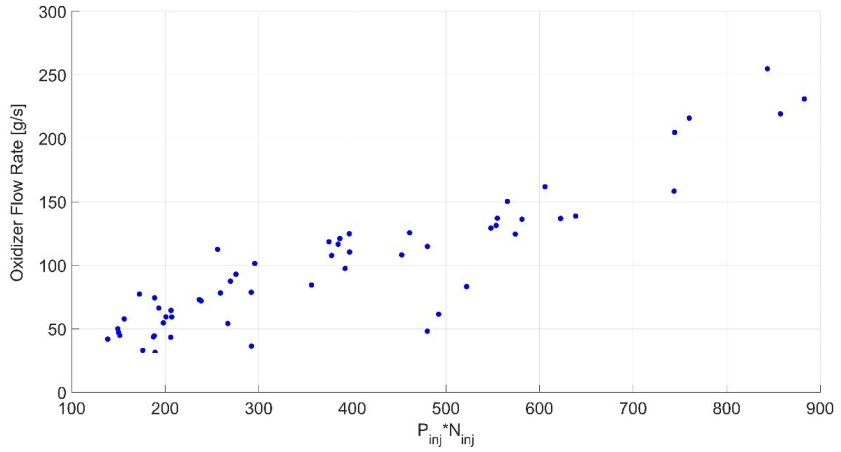

Figure 3.9: Oxidizer Flow Rate Increase by the Upstream Pressure

In Figure 3.9, x- axis shows the overall upstream pressure ($\bar{P}_{inj}$) multiplied with the injector hole number (N_{inj}). Y-axis shows the oxidizer flow rate of all MMT experiments. Figure 3.9 clearly shows that the oxidizer flow is choked at the injector.

Motor chamber pressure has no effect on the discharge coefficient and the flow rate calculations.

A blow-down oxidizer mixture needs an advanced approach by using two phase physics. Because, self-pressurizing N_2O or CO_2 in saturated liquid state cannot be modelled by using fundamental ideal gas, compressible or incompressible flow assumptions. Two phase flow approaches by using Homogeneous Equilibrium Model (HEM) is needed for more precise calculations on flow rate and discharge coefficient. Many researchers have studied the two phase flow characteristics of nitrous oxide [39, 40, 41, 42].

However, two-phase flow approach is neglected in this thesis. The incompressible flow approach is used for the oxidizer characterization (especially discharge coefficient). Equations are explained in Chapter 5. An advanced two-phase flow analysis will be the scope of the subsequent studies.

3.8.1 Two Phase Flow Background

Typical rocket applications require fluid dynamics calculations of the injector and propellant feed system. Most of the liquid propellants such as hydrogen peroxide (H_2O_2), ethanol (C_2H_5OH), RP-1 ($C_{12}H_{24}$) and nitrogen tetraoxide (N_2O_4) can be modelled accurately using classical incompressible fluid dynamics features. In addition, gaseous propellants such as gaseous oxygen, hydrogen and methane use ideal gas law and compressible fluid assumptions. Liquid oxygen (LOX) can also be modelled accurately. Although LOX is in a saturated state at cryogenic temperatures, it uses single-phase incompressible flow assumptions. Compressibility (Z) factor of liquid oxygen at 1 atm pressure is 0.004, and 0.97 for saturated cryogenic oxygen vapor. Both values are very close to ideal values 0.0 and 1.0 [40, 42].

Nitrous oxide however has a liquid Z factor of 0.13 and saturated vapor compressibility factor of 0.53 at the room temperature. Therefore, incompressible liquid or ideal gas assumptions become inaccurate for modelling nitrous oxide. N_2O is handled as a two-phase mixture for fluid flow modelling. Two-phase flow modelling means that fluid flows as a mixture of liquid phase and a vapor phase at the same

time. A fluid quality factor is required for the fluid flow. Fluid quality is the ratio of the vapor mass fraction divided by the total fluid mass.

Injector modelling of self-pressurizing agents such as nitrous oxide is a complex process [39, 40]. Because, fluid quality factor changes during tank evacuation; liquid phase boils into vapor phase. Therefore, internal tank pressure and fluid density change during the evacuation. Tank pressure and fluid density directly effects the hybrid motor performance. Because, these factors affects the injector mass flow rate calculations. Changing the mass flow rate directly effects the combustion stability and motor efficiency.

3.8.2 Two Phase Flow Literature Review

Mass flow rate characterization and modeling by using self-pressurized N_2O has been studied by many researchers in the hybrid rocket field [39, 40, 41, 42]. Solomon developed an engineering model to calculate the mass flow rate of N_2O [39]. Solomon used both incompressible and homogeneous equilibrium mass flow rate models in order to increase the accuracy of the mass flow rate with one dimensional approach. He used iterative process to track fluid properties such as enthalpy across the injector. He used isentropic or adiabatic assumptions.

Solomon also developed two-phase flow model for the CO_2. Because nitrous oxide and carbon dioxide has similar thermophysical features as explained in Table 3.3. He performed cold flow experiments by using the CO_2 to compare the analytical model. CO_2 is a non-energetic compound and it reduces the risk of explosion due to decomposition. It is low cost and quite proper to use in experiments.

Whitmore and Chandler developed two phase flow model of saturated N_2O feed systems [40]. Feed system of self-pressurized systems exhibit transient properties as the tank-fluid mass diminishes. Therefore, modeling tank evacuation becomes challenging. Whitmore and Chandler developed a simple engineering approach by using adiabatic expansion process during evacuation. Tank fluid entrophy changes during tank evacuation through the feed system. However, initial fluid entrophy become equal to the feed system entrophy at a certain time. Therefore, two-phase

non-homogeneous non-equilibrium process dominates the fluid flow process. Whitmore and Chandler calculated tank-fluid states continuously. They considered vent and evacuation of tank both in vapor and liquid phases. Results are supported with cold flow experiments in small scale hybrid rocket motor.

Another fundamental study is made by Stanford University and NASA Ames Research Center [41]. Dyer and his colleagues are performed thermodynamics and mass transfer kinetics in two-phase systems. They emphasized that the incompressible assumption is not valid for liquid phase and ideal gas assumption cannot be modeled for vapor phase. Therefore, they used fundamental Helmholtz energy function in order to predict two-phase injector flow relations. Pressure, density and temperature functions are significant parameters for Helmholtz energy function.

Waxman also emphesized the two-phase flow physics in hybrid rocket motors [42]. He presented theories of single-phase incompressible liquid flow, homogeneous two-phase flow and two-phase flow with non-equilibrium effects. Waxman studied effect of the injector design on discharge coefficient. He also compared oxidizer flow rate change versus supercharged N_2O and CO_2 pressures. He compared results with Dyer's work. Waxman concluded that the discharge coefficient (c_d) in the single phase region is inversely proportional to the injector hole diameter. In addition, critical flow occurs when the motor pressure falls below the oxidizer saturation pressure. Oxidizer mass flow rate can increase due to the injector design such as rounding or chamfering the inlet of the injector hole in machining.

Chapter 4

THERMOCHEMICAL ANALYSIS OF PROPELLANT COMBINATION

In this chapter, theoretical specific impulse with respect to O/F ratio is presented via NASA's Chemical Equilibrium Analysis (CEA) software [13]. CEA uses heat of formation, molecular weight and temperature values of molecules in analysis. Propellant combinations $C_{32}H_{66}/Mg/N_2O/CO_2$ and $C_{32}H_{66}/Al/N_2O/CO_2$ are discussed. Propellant combination includes heavy loading of metals such as aluminum and magnesium. Therefore, oxide formation (also called as condensed combustion product formation, CCP) after the combustion is crucial for motor performance. CCP formation can block the motor nozzle, thus combustion efficiency increases. Therefore, mass fractions of CCP formation is stated.

In addition, metal addition into the paraffin wax increases the heat of reactions of propellants. Released energies of per kg of propellant during the combustion is explained. Heat of reactions are calculated from heat of formations of each species. Energy values are presented due to optimum O/F ratio values. Optimum O/F value is the one that makes the adiabatic flame temperature (T_{flame}) maximum.

In this thesis, experiments indicate that the adiabatic flame temperature determines the flammability level of the carbon dioxide. Therefore, this chapter also presents the theoretical flame temperatures of various of propellant combinations due to the CO_2 mass fraction.

4.1 Theoretical O/F versus I_{sp}

Figure 4.1 shows the O/F *versus* I_{sp} for magnesium based propellants. Magnesium is loaded as 60% by mass. CO_2 mass fraction is 70% by mass in the oxi-

dizer mixture. Chamber pressure, combustion efficiency, and area ratio are taken as 38 *bars*, 0.98 *and* 50. Ambient pressure is selected as 0.006 bar which is Martian atmospheric pressure value.

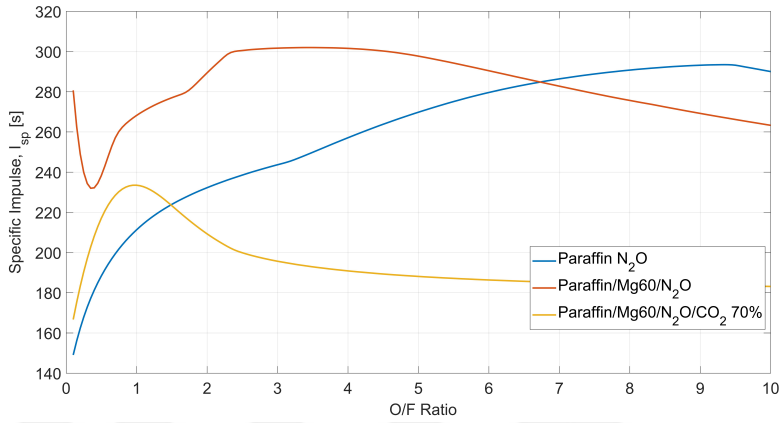

Figure 4.1: Specific Impulse versus O/F Ratio – Magnesium

Magnesium and carbon dioxide addition to propellant combination clearly reduces the O/F ratio. Carbon dioxide increase in nitrous to 70% shifts to O/F ratio throughout 1.1. Reduction in O/F has the advantage of lower oxidizer mass tank. This further reduces the required nitrous oxide mass brought from the Earth in a possible Mars Ascent Vehicle design.

Figure 4.2 shows the O/F *versus* I_{sp} for aluminum based propellants. Al mass fraction is 60% in the paraffin. CO_2 mass fraction is 70% in the oxidizer mixture. Chamber pressure, combustion efficiency, and area ratio are taken as 38 *bars*, 0.98 *and* 50.

Aluminum provides 10 seconds higher specific impulse than the Mg with the same motor pressure and combustion efficiency. Figures 4.1 and 4.2 show the difference of I_sp between two cases. It is worth to note that, although theoretical calculation assumes 98% combustion efficiency, Al/CO_2 based experiments show actual combustion efficiency of around 70%. Detailed data evaluation is given in Chapter 7.

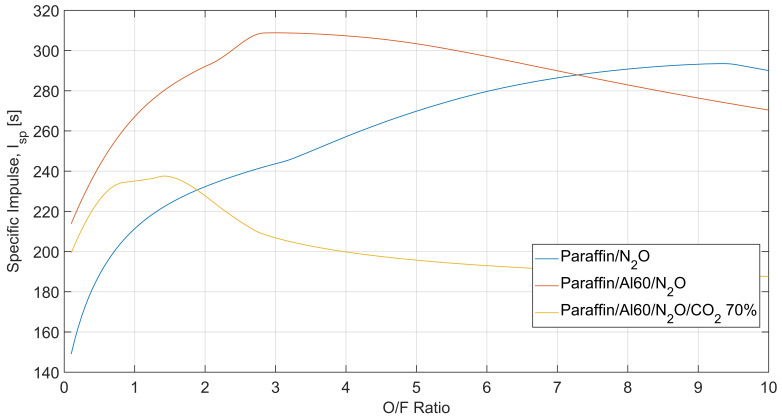

Figure 4.2: Specific Impulse versus O/F Ratio – Aluminum

4.2 Condensed Combustion Product Formation

This section presents mass fractions of condensed combustion products. PCT experiments uses 40% aluminum. MMT experiments uses both 40% aluminum and 60% magnesium. CEA analysis show theoretical values of oxide formation during the combustion. CEA uses 38 bars motor pressure and area ratio of 1.

Table 4.1 shows aluminum cases with respect to various O/F ratio and CO_2 percentage by mass. Aluminum oxide formation is above 55% at O/F ratio of 1. This makes the rocket ignition challenging and low performance. Increasing oxidizer to fuel ratio reduces the oxide formation. Oxide formation decreases by half at O/F ratio of 3. Further decrease on CCP is achieved at O/F ratio of 5. CCP formation is only 12% of products. However at this O/F ratio, 20% of CO_2 is obtained in products. High O/F reveals unburned carbon dioxide in the rocket.

Table 4.1: CCP Formation of Aluminum Cases

*Al*40	30% CO_2			50% CO_2			70% CO_2		
$\overline{O/F}$	1	3	5	1	3	5	1	3	5
CCP Fraction	0.55	0.19	0.12	0.57	0.19	0.12	0.61	0.20	0.12

Table 4.2 shows Mg cases with respect to various O/F ratio and CO_2 mass fractions. Magnesium oxide and carbon formation increases as the CO_2 increases at the optimum O/F value of 1. This reduces the specific impulse and thrust values of the rocket. Oxide formation drastically decreases as the O/F increases. CCP falls by half at O/F value of 3. At this level, 25% of combustion products involves magnesium oxide.

Table 4.2: CCP Formation of Magnesium Cases

$Mg60$	30% CO_2			50% CO_2			70% CO_2		
$\overline{O/F}$	1	3	5	1	3	5	1	3	5
CCP Fraction	0.44	0.23	0.13	0.52	0.25	0.16	0.58	0.25	0.17

At O/F value of 5, oxide formation is only 10% of the products. However, CO_2 cannot contribute the combustion at high oxidizer to fuel ratios. Although 10% of products are oxides, 30% of the products consist of unburned CO_2. Therefore, O/F value of 3 seem practical to have less oxide formation and good rocket performance.

4.3 Energy Analysis of Selected Propellants

Energy analysis is useful indicator of the propellant performance. The energy release due to the combustion is calculated by using heat of reactions (Q_R) of chemical compounds (products and reactants). Eq. 4.1 is the formulation for the heat of reaction (combustion) in kJ/kg for the specific propellant. In this equation, $\hat{Q}_c$ is the heat of formations of products minus reactants. n_m is the mole and MW is the molecular weight of propellants (reactants).

$$Q_R = \frac{\hat{Q}_c}{\sum (n_m \times MW)_{reactants}} \tag{4.1}$$

If $Q_R < 0$ the reaction is exothermic, and if $Q_R > 0$ the reaction is endothermic. In addition, $\hat{Q}_c$ is found by using Eq. 4.2. It refers the difference between total heat

of formations of products and reactants at $25°C$.

$$\hat{Q}_c = \sum_{products} \Delta\hat{H}_{f@25℃} - \sum_{reactants} \Delta\hat{H}_{f@25℃} \tag{4.2}$$

Energy analysis of various propellants are presented in Table 4.3. Energy released per kg of propellants is presented due to optimum O/F ratio. Optimum oxidizer to fuel ratio is taken for maximized T_{flame} by using CEA.

Table 4.3 shows the fuel additive and carbon dioxide mass fractions and released energy ($E_{prop} = Q_R$) per kg of propellant. Results are negative that means reactions are exothermic.

Table 4.3: Released Energy Values of Propellants

Propellant Type	Mass fractions	Optimum O/F Ratio	$T_{flame,max}$ K	E_{prop} kJ/kg
$C_{32}H_{66}/Mg/N_2O$	Mg60	4	3520	6603
$C_{32}H_{66}/Al/N_2O$	Al60	3.5	3850	8221
$C_{32}H_{66}/Mg/N_2O/CO_2$	Mg60 $CO_2$70	0.8	2350	5795
$C_{32}H_{66}/Al/N_2O/CO_2$	Al60 $CO_2$70	0.7	2550	5639
$C_{32}H_{66}/N_2O$	-	8	3263	5307

Table 4.3 indicates that aluminum provides 35 percent higher energy than magnesium in N_2O ignition. Furthermore, released energy of 70% CO_2 based propellant is almost same as $Paraffin/Nitrous$ propellant. This means that, although carbon dioxide slows down the chemical kinetics, it provides same energy level as $Paraffin/Nitrous$. Magnesium has significant effect on this combustion mechanism. In addition, Al and Mg provides similar heat of reaction for 70% CO_2. Al and Mg with carbon dioxide provides higher heat of reaction than 70% CO_2 based propellants.

Heat of reactions in Table 4.3 are calculated from the heat of reactions of each species as explain in Eq. 4.2. Thus, Table 4.4 shows the heat of formations of

significant molecules in solid (s), liquid (l) and gas (vapor) phases. Values are presented for $25°C$.

Table 4.4: Heat of Formations of Molecules

Molecule (phase)	Heat of Formation 25℃, $kJ/mole$
$C_{32}H_{66}$ (s)	-698
N_2O (l)	65
N_2O (g)	81.5
CO_2 (l)	-410.5
CO_2 (g)	-393.5
CO (g)	-110
H_2O (v)	-240
MgO (s)	-610.7

Two examples are presented for heat of reaction calculation. First example is the $Paraffin/N_2O$ chemical reaction.

$$C_{32}H_{66} + 81.81N_2O \rightarrow 15.19CO + 33H_2O + 81.81N_2 + 16.81CO_2 \tag{4.3}$$

Heat of formations are calculated as,

$$\begin{aligned}\hat{Q}_c = \ & 15.19\Delta\hat{H}_{f,\ CO} + 33\Delta\hat{H}_{f,\ H_2O} + 16.81\Delta\hat{H}_{f,\ CO_2} \\ & - \Delta\hat{H}_{f,\ C_{32}H_{66}} - 81.81\Delta\hat{H}_{f,\ N_2O}\end{aligned} \tag{4.4}$$

Thus, heat of reaction is found by using Eq. 4.5.

$$\hat{Q}_R = \frac{\hat{Q}_c}{450 + 81.81 \times 44} \times 1000 = -5307\ kJ/kg\ of\ propellant \tag{4.5}$$

Second example is $Paraffin/Mg/N_2O/CO_2$ chemical equilibrium which is presented in Eq. 4.6.

$$\begin{aligned}&C_{32}H_{66} + 28.12Mg + 20.45\,(0.3N_2O + 0.7CO_2) \rightarrow \\ &\quad 6.64CO + 33H_2 + 6.13N_2 + 28.12MgO + 39.67C\end{aligned} \tag{4.6}$$

Thus, heat of formation is found by using Eq. 4.7.

$$\begin{aligned}\hat{Q}_c = \; & 6.64\Delta\hat{H}_{f,\,CO} + 28.12\Delta\hat{H}_{f,\,MgO} \\ & - 14.31\Delta\hat{H}_{f,\,CO_2} - \Delta\hat{H}_{f,\,C_{32}H_{66}} - 6.13\Delta\hat{H}_{f,\,N_2O}\end{aligned} \tag{4.7}$$

Thus, energy released by the combustion is found by using Eq. 4.8.

$$\hat{Q}_R = \frac{\hat{Q}_c \times 1000}{450 + (28.12 \times 24) + (20.45 \times 44)} = -5795 \; kJ/kg \; of \; propellant \tag{4.8}$$

4.4 Adiabatic Flame Temperature Evaluation

Adiabatic flame temperature (motor chamber temperature) shows the combustion limit of the carbon dioxide. CO_2 slows down the chemical kinetics, thus reduces the T_{flame} inside the motor. At a certain T_{flame}, motor ignition quenches. Therefore, Table 4.5 and Table 4.6 shows the theoretical T_{flame} due to various CO_2 and oxidizer to fuel ratios. CEA is used for analysis with 38 bars of motor chamber pressure and area ratio of 1.

Table 4.5: T_{flame} of Aluminum Cases

$Al40$	30% CO_2			50% CO_2			70% CO_2		
$\overline{O/F}$	1	3	5	1	3	5	1	3	5
T_{flame}, K	2150	2290	2646	2141	1621	1956	1974	1233	1178

In Table 4.5, carbon dioxide addition slightly decreases the T_{flame} at $O/F = 1$. Increasing the oxidizer to fuel ratio causes further decrease in T_{flame}. Flame temperature decreases up to 1233 K at $O/F = 3$. Interestingly, $O/F = 5$ has higher flame temperature than O/F value of 3 for 30% and 50% carbon dioxide cases. However, temperature drops again at 70% carbon dioxide.

Magnesium shows higher flame temperature profile than the aluminum. Table 4.6 shows that T_{flame} has no change at $O/F = 1$. Increasing the oxidizer fuel ratio increases the temperature during the combustion. This means that Mg has better ignition capability with CO_2 compared to Al. 70% CO_2 point shows an interesting

Table 4.6: T_{flame} of Magnesium Cases

$Mg60$	30% CO_2			50% CO_2			70% CO_2		
$\overline{O/F}$	1	3	5	1	3	5	1	3	5
T_{flame}, K	2286	2937	2845	2270	2352	2502	2263	1633	2093

value. Flame temperature is lower at $O/F = 3$ compared to the $O/F = 5$. This means that rocket motor should not operate at $O/F = 3$ at 70% CO_2 level. This value can quench the ignition.

In addition, Table 4.7 shows Mg mass fraction effect on the flame temperature. For the $O/F = 5$, 60% Mg has 1338 K T_{flame}. Increasing Mg percentage to 75% increases motor chamber temperature through 1873 K. Similar rise can been seen for other oxidizer to fuel ratios.

Table 4.7: T_{flame} Variation due to Increased Magnesium Mass Fraction

$CO_2$80%	60% Mg			75% Mg		
$\overline{O/F}$	1	3	5	1	3	5
T_{flame}, K	2244	1373	1338	2530	1967	1873

Chapter 5

HYBRID ROCKET MOTOR DESIGN AND TEST SETUP

Preliminary experiments are performed by using small scale hybrid rocket motor. Small scale tests are defined as PCT (Propellant Characterisation Test). Further experiments are scaled up in order to understand the combustion limit of the carbon dioxide. Because, scale up experiments provide better performance characteristics. Scale up tests are defined as MMT (Mars Motor Test). The motor is defined as MHRM (Mars Hybrid Rocket Motor). This section also presents CAD drawings of both systems, actual ignition images and details of the test setup.

5.1 Propellant Characterisation Test Motor Design

Figure 5.1 shows the PCT rocket motor. The motor is made from stainless steel material. It uses potassium nitrate based pyro to initiate the combustion. The injector of the motor designed as a fitting. Oxidizer flow rates are between 20 and 50 grams per seconds. The fuel grain length is 70 mm. Inner port diameter is 13 mm. Outer diameter of the grain is 31 mm. The graphite nozzle has 3 to 6 mm throat diameter in order to regulate the motor chamber pressure. The total motor length is 122.5 mm with 44.5 mm diameter.

Figure 5.2 shows the complete test system of the PCT. Material of the oxidizer tank is aluminum 6061 with safety factor of 5. It can store 200 grams of oxidizer for 3 seconds motor ignition. Oxidizer tank has a vent port at the top of the tank for the filling process. A manual ball valve is used as isolation valve. Solenoid valve is used as the main valve. Solenoid valve is supplied from [43] and [44]. There are pressure measurement devices supplied from [45]. Pressure transducers show the oxidizer tank and motor chamber pressures during the burn time. There are thermocouples for temperature measurements [46]. Data measurement is performed by using National

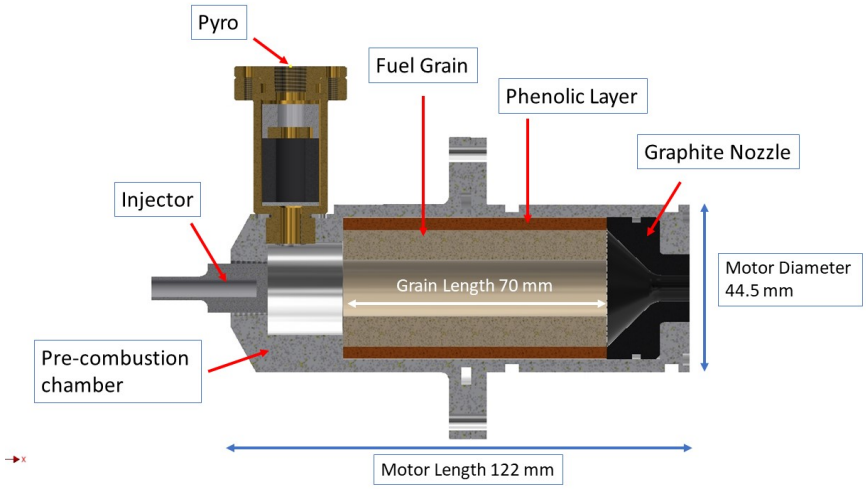

Figure 5.1: PCT Motor Lay-out

Instruments DAQ (Data Acquisition) system [47]. 1/4 inch plumbing is used. All fittings and plumbing is supplied from [48].

Scale up motor and test setup also uses similar plumbing and feed system. Therefore, details of the test setup including sensitivity values of sensors and measurements are explained in the following section.

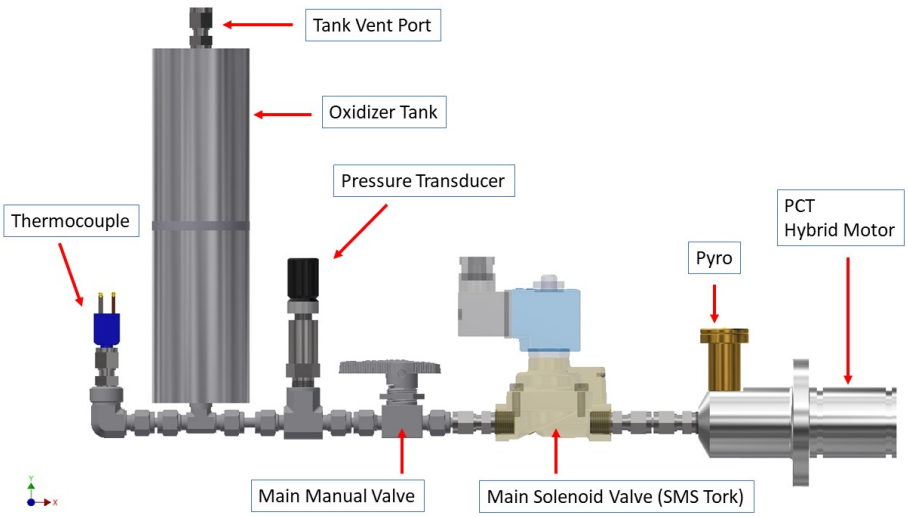

Figure 5.2: PCT Test Setup

Figure 5.3 shows the actual ignition process of PCT experiment. Burn time is

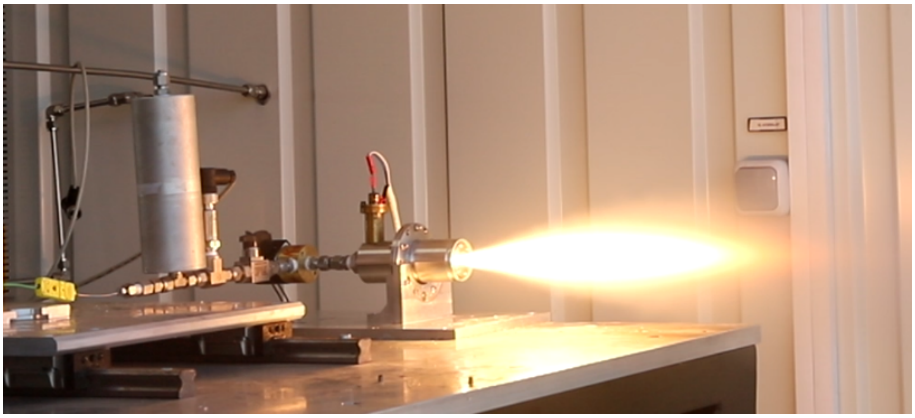

Figure 5.3: Actual Ignition of PCT Experiment

3 seconds with 50 grams per second flow rate. This figure shows a paraffin/nitrous experiment.

5.2 Scale Up Motor (Mars Hybrid Rocket Motor) Design

A classical hybrid rocket motor is designed for the scale up tests. Figure 5.4 illustrates the motor layout. The hybrid rocket motor consists of stainless-steel pre-combustion chamber with 3 grams solid fuel-based pyro section. The pyro is powered with 24V battery. Pyro releases 570 kJ/kg to heat up the motor for 5 seconds. Brass injector chokes the flow therefore downstream pressure has no effect on the flow rate. Brass retainer plate tethers the injector. Oxidizer flow rate changes between 40 and 250 grams per second. Graphite insulator in pre-combustion chamber incarcerates the heat of the pyro fuel. There is a pressure transducer to measure the downstream pressure (motor chamber pressure).

Combustion chamber has a 2.5 mm thick phenolic layer for the grain insulation. Single port fuel grain is 180 mm in length. Inner port diameter is 24 mm, and the outer grain diameter is 48 mm. The post combustion section has phenolic based layer to absorb the ignition. Nozzle (post combustion) pressure is also measured by a pressure transducer. Motor nozzle is made from graphite. The throat diameter is varied from 5 to 11 mm to regulate the combustion pressure.

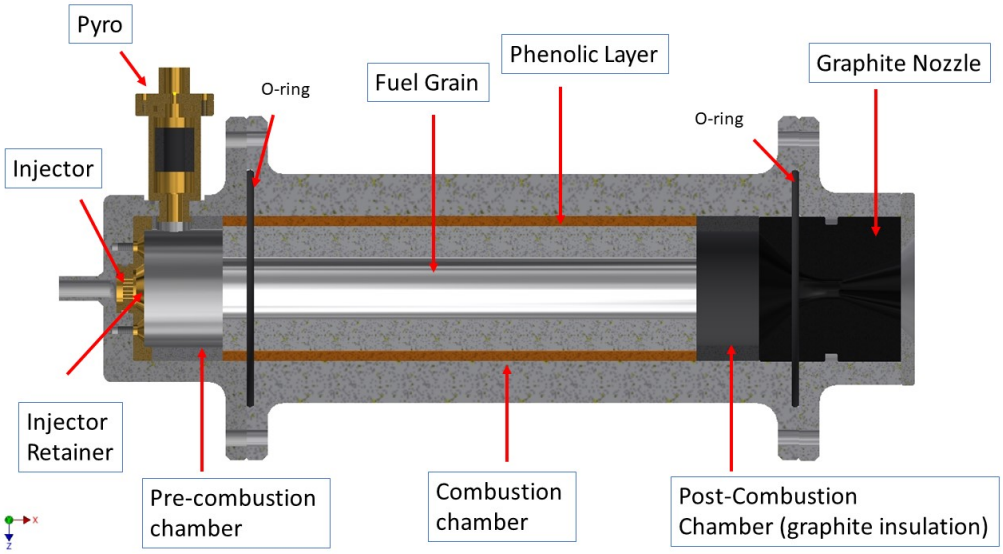

Figure 5.4: Mars Hybrid Rocket Motor Lay-out

5.3 Hybrid Rocket Motor Ignition Process

The ignition of MHRM starts with 2.5 seconds of nitrous combustion (nitrous boost stage). Boost stage exposes enough heat into the motor to take CO_2 combustion easy. Thus, carbon dioxide based combustion (main ignition stage) takes place with an energy boost. Figure 5.5 shows the actual experiment and the test bench.

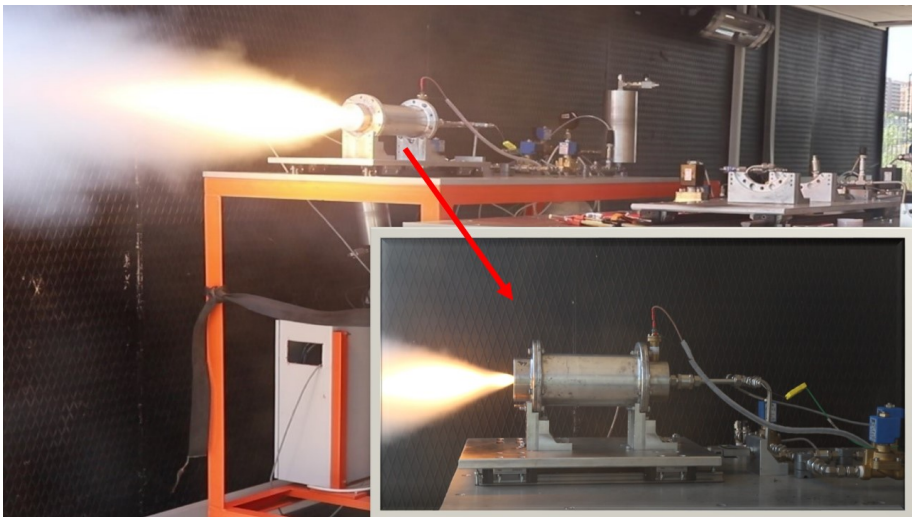

Figure 5.5: MMT Actual Experiment

5.4 The Complete Test Setup

Figure 5.6 shows the complete test setup including nitrous boost line, main ignition feed line and purge lines. The nitrous boost stage uses Aluminum 6061 based oxidizer tank with maximum operating pressure of 280 bars. Nitrous oxide is stored at around 50 bars. Nitrous boost feed line consist of Mv (manual) and Av (automatic) valves for the operation. Purge line uses the same tank as the Nitrous boost line. Purge tank stores 30 bars nitrogen to cool down the motor after the ignition. Main oxidizer tank is a 10-liter aluminum tank, includes CO_2 /N_2O mixture in "blow-down" mode. Main tank has relief valve with 90 bars cracking pressure. Tank also has vent valve, thermocouple and pressure transducer. In addition, mechanical pressure gauge shows the oxidizer pressure as a backup of the NI data acquisition system [47].

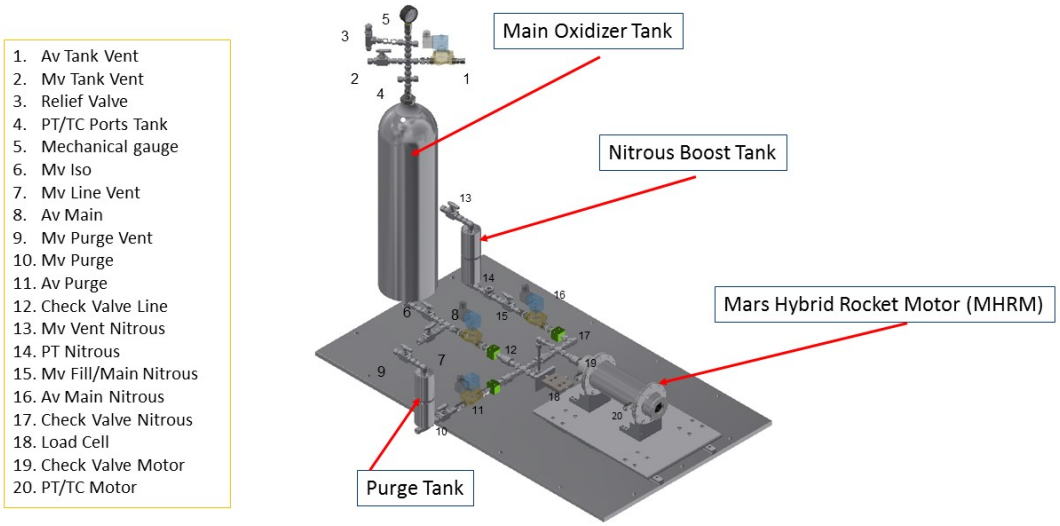

Figure 5.6: MMT the Complete Test Setup

Check valves are used in all feed lines as well as just before the motor entrance. Check valve prevents hydrocarbon fuel leakage through the nitrous feed line. If the nitrous vapor phase interacts with the hydrocarbon, it suddenly decomposes into ni-

trogen and oxygen (releases +19.5 kcal/mole energy). Karabeyoglu [9] experienced decomposition hazard of nitrous due to deflagration wave as sudden pressure increase from 52 bars to 900 bars in 3 seconds. A K-type thermocouple is used to measure the temperatures. Pressure transducer has measuring sensitivity ± 0.5% of the full measurement scale of 70 bars with repeatability that is better than ± 0.05%. Pressure and temperature are recorded using a National Instruments Data Acquisition System and Lab View signal express software. The sampling rate of the DAQ system was set to 5120 Hz. Detailed sensitivity features in error analysis are explained in Appendix B section. All fittings, ball valves, relief valve, and check valves are supplied from Hamlet [48]. Solenoid valves are from SMS Tork [43]. Pressure transducers are from ifm electronics [45]. Thermocouples are from Omega [46].

The test setup uses 3/8 inch sized plumbing, fitting and piping. Pressure transducers has 1/4 inch NPT connection. Thermocuples has 1/8 inch NPT connection.

5.5 Process and Instrumentation Diagram (P&ID)

Figure 5.7 is the process and instrumentation diagram of the test setup. Diagram includes valves on the tanks and locations of the measurement devices. Blue line is the main feed line, yellow line is the nitrous boost line and the red line is the purge section.

The motor uses a load cell in order to record the thrust of the ignition. However, load cell had calibration issues in several experiments.

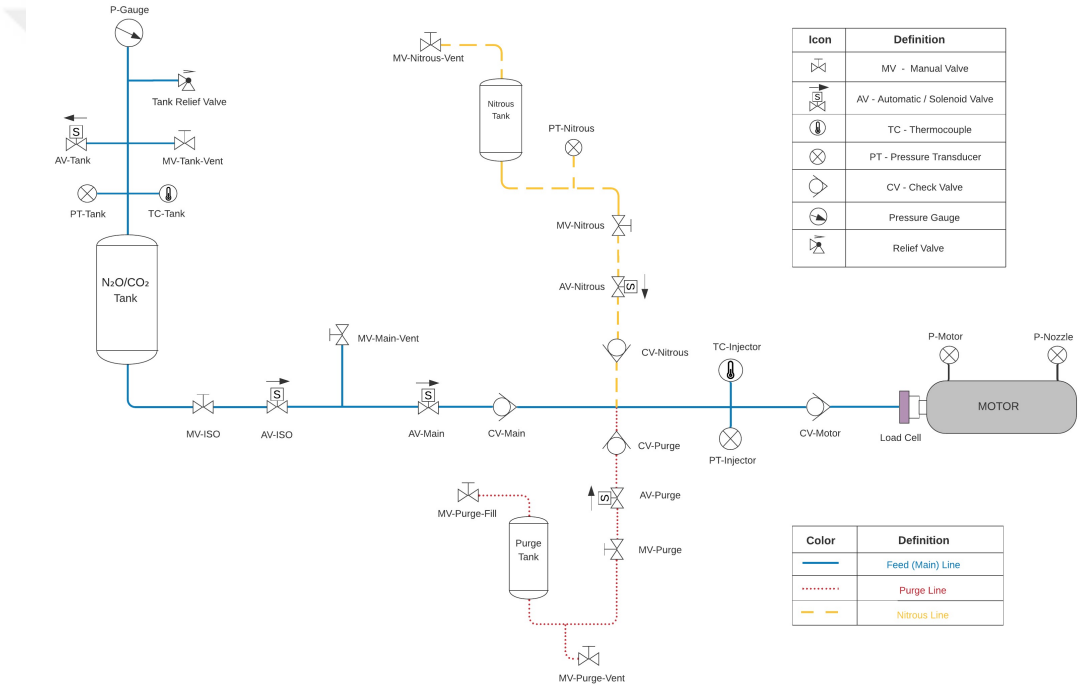

Figure 5.7: Scale Up (MMT) Test Setup P&ID Diagram

Chapter 6

HYBRID ROCKET MOTOR PERFORMANCE EVALUATION

This chapter explains the calculation methods of hybrid motor performance parameters such as oxidizer flow rate ($\dot{m}_{ox}$), regression rate ($\dot{r}$), averaged mass flux ($\dot{G}_{ox}$), specific impulse (I_{sp}), thrust (T) and combustion efficiency (η_{comb}). Mass flow rate is calculated by using mass difference method. Oxidizer mixture operates in blow-down mode with self-pressurizing feature. Regression rate of experiments are quite scattered due to heavy metal loading and CO_2 affect. In hybrid rockets, regression rate highly depend on average oxidizer mass flux. However, carbon dioxide slows down the chemical kinetics during the ignition and regression may be a pressure dependent parameter. Specific impulse and thrust value are also calculated. However, these two parameters are not presented in detail since there is calibration issues in the load cell. Only thrust-time traces of selected experiments are presented to show overall performance of the hybrid motor. Combustion efficiency is another significant parameter for the motor. Combustion efficiencies of magnesium based experiments are really high due to increased motor chamber pressure.

6.1 "Blow-down" Oxidizer Flow Rate Calculation

The oxidizer flow rate is obtained from the before and after weight measurements of the oxidizer masses as Eq. 6.1. The oxidizer mass is reported in grams with a measurement error of 0.003 due to the accuracy of the scale used in tests. Mass flow rate found in Eq. 6.1, is the value that is between main valve opening time and thrust termination. Thrust termination time means valve closing plus an additional time coming from pressure-time traces of specific experiments. Because, there is

an additional oxidizer mass evacuated in feed line between motor entrance and the main valve. When the main valve closes, compressed fluid is evacuated during the thrust termination.

$$\overline{\dot{m}}_{ox} = \frac{M_{oxi} - M_{oxfac}}{t_{burn}} \tag{6.1}$$

Also, there is an additional oxidizer mass between tank and the manual main valve. This mass is vented after the experiment. Therefore, final oxidizer mass includes feed line errors. Eq. 6.12 shows the final oxidizer mass calculation including vented mass.

$$M_{oxfac} = M_{oxf} + M_{vent} \tag{6.2}$$

Oxidizer flow is choked at the injector just before the motor entrance. Therefore, downstream pressure has no effect on the flow rate ($\overline{P}_{ch} = 0$). Figure 3.9 in Chapter 3 illustrates this physical effect.

Blow down oxidizer mixture is influenced by two-phase flow physics. Therefore, it is hard to predict the injector discharge coefficient. Typical injector design with quasi-incompressible or incompressible liquids use Eq. 6.4 for discharge coefficient.

The discharge coefficient (c_d) is a function of the average oxidizer mass ($\overline{\dot{m}}_{ox}$), cross sectional area of the individual injector hole (A_{inj}), number of injector holes (N_{inj}), average fluid density at the injector ($\overline{\rho}_{liquid}$) and the injector upstream pressure ($\overline{P}_{inj}$).

$$\overline{\Delta P} = (\overline{P}_{inj} - \overline{P}_{ch}) \tag{6.3}$$

$$c_d = \overline{\dot{m}}_{ox} / \left(N_{inj} A_{inj} \sqrt{2 \overline{\rho}_{liquid} \overline{\Delta P}} \right) \tag{6.4}$$

In this thesis incompressible assumption is used for the c_d characterisation. Discharge coefficients are obtained to be between 0.2 and 0.35 at the experiments using Eq. 6.4. When the characteristic discharge is found, the next step is to find actual mass flow rate during the burn time. Therefore, Eq. 6.4 is used again by using c_d and new $\overline{\Delta P}$ that is obtained from pressure-time traces of specific experiment.

6.2 Regression Rate Analysis

Hybrid rocket performance analysis requires the identification of space time averaged regression rate ($\overline{\dot{r}}$) and average mass flux ($\overline{\dot{G}_{ox}}$). The regression rate is determined by the ratio of the port radius difference over the burn time in Eq. 6.5. The initial fuel grain diameter is measured by a calibrated caliper. Burn time is found from the pressure time traces. The regression rate is in *mm/s.*

$$\overline{\dot{r}} = \frac{r_f - r_i}{t_{burn}} \tag{6.5}$$

The final port radius is calculated from a "mass reduction-based approach" by using Eq. 6.6. In this equation, fuel grain density (ρ_f) is already known from the casting process. L is the grain length. d_i is the initial fuel grain port diameter. Δm is the difference between initial and final grain masses.

Measurement of the final fuel grain mass is as follows; (i) final grain (phenolic plus unburned fuel) mass is measured by a scale. (ii) the volume of unburned fuel can be found from density and mass. (iii) unburned fuel volume is matched to the cylinder volume to find the final port radius.

$$d_f = \sqrt{\frac{4\Delta m}{\pi \rho_f L} + d_i^2} \tag{6.6}$$

The averaged oxidizer mass flux is another significant parameter in data analysis of the classical hybrid motor combustion. Mass flux during combustion is directly depending on the port diameter of the fuel grain as well as the oxidizer mass flow rate as in Eq. 6.8. The grain port area in this equation is determined using Eq. 6.7. Therefore, the unit of the averaged mass flux is kg/m^2-*s.*

$$\overline{A}_{port} = \frac{\pi}{4}\left[\frac{d_i + d_f}{2}\right]^2 \tag{6.7}$$

$$\overline{\dot{G}}_{ox} = \frac{\overline{\dot{m}}_{ox}}{\overline{A}_{port}} \tag{6.8}$$

6.3 Combustion Efficiency

Combustion efficiency is a significant parameter that affects the performance of hybrid motor ignition. In hybrid motors, combustion efficiency depends on the motor chamber pressure. Generally, higher chamber pressure forms higher combustion efficiency for the same flow rate. Combustion efficiency is the ratio of experimental characteristic velocity (c^*_{exp}) and theoretical characteristic velocity (c^*_{theo}) as stated in Eq. 6.9. Theoretical value is determined by using NASA CEA.

$$\eta_{comb} = c^*_{exp}/c^*_{theo} \tag{6.9}$$

c^*_{exp} refers to the experimental characteristic velocity, is found in Eq. 6.11. The average motor chamber pressure ($\overline{P}_{ch}$) comes from the measured data by NI-DAQ. The nozzle throat area (A_{th}) and the total average flow rate ($\overline{\dot{m}}_{ox} + \overline{\dot{m}}_f$) are other parameters for the characteristic velocity calculation.

In this thesis, magnesium powdered combustion has quite high combustion efficiencies over 0.95 due to really high motor pressure obtained from Mg/CO_2 combustion. Al/CO_2 based experiments mostly have smaller combustion efficiency between 0.50 and 0.75.

$$A_{th} = \pi {d_{th}}^2/4 \tag{6.10}$$

$$c^*_{exp} = \frac{\overline{P}_{ch} A_{th}}{(\overline{\dot{m}}_{ox} + \overline{\dot{m}}_f)} \tag{6.11}$$

6.4 Fuel Flow Rate and Oxidizer to Fuel Ratio

$\dot{m}_f$ is the "fuel mass" flow rate that is calculated using Eq. 6.12. It is calculated by difference between initial and unburnt grain masses ($M_{f_i} - M_{f_f}$) over average test time (t_{av}). The average test time comes from the data reduction process by using thrust termination and burn times in Eq. 6.13.

$$\overline{\dot{m}}_f = \frac{M_{f_i} - M_{f_f}}{t_{av}} \tag{6.12}$$

$$t_{av} = \frac{t_f - t_{burn}}{2} \tag{6.13}$$

In Eq. 6.13, t_f refers thrust termination time. Thrust termination time is the one between main valve closing time and the time when motor chamber pressure becomes below 10 bars. It is measured from pressure-time traces.

The average oxidizer to fuel ratio ($\overline{O/F}$) is significant to understand the effect of the oxidizer compound to the combustion. It is defined by the $\overline{\dot{m}}_{ox}/\overline{\dot{m}}_f$. Experiments performed $\overline{O/F}$ between 2 and 7.

6.5 The Specific Impulse and Thrust

The specific impulse and thrust are another key parameter of the rockets, are shown in Eq. 6.14 and Eq. 6.15.

$$I_{sp} = c^*_{exp} C_F \eta_{nozzle} \eta_{comb} / g_o \tag{6.14}$$

$$T = I_{sp} g_o (\overline{\dot{m}}_{ox} + \overline{\dot{m}}_f) \tag{6.15}$$

The thrust coefficient (C_F) depends on the propellant type and comes from the CEA. The nozzle efficiency (η_{nozzle}) is assumed as 0.98. The combustion efficiency is derived from Eq. 6.11. Finally, the g_o is the gravitational constant of the Earth 9.81 m/s^2. Specific impulse is in seconds. In thrust equation, the total mass flow rate (oxidizer plus fuel mass flow rate) is derived from Eq. 6.1 and Eq. 6.12. The thrust is presented in Newtons. The overall thrust range of small scale experiments (PCT) are between 20 and 60 Newtons. Scale up (MMT) experiments has an overall value of 200 Newtons. MMT motor thrust capability up to 300 Newtons.

Chapter 7

THE HYBRID ROCKET MOTOR TEST RESULTS

This chapter presents results of both PCT and MMT experiments. Over a hundred ignitions are performed for each scales. PCT experiments provide preliminary insight for $Metal/CO_2$ combustion in hybrid rockets. Selected data is presented with performance parameters such as mass flux, regression rate and combustion efficiency. MMT experiments provide more detailed analysis related to the CO_2 combustion in hybrid rockets. For MMT, aluminum and magnesium based experiments are presented in different sub sections. First subsection shows combustion boundary of Al/CO_2 cases. Second subsection focuses on magnesium related tests. Magnesium has better ignition capability with carbon dioxide than aluminum. Pressure time traces with respect to various carbon dioxide levels are presented. Ignition boundary based experiments is presented due to oxidizer mass flux versus carbon dioxide mass fraction. In addition, ignition boundary is discussed due to T_{flame} versus CO_2 mass fraction.

Regression rate evaluation is explained both for lab scale and scale up tests. However, regression rate of experiments are so scattered. Only selected experiments are compared with respect to similar oxidizer mass flux values. In hybrid rockets, regression rate changes due to the mass flux. Motor pressure has no effect on the regression rate. However in this thesis, there are two major factor that affects the regression rate; heavy metal loading and carbon dioxide addition.

Combustion efficiency evaluation due to metal oxide (slag) formation is discussed. Slag formation blocks the nozzle thus motor pressure increases, oxidizer flow rate decreases. Increased motor pressure causes increase in combustion efficiency. In addition, thrust value of selected experiments are presented.

Various of measurement devices are used for experiments such as caliper, scale,

pressure transducers and thermocouples. Key parameters such as regression rate, combustion efficiency and mass flux are depend on sensitivity of these devices. Therefore, an error analysis is made for the data precision.

7.1 Fuel and Test Codes

Experiments are performed with various fuel combinations. Fuel formulations have specific codes for data analysis. Table 7.1 explains the test and fuel codes for both PCT and MMT. The fuel code starts with the metallic powder name and mass fraction in the grain. The following number is the ratio of the structural additive in the paraffin binder. Then the fuel number is written. Casting method is the final identification. HS refers to the high shear mixer. Therefore, the fuel code is in AL40_15_001_HS format. The test names are as follows; PCT (Propellant Characterization Test) and MMT (Mars Motor Test).

Table 7.1: Test Name and Fuel Code

Test #	Additive	Additive %	Structural Additive %	Fuel # and Casting Method
MMT001	Al, Mg	40	15	001_HS

7.2 Small Scale (PCT) Hybrid Motor Results

This section presents the pressure time traces of ignitions due to CO_2 mass fraction. Blue line shows the oxidizer tank pressure, red line is the motor pressure in Figure 7.1. However, red line shows the nitrous boost pressure in the following figures. In these figures, orange line is the motor pressure. Increasing carbon dioxide results in the instability for the combustion. Then, the combustion quenches at a certain level. In addition, selected data of PCT experiments are presented in Table 7.2. In this table, Mg40 is tested at PCT008 – PCT068. Regression rate of experiments are

quite scattered. Figure 7.5 shows the regression rate profiles. Relative error analysis for PCT experiments are also given.

7.2.1 PCT Pressure - Time Traces

The Figure 7.1 shows the stable ignition profile for 22% carbon dioxide 78 % nitrous experiments. There is a little ignition delay due to reduced tank pressure at the beginning. First reduction in tank pressure is caused from blow down characteristics of the saturated liquid mixture. Ignition is highly stable for 3 seconds burn. Then, the main valve is closed and thrust termination occurs 300 miliseconds.

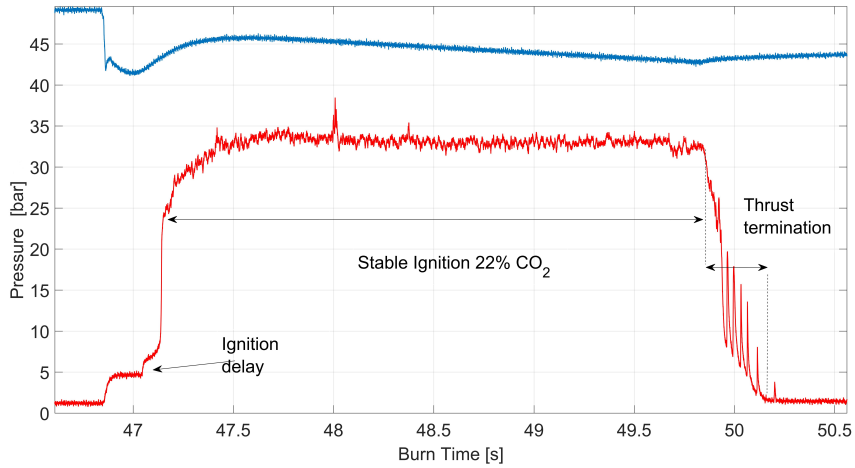

Figure 7.1: Al40 - CO_2 22% Test – Stable Ignition

In Figure 7.2, ignition becomes unstable. Ignition starts with 1 seconds of pure N_2O burn. This nitrous boost stage provides required heat to initiate the CO_2 based combustion. Main ignition takes 3 seconds. Combustion stability is caused by internal ballistics. Nozzle throat diameter is narrow for 1 mm.

Increasing carbon dioxide mass fraction in the oxidizer mixture causes quenched ignition. Nitrous boost successfully burns. However, CO_2 slows down the gas phase reactions thus ignition quenches at 55% cardon bioxide mass fraction.

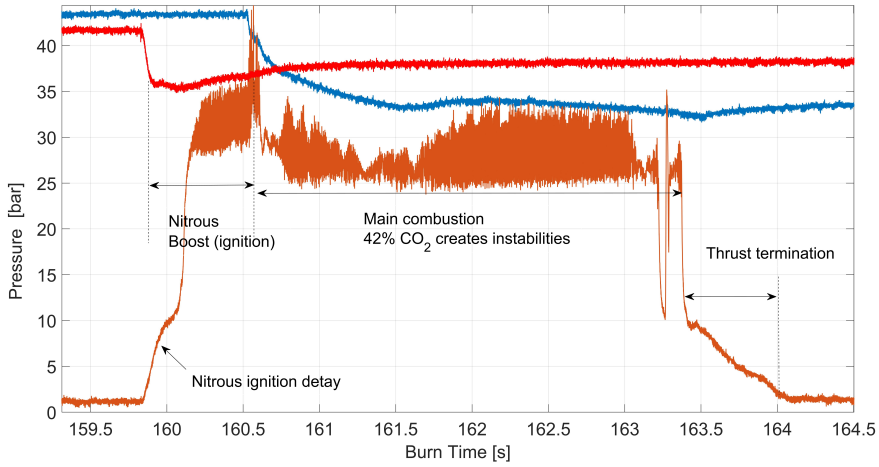

Figure 7.2: Al40 - CO_2 42% Test

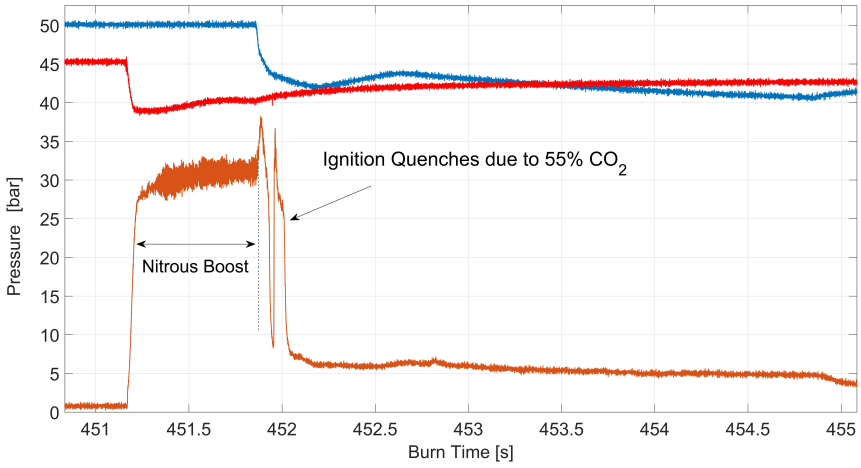

Figure 7.3: Al40 - CO_2 55% Test – Ignition Quenches

7.2.2 PCT Data Analysis

Over a hundred experiments are performed for the PCT. However, only selected data are presented for a consistent data analysis. Table 7.2 shows performance parameters. Overall thrust of PCT motor is found around 50 Newtons. For Al40, 20% CO_2 experiments have average combustion efficiency of 0.75. In addition, Mg40 based experiments with 15% CO_2 shows higher efficiency than aluminum. Therefore, scale up tests are needed for more sensitive analysis.

Table 7.2: PCT Data Analysis: Performance Parameters

Test Code	CO_2 %	$\overline{OF}$	$\overline{G}_{ox}$ (kg/m^2s)	$\overline{\dot{r}}$ (mm/s)	η_{comb}
PCT019	0	7.83	232.67	1.94	0.72
PCT026	0	6.86	186.14	1.95	0.84
PCT028	0	8.18	186.50	1.54	0.85
PCT015	0	5.41	148.45	1.45	0.91
PCT021	0	5.72	138.67	1.75	0.88
PCT027	0	6.65	222.65	1.87	0.86
PCT029	0	5.62	170.085	1.58	0.84
PCT034	12.92	2.52	96.200	2.03	0.75
PCT036	21.84	1.95	69.09	1.87	0.73
PCT050	14.07	3.18	76.47	1.46	0.73
PCT051	13.12	2.23	81.06	2.07	0.75
PCT052	17.70	2.98	107.64	1.95	0.69
PCT056	15.71	2.82	120.78	2.12	0.80
PCT061	21.77	2.88	109.27	2.05	0.75
PCT063	15.12	2.52	80.38	1.70	0.74
PCT090	16.99	3.32	136.15	2.31	0.62
PCT059	32.34	6.27	154.09	1.51	0.83
PCT072	42.70	5.29	144.08	1.37	0.38
PCT008	0	6.66	157.86	1.30	0.89
PCT030	0	6.14	177.65	1.63	0.88
PCT041	0	2.89	117.42	2.53	0.86
PCT043	14.05	2.61	85.90	1.94	0.88
PCT046	15.27	3.22	112.85	2.18	0.79
PCT049	13.5	2.94	85.32	1.76	1.06
PCT068	15.19	4.86	133.58	1.55	0.88

It is worth to note that, aluminum addition to the paraffin wax reduces the oxidizer to fuel ratio. CO_2 addition provides further reduction in O/F. Figure 7.4 shows the reduction. Experimental O/F reduction verifies the theoretical analysis performed by the CEA in Chapter 3.

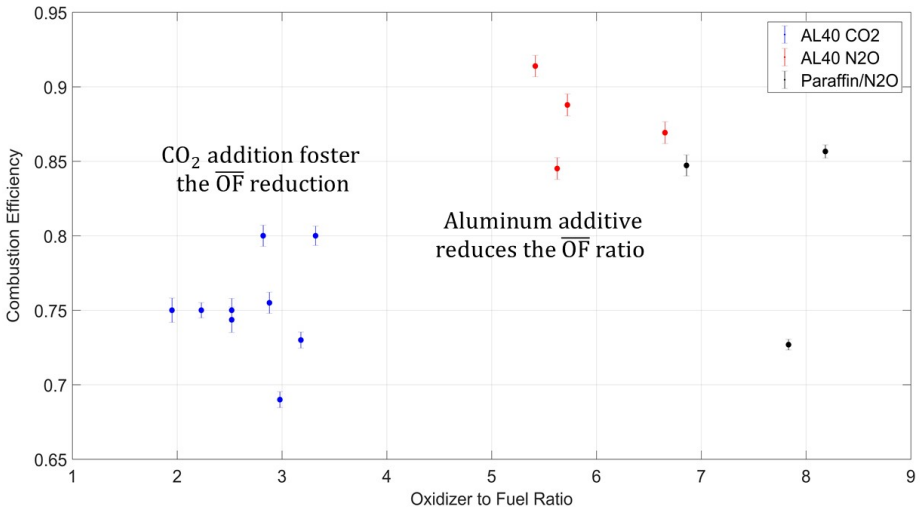

Figure 7.4: η_{comb} versus O/F of PCT Experiments

Regression rate of PCT experiments are quite scattered. However at lower mass fluxes, regression rate of aluminum based experiments are higher than the reference fuel that is SP7. Figure 7.5 shows the comparison of the regression rate. At lower mass fluxes (between 60 and 120 kg/m^2s), increased regression rate is achieved due to heavy metal loading. CO_2 effect on regression rate cannot be determined due to scattered data.

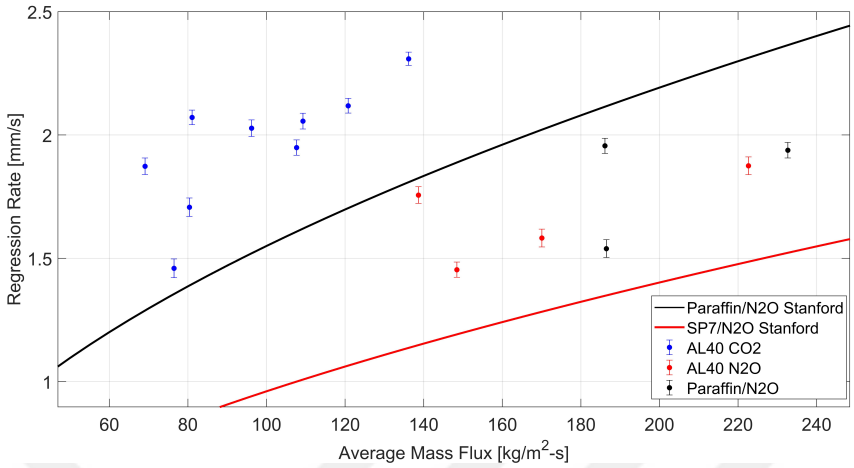

Figure 7.5: Regression Rate Comparison of PCT Experiments with SP1 and SP7

7.2.3 PCT Relative Error Analysis

Relative error analysis provides the sensitivity of data measurements. Sensitivity of scales and caliper is 0.01. Pressure transducer has measuring sensitivity ± 0.5% of the full measurement scale of 70 bars with repeatability that is better than ± 0.05%.

Table 7.3: Relative Errors of PCT Experiments

Name	**Definition**	**Average Error**	**Factor**
Final port diameter at the thrust termination	E_{dvc}	0.0075	Final grain diameter
Final diameter	E_{df}	0.0075	Grain Properties: Mass, density and length
Regression Rate	E_{reg}	0.016 – 0.020	E_{dvc}, E_{df} *and burn time*
Oxidizer mass flux	E_{gox}	0.06	E_{dvc}, E_{df} *and* E_{Mox}
Oxidizer flow rate	E_{Mox}	0.051	Oxidizer mass difference; scale sensitivity

7.3 Scale Up (MMT) Hybrid Motor Results

7.3.1 Paraffin/Aluminum/CO_2/N_2O

CO_2 Ignition Capability

Figure 7.6 shows the ignition boundary of aluminum based experiments. Blue dots are successful and stable ignition profiles of 40% Aluminum up to 130 grams per second (corresponds 160 kg/m^2s mass flux). Green dots are quenched ignitions of 40% Aluminum. PCT provides that ignition boundary is found at 45% CO_2 for Al based experiments [10]. Ignition fails at 53% carbon dioxide for Al40.

Red dots show Al60 based ignitions. These ignitions are performed by using 30% flake and 30% spherical shaped Al. Flake addition increases the successful ignition rate to the 52% carbon dioxide level. Flake shape has larger surface area, thus increases the combustion rate compared to spherical shaped powders. However, there is a quenched ignition for Al60 that is seen as black dot. Therefore, Al60 has maximum ignition limit at around 50% CO_2.

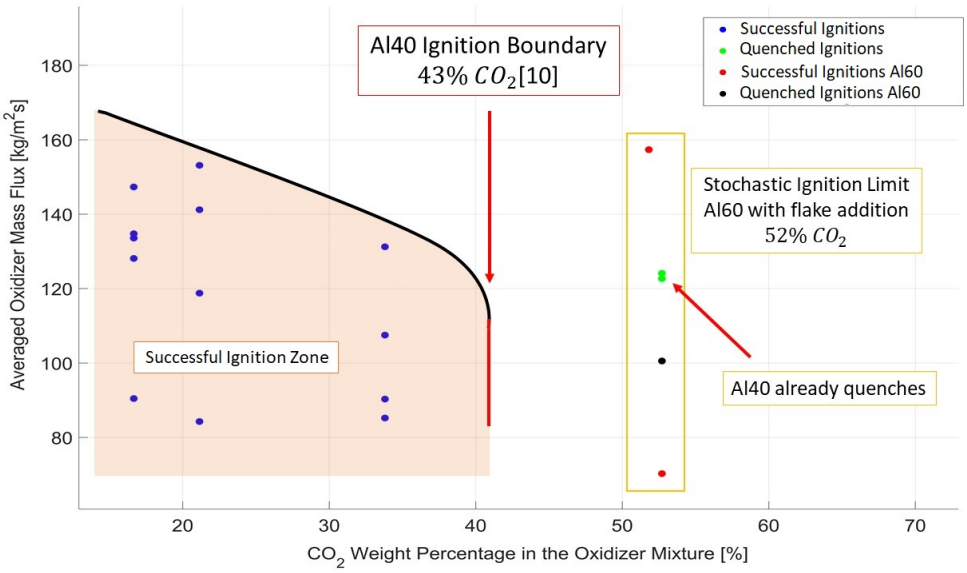

Figure 7.6: Ignition Boundary of Al/CO_2 Experiments due to the Mass Flux

The motor chamber pressure (adiabatic flame temperature) is the key factor to achieve a successful combustion. Combustion quenches below a certain T_{flame} level.

Thus, T_{flame} profile due to the carbon dioxide mass fraction is shown in Figure 7.7. Ignition capability is achieved up to 2200 K. Al40 based ignitions quench below 2200 K. Adiabatic flame temperature increases with high level of metal additive inside the fuel. Figure 7.7 shows that Al mass fraction is increased to 60% (60% Aluminum and 40% Paraffin wax). For Al60, 30% of this content is casted as 3 micron flake shaped Al, and 30% is casted as spherical shaped aluminum. Flake shaped powder has larger surface area that forms better ignition characteristics. Thus, successful combustion limit is increased up to 55% CO_2. Flame temperature is found as 2600 K at this carbon dioxide level. However, this limit is considered as "stochastic limit" since there are also ignition failures.

It is worth to note that theoretical ignition temperature of Al/CO_2 is found as 2000 K from the literature [32]. Therefore, MMT experiments show that the lower ignition limit for Al40 at 43% CO_2 corresponds the theoratical ignition limit of Al/CO_2.

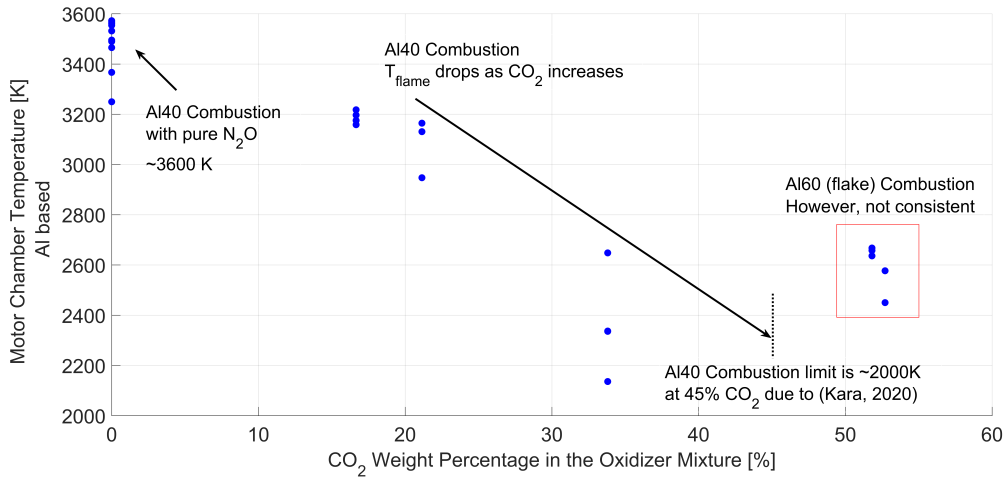

Figure 7.7: Adiabatic Flame Temperature Variation of Al/CO_2 Tests

Ignition capability of Al40 based tests are also presented in Figure 7.8 with respect to the averaged oxidizer mass flux. Figure 7.8 shows that ignition quenches at around 2000 K for Al40 fuels. At this ignition limit, average mass flux corresponds to 70 kg/m^2s.

Furthermore, increasing the averaged mass flux reduces the T_{flame} to 1700 K as seen in red dots in Figure 7.8. For the increased aluminum content (Al60), the adiabatic flame temperature reaches 2500 K. There are two successful Al60 tests at flux values of 70 and 157 kg/m^2s. However there is a quench value at 100 kg/m^2s. Both experiments are performed at 52% carbon dioxide level for Al60.

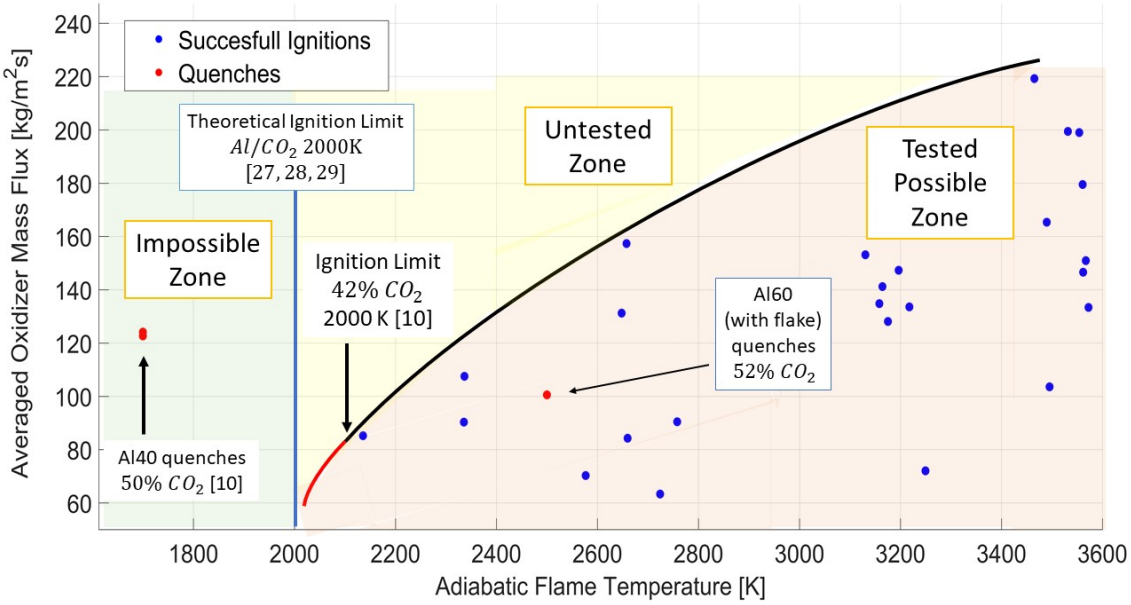

Figure 7.8: Averaged Mass Flux versus Adiabatic Flame Temperature Al/CO_2

Data Results

Details of data results are presented in Appendix A section; Tables A.1 - A.5. In this section, Table A.1 and A.2 show the regression rate versus averaged mass flux for the $Paraffin/Al/N_2O/CO_2$. Tables A.3 and A.5 presents the performance parameters such as oxidizer to fuel ratio, combustion efficiency, motor chamber pressure, oxidizer flow rate, discharge coefficient and motor chamber temperature.

According to Table A.3, combustion efficiency of $Al/Nitrous$ based experiments are 0.80 in average. Adiabatic flame temperature of ignitions are 3500 K. Various O/F ratios are tested between 3 and 8. In the Table A.5, CO_2 based MMT are presented. Combustion efficiencies decrease by CO_2 addition. Overall range of

combustion efficiency is found as 0.65. However, Al60 experiments (MMT032 and MMT037) increases the efficiency due to the slag formation. Slag formation blocks the nozzle and increases the motor chamber pressure. Therefore, efficiency is increased. Furthermore, Table A.5 shows that T_{flame} reduces significantly with the CO_2 addition (to 2500 K). Thrust range of experiments are changing between 80 and 350 Newtons.

7.3.2 $Paraffin/Magnesium/CO_2/N_2O$

The performance of a motor is evaluated using pressure-time variation measured during the combustion by data acquisition system. Therefore, this section shows the 'Pressure-Time' traces of actual motor ignitions. In figures, the red line shows the nitrous oxide tank pressure (nitrous boost ignition zone), the yellow line is the injector upstream pressure, the blue line shows the main tank (CO_2/N_2O oxidizer mixture) pressure. Purple and orange colours are motor chamber and nozzle pressures.

Combustion starts as follows; (i) Mg/N_2O combustion starts with an ignition delay. (ii) the motor pressure increases significantly to above 40 bars. (iii) Main ignition starts with CO_2/N_2O oxidizer mixture. CO_2 has a significant effect on combustion. CO_2 slows down the chemical kinetics (chamber pressure drops) like a fire extinguisher and reduces the motor chamber temperature. Adiabatic flame temperature change with CO_2 addition is also discussed in this section.

Pressure - Time Traces

Successful and stable ignition achieved up to 70% CO_2 in the classical hybrid motor. Figure 7.9 shows the $Mg60$ CO_2 68% experiment. Magnesium has delayed ignition characteristics with nitrous oxide that can be seen during the "nitrous ignition" section. Then, the CO_2/N_2O oxidizer is injected causes sudden drop in motor chamber pressure. Motor flame temperature also drops significantly compared to pure nitrous combustion. Pressure drop then recovers during the rest of the combustion.

Increasing CO_2 level to 75% makes the combustion relatively unstable as pre-

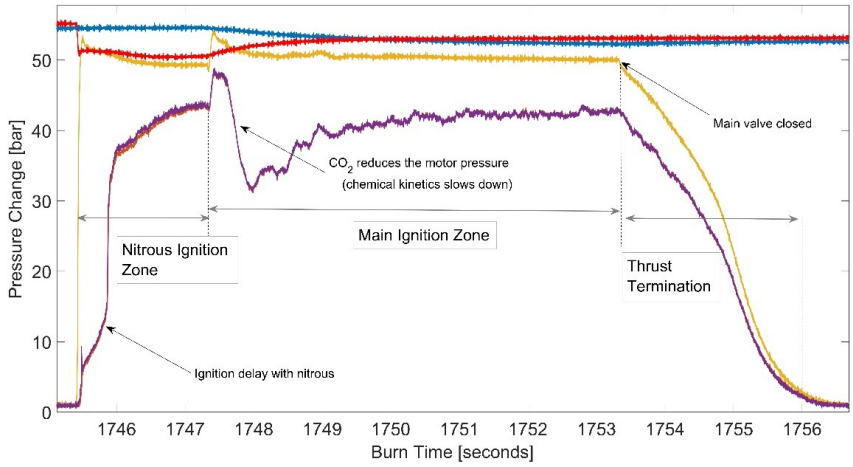

Figure 7.9: Mg60 - CO_2 68% Test – Stable Ignition

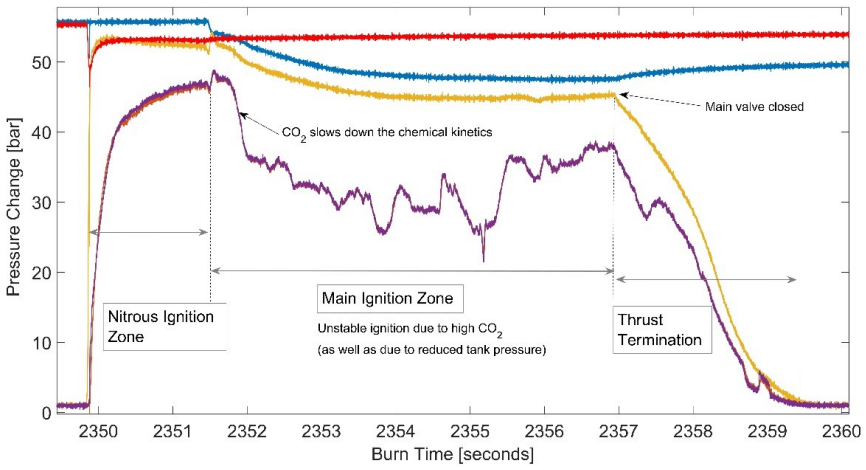

Figure 7.10: Mg60 - CO_2 75% Test – Unstable Ignition

sented in Figure 7.10. Nitrous oxide successfully ignites the motor. Then, 75% CO_2 25% N_2O mixture reduces the motor pressure from 45 to 35 bars. Pressure decrease also affects the motor stability. CO_2 reduces the motor chamber temperature from 3000 to 1500 K in this experiment.

Classical hybrid rocket motor quenches at the 80% CO_2 level. Figure 7.11 shows the pressure time trace of Mg60 $CO_2$80% firing. After the nitrous boost, the motor immediately quenches due to carbon dioxide injection.

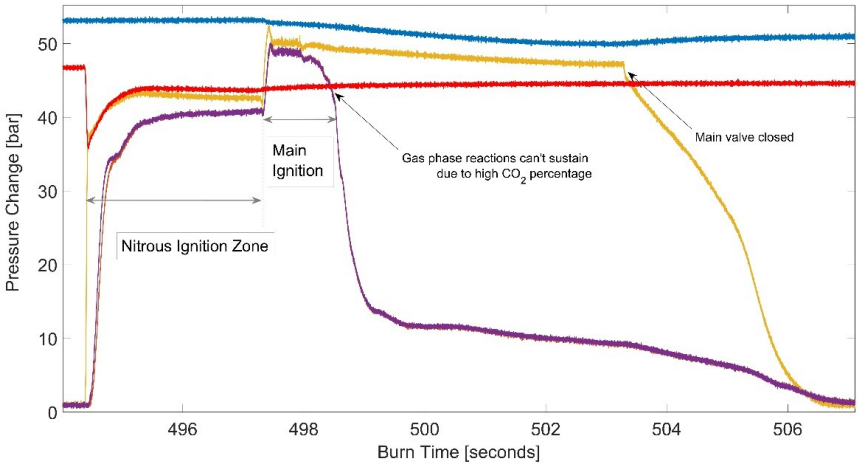

Figure 7.11: Mg60 - CO_2 80% Test – Quenched Ignition

CO_2 Ignition Capability

Pressure-time traces show that carbon dioxide slows down the chemical kinetics. It means that motor chamber temperature decreases. Combustion quenches (fails) below a certain T_{flame}. Thus Figure 7.12 shows T_{flame} variation due to CO_2 addition at hybrid motor experiments. The stable ignition occurs at 75% CO_2 level around 1700 - 1800 K. Ignition quenches below 1600 K.

Ignition boundary is also studied by using oxidizer mass flux. In Figure 7.13, the blue dots show the successful experiments for particular oxidizer flow rates. Green dots are successful but unstable ignitions. Red dots indicate the quenched ignitions. There are two points at 64% CO_2 which are unstable and are considered as outliers. 75% CO_2 is the stochastic limit of the motor ignition. At this point, ignition is unstable or quenches arbitrarily. Ignition fails above 75% CO_2. In Figure 7.13, successful ignition zone is stated as orange field. The boundary is shown as red dashed line around 72.5% CO_2. There is a misfire data due to really high oxidizer mass flux for 70% CO_2.

The ignition limit is also stated as averaged mass flux versus adiabatic flame temperature. Figure 7.14 shows that the combustion quenches at motor chamber pressure (adiabatic flame temperature) below 1600 K. So, the yellow zone is prac-

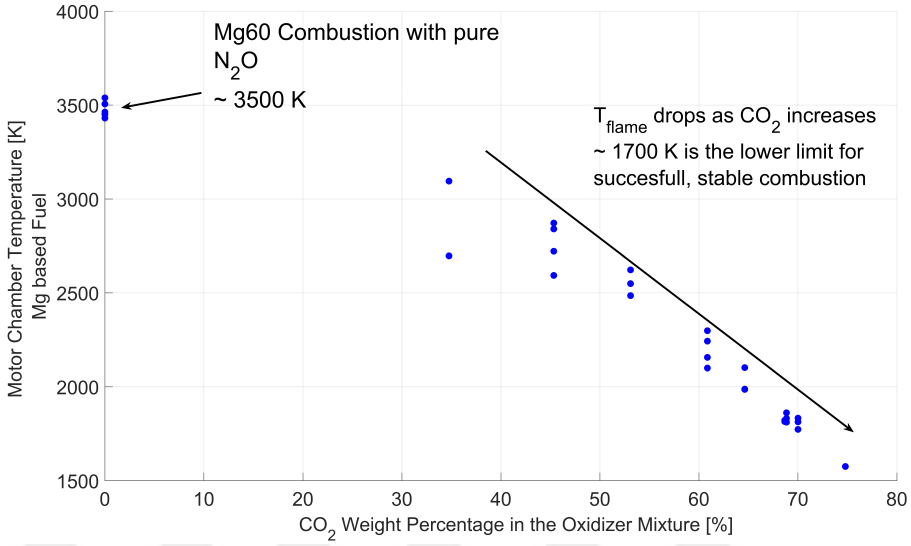

Figure 7.12: Adiabatic Flame Temperature Variation of Mg/CO_2 Tests

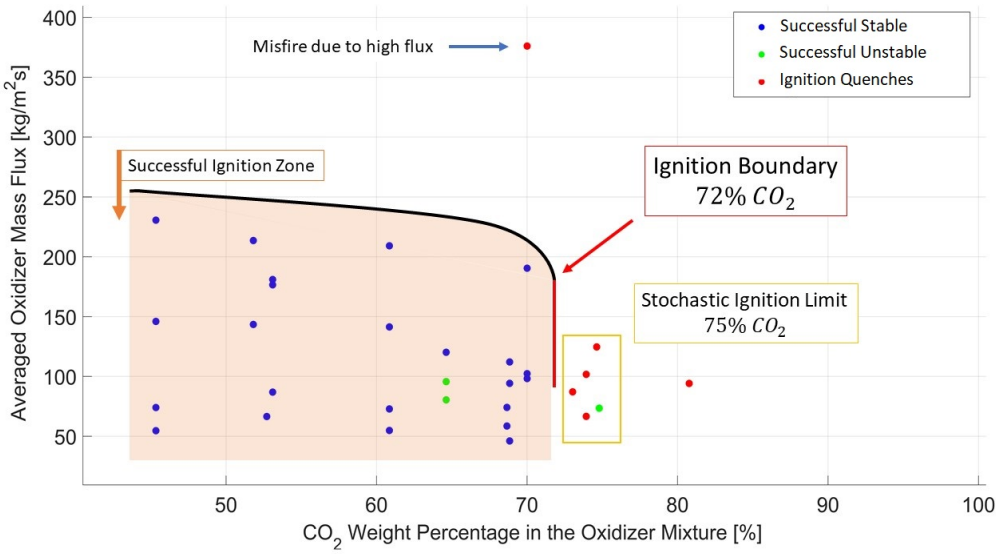

Figure 7.13: Ignition Capability of Mg/CO_2 Experiments due to the Mass Flux

tically impossible region due to ignition boundary. Red dots state the quenched ignitions. In addition, 1000 K is the theoretical combustion value of Mg/CO_2 according to [32, 33, 34]. Therefore, the blue zone is theoretically impossible zone for the combustion. Practically possible zone is shown as orange region. Paraffin/Mg

based hybrid motor that operates in this region successfully ignites CO_2. There is a quenched ignition point at an average mass flux of 375 kg/m^2s for 70% CO_2.

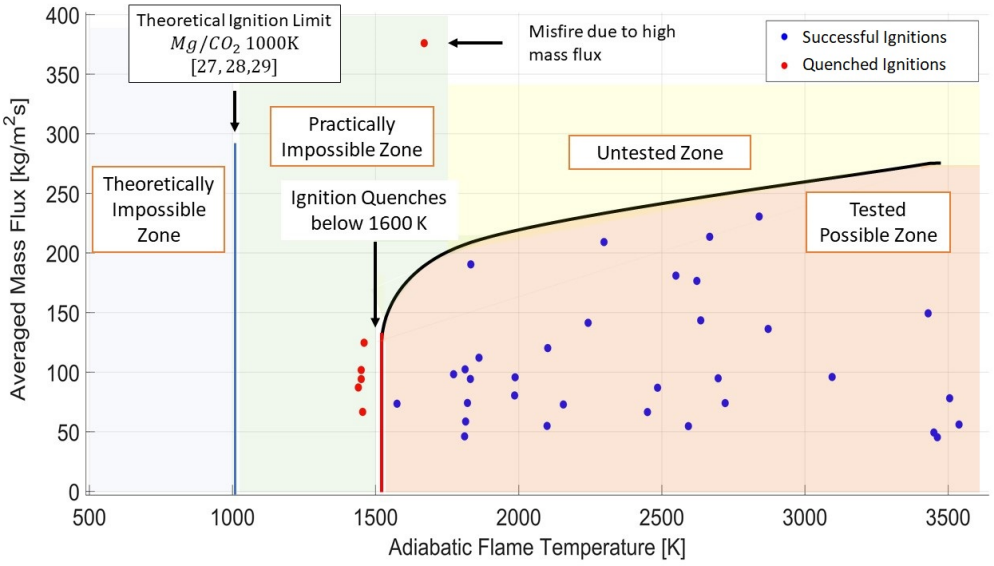

Figure 7.14: Averaged Mass Flux versus Adiabatic Flame Temperature - Mg/CO_2

In addition Figure 7.14 shows that MMT motor can operate oxidizer mass flux range of 45 to 260 kg/m^2s. A larger motor is needed to achieve mass flux ranges above the 260 kg/m^2s.

Combustion Efficiency

Combustion efficiency depends on the motor chamber pressure during the ignition. Magnesium powder shows easy ignition characteristics with carbon dioxide. One-half of products due to this combustion generates magnesium oxide (MgO). High level of oxide formation (slag formation) blocks the nozzle throat (as well as the injector) especially with low flow rates. Blockage in the nozzle cause a significant increase in chamber pressure.

Oxide formation after experiments is shown in Figure 7.15. Magnesium oxide has the melting point of 3125 K that is well above the motor temperature of CO_2 based experiments. Therefore, magnesium oxide is formed as a thin film inside the

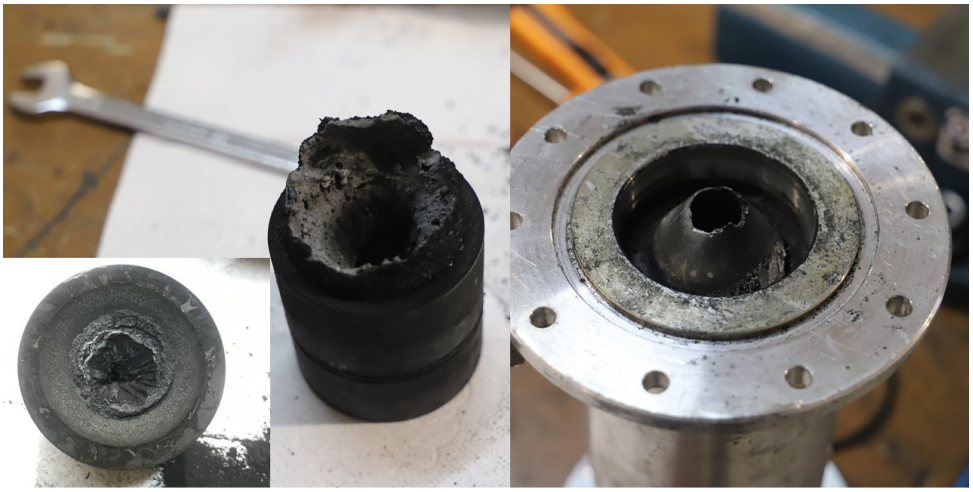

Figure 7.15: Magnesium Oxide Slag Formation After the Ignition

post combustion chamber (and nozzle). Approximately 8% of unburned fuel consist of condensed combustion products as magnesium oxide.

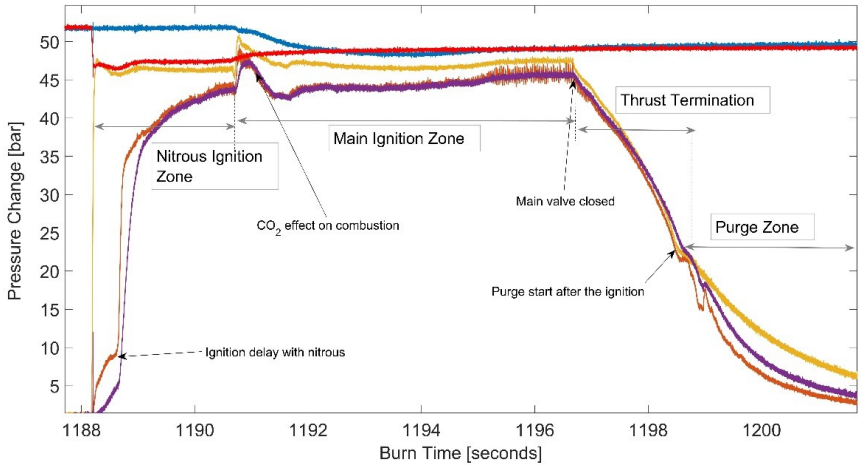

Figure 7.16: Pressure Time Trace of Slag Formation Test

In Figure 7.16, ΔP $\left(\overline{P}_{inj} - \overline{P}_{ch} \right)$ of this experiment seem stable and is 2 bars. Stable pressure differences indicates that oxide formation has uniform-thin film characteristics.

Data Results

Significant parameters of carbon dioxide based firings are presented in Tables A.7 to A.11. Tables A.7 and A.8 show regression rate versus mass flux. Tables A.9 and A.11 show performance parameters. Upstream pressures are around 50 bars. Motor chamber pressures are around 40 bars. Combustion efficiencies of magnesium based experiments are quite high, mostly above 95% at various of O/F ratios. Thrust values of Mg based experiments are changing between 100 and 350 Newtons. Tables A.4 and A.6 illustrate thrust and specific impulse values of experiments.

Thrust measurements are performed by using s-type load cell. Some experiments have calibration issues. However, two tests are selected to show as examples; MMT097 and MMT101. Both experiment has similar flow rate values. In Figure 7.17 MMT97 has 60% CO_2. Figure 7.18 consists of MMT101 experiment with 70% CO_2.

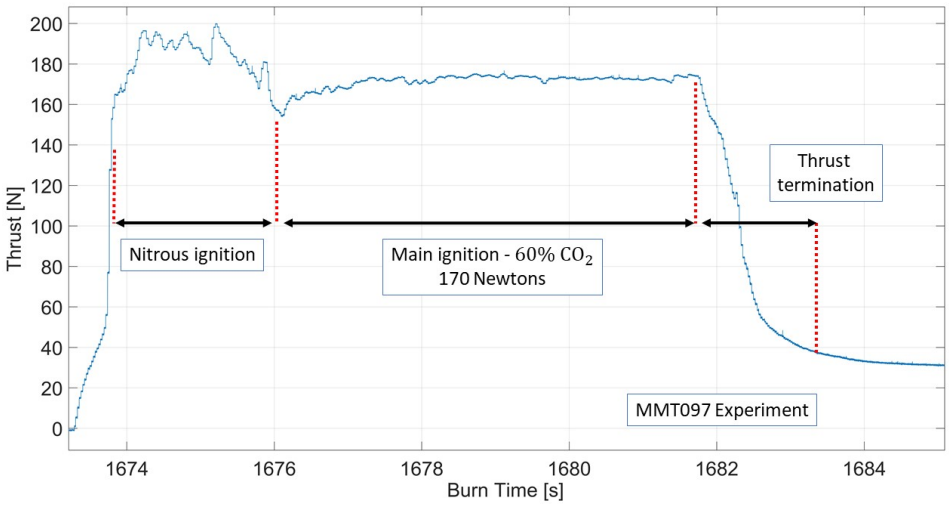

Figure 7.17: Thrust Variation of MMT097 Experiment

In Figures 7.17 and 7.18, y-axis shows the thrust variations. X-axis is the total ignition time. Both parameters are measured by using NI DAQ system. First section shows the nitrous boost region. Second section is the main ignition zone with carbon dioxide. MMT097 and MMT101 have similar total mass flow rate values (oxidizer

plus fuel flow rates). However, MMT097 has higher combustion efficiency. Therefore, MMT097 has an average thrust value of 170 N. MMT101 has 160 N average thrust. Theoretical thrust value of MMT093 is found as 249 N. MMT101 has theoretical thrust of 185 N. There is 40% error in MMT097 and 15% error in MMT101.

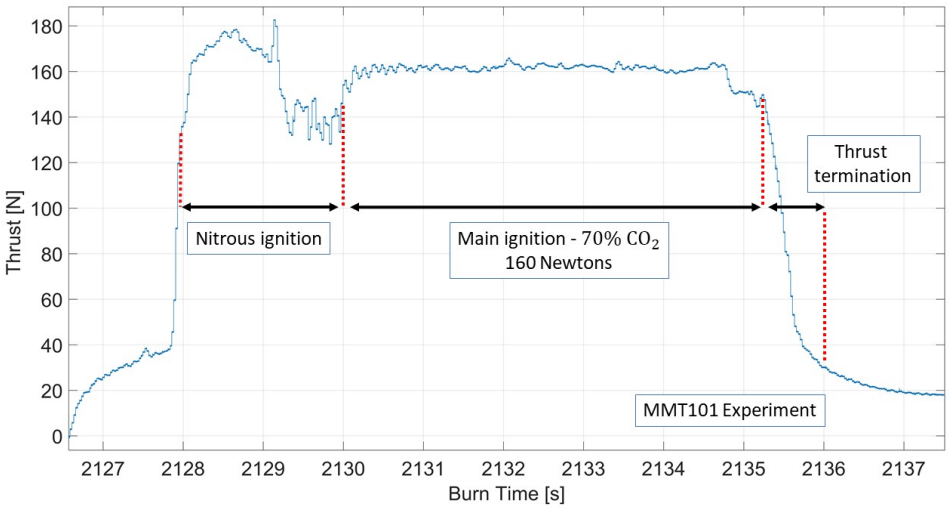

Figure 7.18: Thrust Variation of MMT101 Experiment

In Table A.8, pure nitrous oxide based experiments are presented. Combustion efficiencies are above 100% due to slag formation during the experiments. 60% Mg loaded fuels hardly ignite with N_2O. Thus, the ignition creates high oxide formation. High CCP formation blocks both injector holes and nozzle throat. Injector blockage reduces the oxidizer mass flux. And, nozzle throat blockage results an increase in motor chamber pressure.

However in Table A.9, MMT104 shows a feasible results without blockage issues. Combustion efficiency of the MMT104 is 0.63 which indicates the poor combustion mechanism of heavy loaded Mg with the nitrous oxide.

CO_2 based tests are presented in the Table A.11. These experiments are performed with oxidizer mass flow rates ranging from 47 to 220 grams per seconds. Thus averaged mass flux values are stated between 60 and 210 kg/m^2s. Combustion efficiencies of CO_2 based tests are quite high that is above 0.95. Slag formation

is the most significant reason for high efficiency.

However, experiments with less CCP formation still provides higher efficiency values compared to pure nitrous cases. For example, MMT36 has similar flow rate with MMT104 (pure nitrous experiment). MMT36 consist of 52% CO_2 and higher efficiency than MMT104.

Tables A.9 and A.11 also show oxidizer to fuel ratio and adiabatic flame temperature data sets. Adiabatic flame temperatures of $Mg/Nitrous$ are found as 3500 K. Carbon dioxide addition reduces the T_{flame} significantly to 1700 K.

In addition, various of experiments have instabilities during ignition. These instabilities are considered as feed coupled and low frequency instabilities. Two experiment are shown to evaluate combustion instabilities. MMT089 is a stable experiment shown in Figure 7.19. There is a noise at a specific pressure value of MMT089 experiment. Motor and nozzle pressures show this noise. Motor pressure is the purple line. Nozzle pressure is the orange line. Blue line is the main tank pressure. Yellow is the injector upstream pressure. The red line is the nitrous pressure.

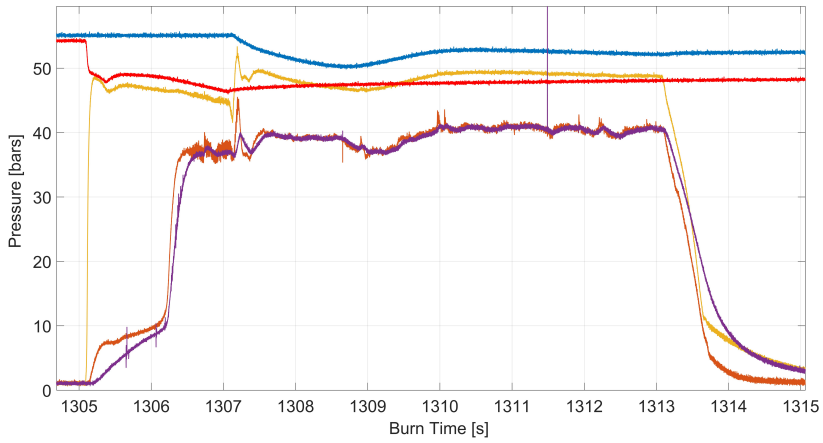

Figure 7.19: Pressure Time Trace of MMT089 Experiment

Pressure time plot of the MMT097 is shown in Figure 7.20. MMT097 is highly stable experiment at main ignition zone. However, nitrous boost region has instabilities.

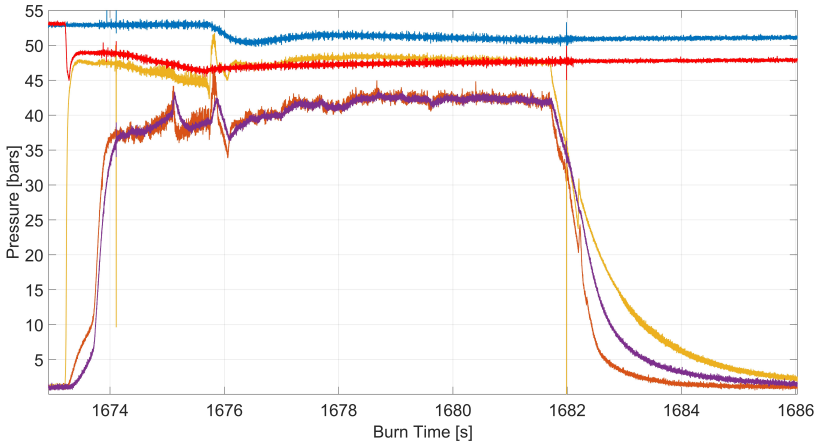

Figure 7.20: Pressure Time Trace of MMT097 Experiment

FFT (Fast Fourier Transformation) results are presented in Figures 7.21 and 7.22. Sampling frequency of experiments are taken as 5200 Hz.

In MMT089, low power instabilities occur at 440 Hz due oscillations of the main tank pressure. This oscillation affects injector upstream pressure and nozzle (post combustion) pressures. However, motor ignition does not show any instability at 440 Hz. Motor shows low frequency instability at 60 Hz. There is a noise at 2000 Hz. Noise amplitude is higher in the motor compared to the feed line.

MMT097 experiment has feed coupled oscillations due to the tank pressure. Tank and feed line show a peak instability at 440 Hz due to the sensor noise. In addition, low frequency oscillations occur in pre-combustion chamber at the beginning of the combustion. Low frequency occurs at around 50 Hz. Nozzle pressure measurement does not show any significant instability. The only peak is occured 440 Hz due to the sensor noise.

Both MMT089 and MMT097 show peak amplitudes at 2500 Hz. This peak is normal due to the sampling frequency of the pressure transducers.

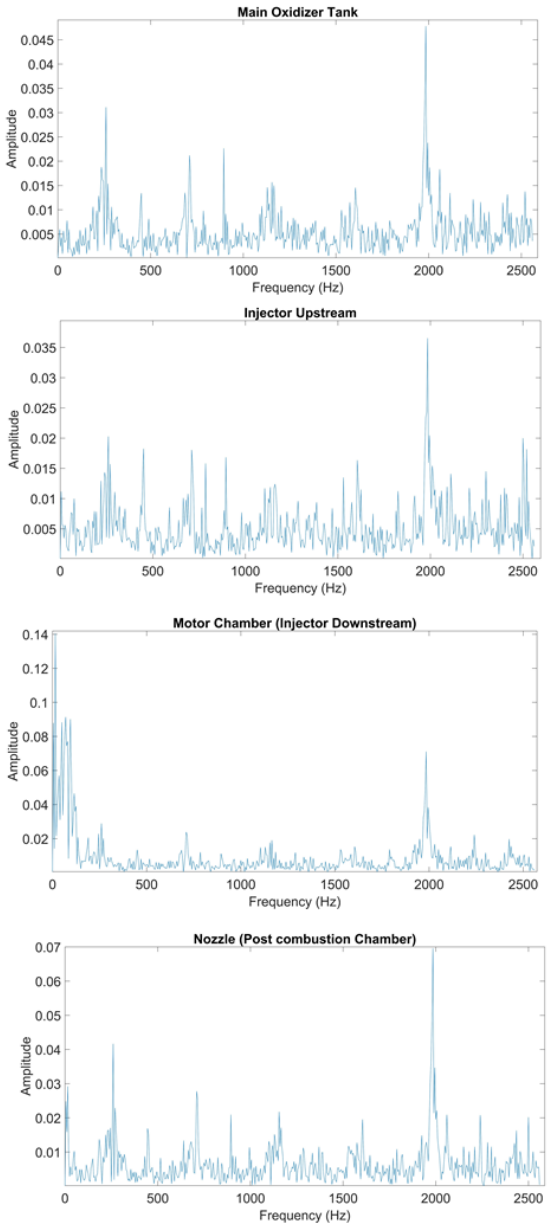

Figure 7.21: FFT Analysis of MMT089 Experiment

7.3.3 MMT Regression Rate Evaluation

In hybrid rockets, regression rate model is assumed according to diffusion limited model as shown in Figure 7.23. Motor chamber pressure has no effect on regression rate at moderate flux values. Therefore, regression rate is defined as in Eq. 7.1. Coefficients a and n are determined curve fitting obtained from various of experiments.

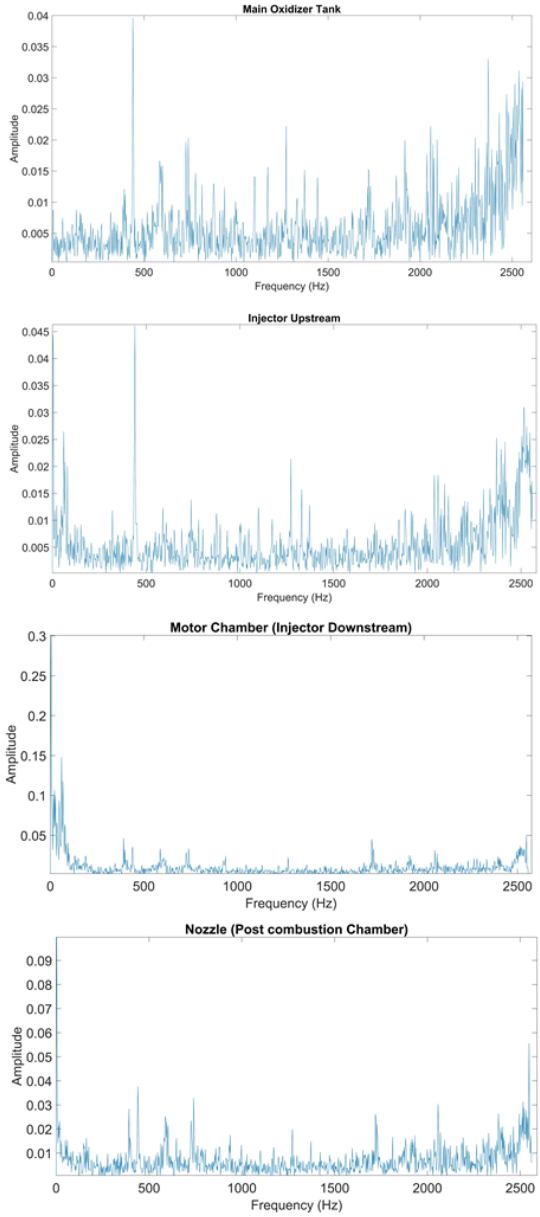

Figure 7.22: FFT Analysis of MMT097 Experiment

In these formulas regression rate is in mm/s and oxidizer mass flux is in kg/m^2s.

$$\overline{\dot{r}} = a\overline{\dot{G}}_{ox}^{n} \tag{7.1}$$

Coefficients a and n due to various of propellant combinations are presented in Table 7.4 [32]. The unit of a is $(m^{2n+1})/(kg^n s^{1-n})$.

However in this thesis, experiments involve heavy metal loading as well as high

Table 7.4: Regression Rate Coefficients for Various Hybrid Propellants

FUEL	**OXIDIZER**	a	n
HTPB	LOX	3.043×10^{-2}	0.0681
HDPE	LOX	2.34×10^{-2}	0.62
Paraffin	LOX	11.70×10^{-2}	0.62
Paraffin	N_2O	15.5×10^{-2}	0.50

carbon dioxide amount. Heat transfer mechanism due to heavy metal loading directly affects the regression rate model. In addition, carbon dioxide slows down chemical kinetics, thus motor pressure become significant in regression rate. This theory is shown in Figure 7.23 [37]. Detailed analysis of regression rate is not the scope of this thesis. Kinetics limited models and radiative heat transfer will be studied in upcoming studies.

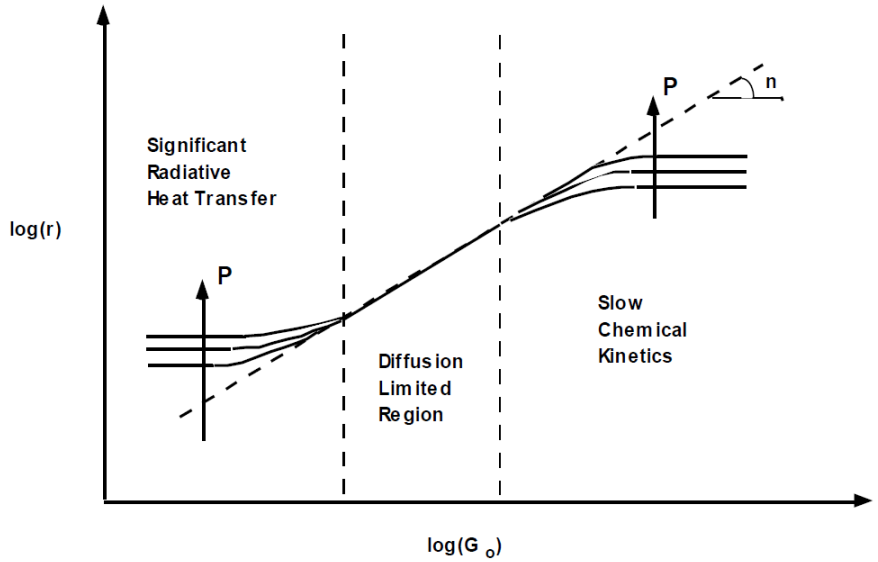

Figure 7.23: Effect of Pressure on the Regression Rate [28]

In this thesis, a brief comparison is made in order to show how carbon dioxide affect the regression rate. Magnesium and aluminum based cases are presented in separate sections.

Magnesium Effect on Regression Rate

Table 7.5 shows averaged mass flux versus regression rate values of particular experiments. Flux ranges of experiments are considered between 55 and 146 kg/m^2s. Data table is also shown as Figure 7.24 for more clear understanding.

According to this figure, carbon dioxide addition has no particular effect on the regression rate at flux values between 55 and 75 kg/m^2s. Regression rate slightly decreases with the CO_2 addition at higher mass fluxes such as 132 and 210 kg/m^2s. In addition, 50% CO_2 can be considered as a critical point at high mass fluxes. Because, a sharp drop is shown in Figure 7.24 at the flux level of 132 kg/m^2s. Flux level of 210 is not shown in the figure since there is only two data points.

Table 7.5: CO_2 Effect on Regression Rate - Mg Cases

Test #	$\boldsymbol{CO_2}$ **(%)**	$\overline{\dot{G}}_{ox}$ $\boldsymbol{(kg/m^2s)}$	$\overline{\dot{r}}$ $\boldsymbol{(mm/s)}$
1	0	56.02	0.58
2	60.85	54.8	0.62
3	0	78.06	0.59
4	45.34	74.00	0.61
5	60.85	72.83	0.52
6	68.66	74.10	0.67
7	74.79	73.46	0.61
8	0	149.31	1.01
9	51.81	143.40	0.94
10	60.85	141.34	0.63
11	51.81	213.52	1.05
12	60.85	209.11	0.79

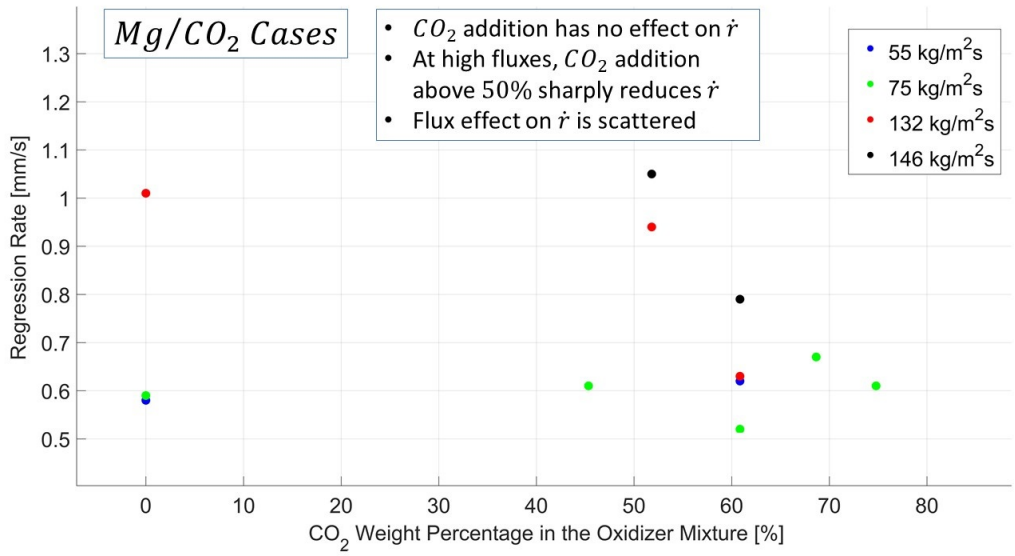

Figure 7.24: Mg based $\bar{r}$ versus CO_2 Mass Fraction

Aluminum Effect on Regression Rate

Regression rate of Al based experiments are quite scattered. Table 7.6 summarizes selected data for the regression rate comparison. Also, data points are presented in Figure 7.25. CO_2 addition decreases the regression rate.

Regression rate reduction decreases at high mass fluxes due to the CO_2 addition. For instance, at the 132 kg/m^2s, $\bar{r}$ decreases as 5% by CO_2 addition through 16%. Carbon dioxide addition fosters the reduction even further, 7.6% by CO_2 addition to 33%. Similar reduction can also be seen for higher fluxes such as 146 and 152 kg/m^2s. Figure 7.25 shows an outlier data pair at 105 kg/m^2s. At this flux value, increasing the CO_2 from 0 to 33% increases the regression rate for 9.4%.

7.3.4 MMT The Relative Error Analysis

Relative error analysis is made due to [49]. The error in regression rate of experiments changes between 0.1 and 0.26. Relative error in regression rate depends on sensitivity of caliper and scales. Caliper and scale have sensitivity of 0.01 used grain mass and dimension measurements. In addition, relative error in burn time also affects the regression rate that is considered as 0.1% due to sensitivity of DAQ

Table 7.6: CO_2 Effect on Regression Rate - Al Cases

Test #	$\boldsymbol{CO_2}$ **(%)**	$\overline{\dot{G}}_{ox}$ $\boldsymbol{(kg/m^2s)}$	$\overline{\dot{r}}$ $\boldsymbol{(mm/s)}$
1	21.14	84.27	1.14
2	33.80	90.3	0.88
3	0	103.56	1.06
4	33.80	107.5	1.16
5	0	133.36	0.92
6	16.65	133.56	0.87
7	33.80	131.22	0.85
8	0	146.58	0.97
9	16.65	147.31	0.90
10	0	150.93	1.18
11	21.14	153.13	1.01

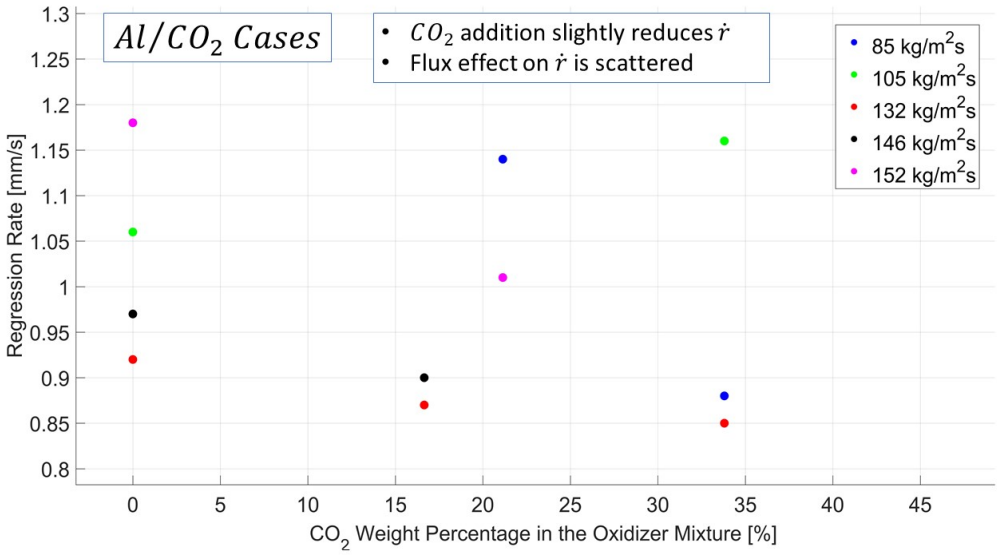

Figure 7.25: Al based $\dot{r}$ versus CO_2 Mass Fraction

system. Relative error in average mass flux changes between 0.14 and 0.5. Mass flux measurement depends on relative error in port diameter at thrust termination,

initial port diameter and oxidizer flow rate. Port diameter related error factors are considered as 0.01 due to scale/caliper sensitivities. Relative error related to oxidizer mass flow rate is directly proportional with relative errors of average feed pressure, injector diameter, discharge coefficient and ambient temperature. Relative errors related to combustion efficiency and characteristic velocity are another important factor for the accuracy of the experiments. Both error values are found around 0.025. All these error factors are discussed in the Appendix A . All equipment used in the measurements are calibrated and certified.

Chapter 8

MARS ASCENT VEHICLE PROPULSION SYSTEM EVALUATION

This chapter aims to provide an insight of Mars Ascent Vehicle propulsion system by using in-situ CO_2. Details of propulsion system design are presented for sustainable Martian operations. $Paraffin/Mg/CO_2/N_2O$ propellant combination requires two stage rocket to fulfill the delta-V requirement to reach the 500 km Low Mars Orbit (LMO). However, preliminary concept design uses single stage rocket for ballistic hopper missions.

In addition, earth based mass over payload mass (M_{earth}/M_{pl}) is minimized due to the carbon dioxide percentage. M_{earth} minimization is achieved at 60% CO_2 for Mg80 fuel grain. This means that, 40% of the oxidizer (nitrous oxide) is transported from the Earth. 20% of the fuel grain (paraffin) is brought from the Earth.

8.1 MAV Propulsion System Literature Review

There are many MAV design concepts using hybrid rockets studied by many researchers. These studies provide practical experiments to evaluate in-situ propellant usage for the Mars. Carter [50] discussed technology requirements for propulsion systems such as displacement pumps and bladder lined composite tanks. One of the experimental works for a potential MAV is presented by Karp with paraffin-based fuel and Mixed Oxides of Nitrogen (MON-3) oxidizer [51]. Karp proposes hybrid rocket based MAV with 346 kg gross lift-off mass, 57 cm outer diameter, and 2.9 m length. Furthermore, Evans and Karabeyoglu also studied MON based oxidizer for MAV experiment with metallized SP7 fuel by using 30 microns sized aluminum powder [52]. They performed various of experiments by using hybrid motor with

68 mm outer grain diameter. SP7 paraffin-based solid fuel is developed by Space Propulsion Group, Inc., specifically for this program.

8.2 MAV Earth Based Propellant Mass Optimization

In-situ CO_2 as an oxidizer compound has advantages of reduced mass and cost for MAV propulsion systems. This section explains an optimization process in order to understand the positive impacts of in-situ CO_2 for MAVs. Optimization process finds minimum brought mass (from the Earth) value over a specific payload mass (M_{earth}/M_{pl}). NASA CEA is used for the optimization process. Minimum value of M_{earth}/M_{pl} is shown according to the carbon dioxide mass fraction. Combustion and nozzle efficiencies are considered perfect (100% efficiency) for the theoretical analysis. Motor chamber pressure is taken as 38 bars with an area ratio of 50. Optimization assumes single staged rocket with ΔV_{del} of 1600 m/s. Structural mass ratio (ϵ) is taken as 0.26. Details of calculation process is explained in Appendix C.

Although this thesis uses Mg60 fuels for motor ignitions, smaller mass fractions of M_{earth}/M_{pl} is obtained at Mg80 fuel grain. Therefore, this section focuses on $Mg80/CO_2$ propellant combination for the optimization process.

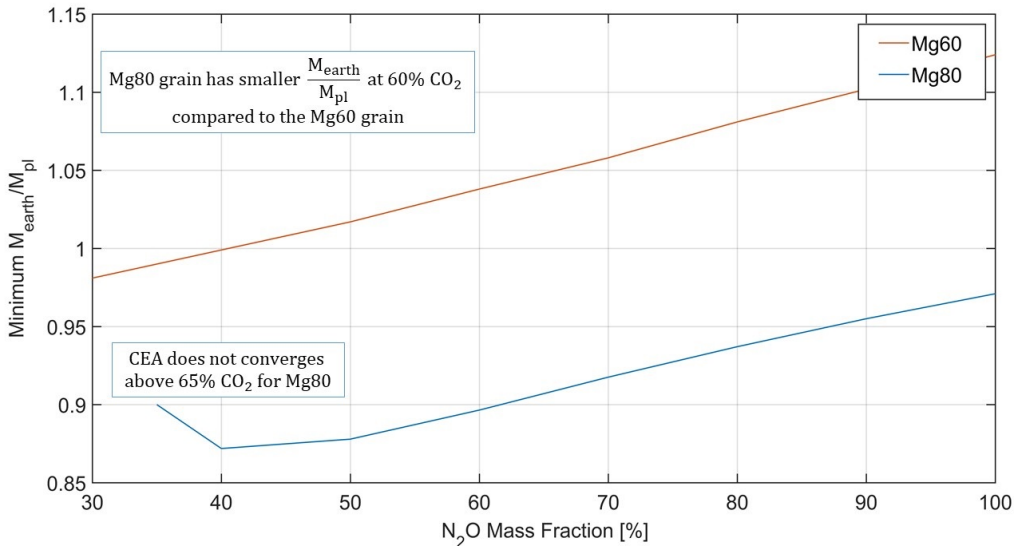

Figure 8.1: Earth Based Mass Fraction Minimization due to the O/F

Figure 8.1 shows the minimum values of M_{earth}/M_{pl} due to nitrous oxide mass fractions. Practically, casting of Mg80 with 20% paraffin binder is a difficult process. New casting methodologies will be studied for subsequent experiments.

Figure 8.2 shows M_{earth}/M_{pl} fraction due to O/F ratio. Various of CO_2 fractions are presented in this figure. According to Figure 8.2, minimum value is achieved for 60% CO_2 as 0.88. Although high carbon dioxide level seem practical for an in-situ rocket, 60% CO_2 minimizes the nitrous mass which is needed to brought from the Earth (M_{earth}). Minimum values are achieved around $O/F = 2$.

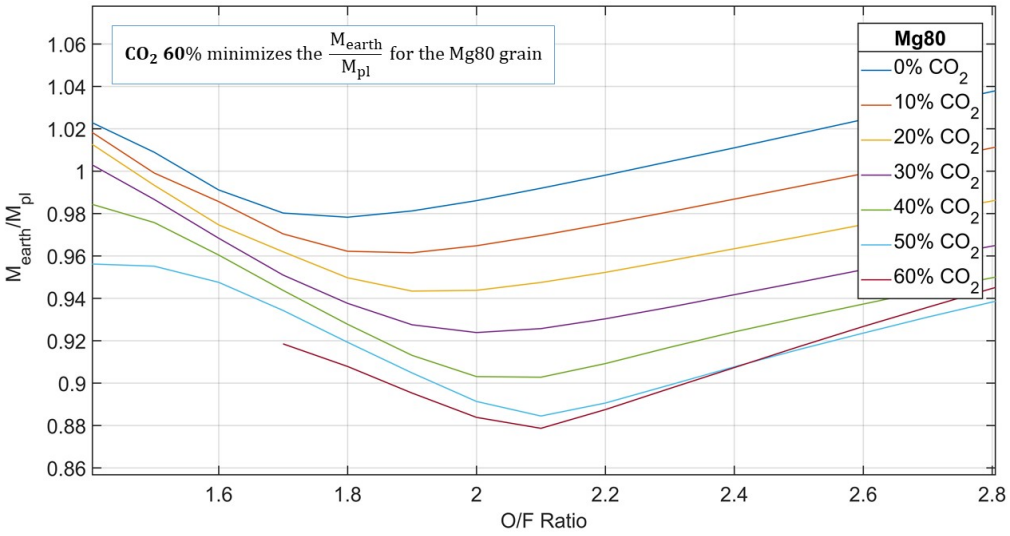

Figure 8.2: Earth Based Mass Minimization due to various CO_2 Mass Fractions

In addition, Figure 8.3 summarizes minimized M_{earth}/M_{pl} due to nitrous oxide mass fraction. M_{earth}/M_{pl} points are taken at optimum O/F values obtained by CEA. Both aluminum and magnesium mass fractions at 80% are presented. Al80 grain has slightly better fraction values. However, Al80 ignition provides challenging ignition with above 40% CO_2.

Optimizatipn Sensitivity due to the Structural Mass Ratio

Sensitivity of M_{earth}/M_{pl} is calculated by changing the rocket structural mass ratio, ϵ. The current optimization takes Structural mass ratio (ϵ) as 0.26. With this value,

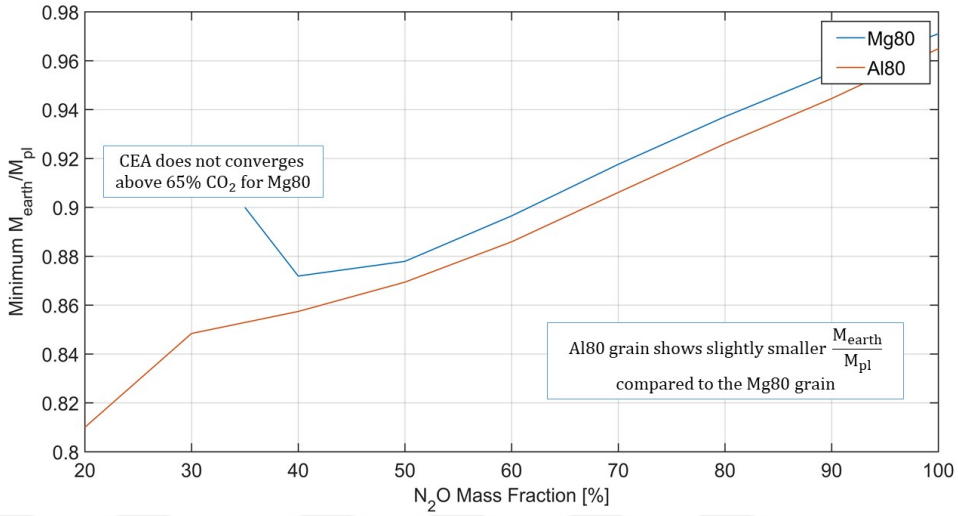

Figure 8.3: Earth Based Mass Minimization of Al and Mg versus N_2O Mass Fraction

Figure 8.2 shows the minimum M_{earth}/M_{pl} as 0.89. Structural mass ratio versus M_{earth}/M_{pl} is summarized in Figure 8.4.

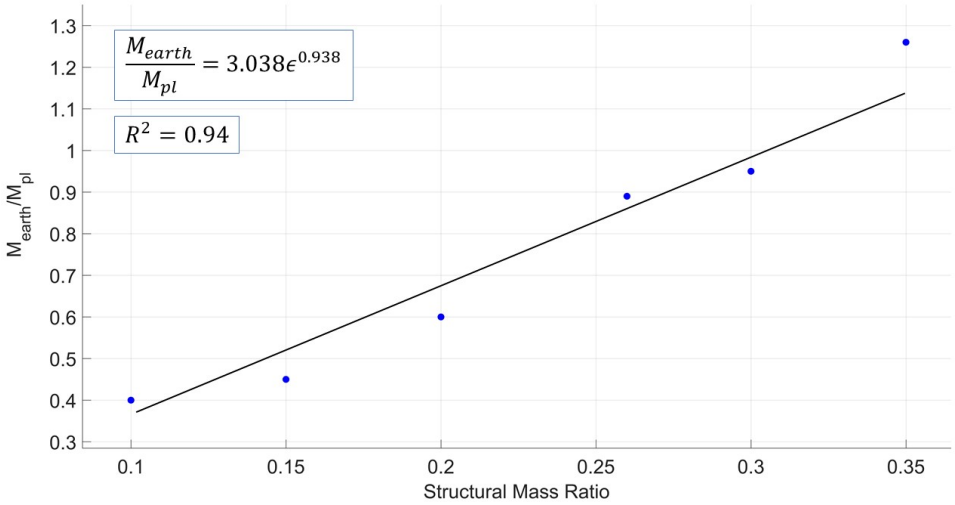

Figure 8.4: Earth Based Mass Minimization due to Structural Mass Ratio

ϵ changes between 0.1 and 0.35 with the step size of 0.5. Increasing ϵ linearly increases the M_{earth}/M_{pl}. Sensitivity of the optimization is given in Figure 8.4. Minimum M_{earth}/M_{pl} values consist of Mg80 and 60% CO_2 combination.

8.3 MAV ΔV Evaluation

$Paraffin/Mg/CO_2/N_2O$ propellant combination needs two staged rocket to fulfill the delta-V requirement to access 500 km altitude. Required delta-V for 500 km low Mars orbit is 4300 meters per seconds. However, a 240 kg single staged rocket has delivered delta-V (ΔV_{del}) of 3947.1 meters/seconds as discussed in Section 8.4.

The ΔV_{del} of the single staged hybrid sounding rocket is found in Eq. 8.1. α_{TVC} is the thrust vector angle, $M_{initial}$ is the initial rocket mass (can also be gross lift-off mass) in kg, M_{bo} is the burn-out mass which is obtained after all propellant is consumed in kg.

$$\Delta V_{del} = I_{sp} g_0 \cos(\alpha_{TVC}) \ln(\frac{M_{initial}}{M_{bo}}) \tag{8.1}$$

ΔV_{del} term must be equal to delta-V budget due to orbital velocity, potential energy, gravity loss, drag loss and the planet's rotation.

Orbital velocity refers the kinetic energy component which is shown as in Eq. 8.2. The μ_{mars} is the gravitational constant of Mars $0.0428 \times 10^6\ km^3/s^2$. R_{mars} is the Mars's radius 3396.2 km. And the h is the altitude in which the rocket targets ($h = 500km$ in this case).

$$\Delta V_{co} = \sqrt{\frac{\mu_{mars}}{R_{mars} + h}} \tag{8.2}$$

The potential energy term is also reversible thus uses the following relation,

$$\Delta V_{pot} = \sqrt{\frac{\mu_{mars}}{R_{mars}}} \sqrt{2 - \frac{R_{mars}}{R_{mars} + h}} \sqrt{\frac{\mu_{mars}}{R_{mars} + h}} \tag{8.3}$$

For the $h \ll R_{mars}$ the term is stated in linear form.

$$\Delta V_{pot} \cong \frac{h}{R_{mars}} \sqrt{\frac{\mu_{mars}}{R_{mars}}} \tag{8.4}$$

The gravity loss term is irreversible and depend on the burn time (t_{burn}) and trajectory angle with respect to local horizon (γ_{tvc}). Trajectory angle is selected as 75°.

$$\Delta V_{grav} = \int_0^{t_{burn}} gsin\left(\gamma_{tvc}\right) dt \tag{8.5}$$

The drag loss changes with the drag force (D), initial rocket mass ($M_{initial}$) and the burnout time (t_{burn}).

$$\Delta V_{drag} = \int_0^{t_{burn}} \frac{D}{M} dt \tag{8.6}$$

The drag force in Eq 8.6, requires the drag coefficient of the rocket. The drag coefficient can be estimated by using Missile datcom or CFD analysis due to the rocket aerodynamic design. In this study, the drag loss is assumed as 100 m/s. Algorithm will be evaluated for subsequent studies.

Another factor of required delta-V calculation is due to Mars's rotation. Velocity increment due to rotation can be found in Eq. 8.7.

$$\Delta V_{rot} = V_M \sin\left(Az\right) \ = V_M \frac{\cos(i)}{\cos(La)} \tag{8.7}$$

$Az,\ La,\ and\ i$ refer the initial azimuth, latitude and inclination angles due to the launch site. Azimuth and latitude are assumed as 80 and -4.5 degrees.

The Mars's rotation velocity (V_M) equals,

$$V_M = V_M^m \cos(La) \tag{8.8}$$

V_M^m is 241.172 meters per seconds. Thus,

$$\Delta V_{rot} = V_M^m \cos(La) \tag{8.9}$$

The delta-V budget ($\Delta V_{del} = \Delta V_{req}$) presented in the following equations.

$$\Delta V_{req} = \Delta V_{co} + \ \Delta V_{pot} + \Delta V_{grav} + \Delta V_{drag} - \Delta V_{rot} \tag{8.10}$$

Thus, for the n staged rocket with mass ratio of μ_i,

$$\Delta V_{req} = \Delta V_{del} = \sum_{i=1}^{n} I_{sp,i} g_0 \cos(\alpha_{TVC}) \ln(\mu_i) \tag{8.11}$$

8.4 Single Stage Mars Sounding Rocket Evaluation

Hybrid propulsion system by using $Paraffin/Mg/CO_2/N_2O$ propellant combination is totally feasible for Mars Ascent Vehicles. In-situ propellant combination provides significant cost savings as well as ease of manufacturing on Mars. Only 20% fuel and 40% oxidizer are needed to be brought from the Earth. Magnesium and CO_2 can be extracted on the Mars. Martian atmosphere consist of 96% carbon dioxide. In additon, 5% of Martian surface includes Mg due to Boiron [13]. Hybrid propulsion system for Martian operation provides several advantages. Self-pressurizing capability of oxidizers make the rocket simple and safe. Wide range of launch windows are available for self-pressurizing oxidized rocket. For example, oxidizer tank pressure becomes 45 bars at 15℃, summer periods of the Mars. Paraffin wax and nitrous oxide is taken from the Earth easily. Furthermore, reduction in oxidizer to fuel ratio makes the Al 6061 based tank lighter.

In this section, a sounding Mars rocket is designed for hopper missions. Magnesium mass fraction is used as 80%. Carbon dioxide mass fraction is taken as 60% in the oxidizer mixture. Burn time and burnout distances are presented by using 2-DOF trajectory analysis. Details of 2-DOF equations are presented in Appendix D. Performance parameters such as thrust and specific impulse is calculated by using CEA.

A hybrid rocket motor with a 38 bars combustion pressure, 99% of combustion efficiency, 5 kg/s of oxidizer mass flow rate and nozzle area ratio of 50 provides 270

seconds of specific impulse at an oxidizer to fuel ratio (O/F) of 2. Also, the thrust level of this single motor is found as 20 kN. Sounding rocket has 150 mm fuel grain inner diameter and 260 mm outer diameter. Fuel length is assumed as 800 mm. The density of $80\%Mg/20\%Paraffin$ fuel is 1475 kg/m^3. Therefore, grain mass equals 53 kg. It means that only 10 kg paraffin is taken from the Earth. In addition, oxidizer mass becomes 106 kg with the $O/F = 2$. Thus, total propellant mass corresponds 159 kg. Oxidizer tank mass is 23 kg with Al 6061 design. Length of the tank is 2 meters. In addition, 2 kg payload mass is assumed to transfer a sample from a point to another on the Mars. Structure mass of the rocket is estimated as 18 kg consist of motor interface, motor casing, measurement devices and the oxidizer feed system (plumbing and valves). Avionics and power system is 5 kg. Nosecone is 2 kg.

Detail dimensions as well as performance of a possible Mars sounding rocket is explained in Table 8.1. Subscript r refers the 'rocket' in parameters such as $M_{ox,\ r}$; rocket oxidizer mass.

It is worth to note that, oxidizer tank mass is depending on the density of the oxidizer at 50 bars. Saturated oxidizer mixture at 50 bars need the tank temperature of 15℃. Mars atmospheric temperatures are changing between $-70\ and\ 20$℃ near the equator. Thus, a heater system with a simple thermostat can be used at night times to increase the temperature to 15℃. On the other hand, launch can be performed in Martian summer days such as July or August.

The sounding rocket has 24 seconds burn time and the mass ratio $\left(n_s = \frac{M_{initial}}{M_{bo}}\right)$ of 4. 2-DOF calculation shows that rocket have 7.15 km downrange distance with 25.15 km burn out altitude. Velocity at burnout is 3.5 km/s. The initial flight path angle γ_{tvc} is taken as 75°. Details of 2-DOF calculations are presented in Appendix D. However, 3-DOF calculation is needed in order to increase the precision for the launch.

Table 8.1: Performance Parameters of Mars Sounding Rocket Concept

Parameter- Unit	**Value**	**Parameter Name**
$T,\ kN$	20	Thrust
$I_{sp},\ s$	270	Specific Impulse
$\overline{O/F}$	2	Oxidizer to Fuel Ratio
$M_{ox,\ r},\ kg$	94	Oxidizer Mass
$M_{f,\ r},\ kg$	47	Fuel Mass
$M_{tank,\ r},\ kg$	23	Oxidizer Tank Mass
$M_{s,\ r},\ kg$	18	Structural Mass
$M_{nose,r},\ M_{av,\ r},\ kg$	7	Nosecone plus Avionics Mass
$M_{pl,\ r},\ kg$	2	Payload Mass
$M_{tot,\ r},\ kg$	191	Total Initial Mass
$L_{tank,\ r}\ ,\ L_{fuel,\ r},\ m$	0.8, 2	Fuel and Tank Length
$\dot{m}_{ox,\ r},\ kg/s$	5	Oxidizer Flow Rate

Chapter 9

CONCLUSION

This thesis investigates the ignition limit of CO_2 by using $Paraffin/Metal$ fuel in a classical hybrid rocket. Small scale experiments provide maximum ignition limit of 43% CO_2 by mass in the oxidizer mixture for Aluminum powder. Scale up experiments showed that magnesium has easier ignition capability with CO_2 than the aluminum. Maximum successful ignition is achieved up to 75% CO_2. Scale up tests performed in oxidizer mass flux values between 50 *and* 260 kg/m^2s. Maximum successful flux rate is achieved at 74 kg/m^2s for the 75% CO_2.

One significant outcome of this thesis is that CO_2 addition slows down the chemical kinetics. Gas phase reactions become impractical at high CO_2 mass fractions. It means that, CO_2 reduces the adiabatic flame temperature during combustion. Motor chamber temperature drops significantly from 3500 K to 1700 K with the CO_2 addition. 1600 K is the ignitibility limit and ignition quenches below 1600 K flame temperature.

This thesis concludes that in-situ based $Paraffin/Mg/CO_2/N_2O$ is the most prominent candidate for Martian transportation vehicles. Martian vehicle with hybrid propulsion provides low cost, safe launch operations, ease of manufacturing, and ease of design. In-situ CO_2 usage significantly reduces the mass needed to be brought from the Earth. Although ignitions can be performed for up to 75% CO_2, the Earth based mass is minimized at 60% CO_2 for Mg80 fuel grain. 20% of fuel grain that is paraffin wax is stored from the Earth. Casting of Mg80 grain is not practical thus experiments only covers Mg60 fuel grains. Mg80 fuel casting methods will be evaluated for upcoming experiments.

Chapter 10

FUTURE WORK

This study indicates that CO_2 can burn with metallic powdered fuels by using classical hybrid rocket design. However, advanced internal ballistics improvements are needed in order to achieve higher mass fractions for CO_2. Increasing adiabatic flame temperature is significant inside the motor.

Therefore, there are several methods that can be considered such as (i) magnesium additive mass fraction increase in paraffin wax (up to 80%), (ii) aft injection methodologies to increase adiabatic flame temperature, (iii) Potassium nitrate addition into the fuel grain, and (iv) angled or swirl injection methods. All these methods are currently being used by hybrid propulsion community to improve internal ballistics during the combustion.

A post-test image for angled injector experiment is shown in Figure 10.1. This image clearly shows that fuel grain is scraped by the oxidizer flow. Fuel droplets merge with oxidizer flow aggressively. Combustion may not increase T_{flame}, but it can make an impact with easier ignition.

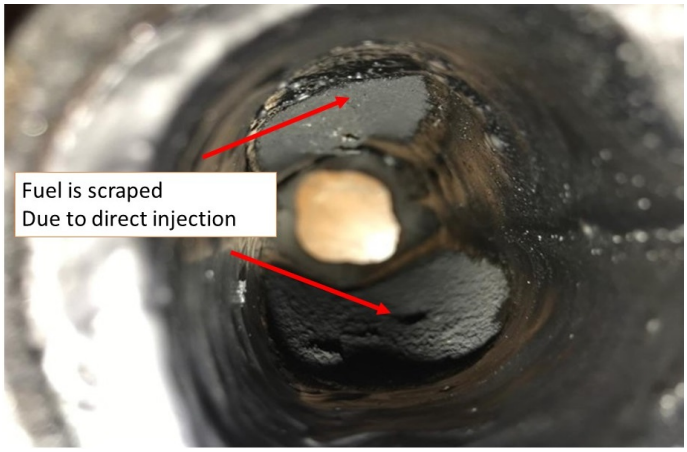

Figure 10.1: Angled Injection Effect on Fuel Grain

Several experiments are performed for preliminary analysis of angled injection. The injector has 4 holes with 15 degrees. The effect of direct injection is presented in Table 10.1.

Table 10.1: Effect of the Angled Injector on Regression Rate

FUEL	CO_2 %	$\overline{G}_{ox}$ (kg/m^2s)	$\overline{\dot{r}}$ (mm/s)
MMT77	0	72.86	0.95
MMT78 angled	0	67	1.22
MMT82 angled	34	54.93	0.98
MMT83	34	63.83	0.78

In Table 10.1, MMT77 and MMT78 are Paraffin/Nitrous experiments without metallic additive. With the similar flux value and O/F ratio, regression rate is increased by 28% by using angled injector. MMT82 and MMT83 show 60% Mg loaded experiments. CO_2 mass fraction is 34% in the oxidizer mixture. Similarly, angled injector motor provides 25% increase in the regression rate.

In addition, increasing magnesium mass fraction up to 80 or 85% is another method for increased T_{flame}. High shear mixer cannot be used fuel grains consist over 50% metal additive. Therefore, an alternative fuel casting methodology is needed for 80% magnesium fuels. One method is to use ball milling or sintering technique. Metal/Paraffin fuel can be mixed by ball milling. Then, the fuel can be casted in a pressurized mold. For 70% CO_2, 80% Mg fuel increases T_{flame} from 1700K to 2600K at $O/F = 3$. In addition, Earth based mass fraction is obtained at 50% CO_2 for Mg80 fuel grain. Additional experiments can be performed to verify the optimization process. 50% CO_2 concentration is already in successful ignition zone for the Mg80.

Theoretical calculations showed that maximum adiabatic flame temperature is achieved at $OF = 1$. Therefore, scale up motor can be designed for optimum O/F tests. However, CCP formation is one issue for low oxidizer to fuel ratios.

Aft injection and potassium nitrate addition into the fuel are two possible methods for increased flame temperature during the combustion. Although KNO_3 provides easier ignition with carbon dioxide, it does not have positive contribution to T_{flame}. Aft injection requires additional calculations on internal ballistics.

BIBLIOGRAPHY

[1] NASA Mars Exploration Program News, "Odyssey finds water ice in abundance under mars' surface," https://mars.nasa.gov/news/247/odyssey-finds-water-ice-in-abundance-under-mars-surface/, 2002.

[2] S. Marchi, "A new martian crater chronology: Implications for jezero crater," https://arxiv.org/abs/2102.05625, 2021.

[3] A. Grau Galofre, A. Jellinek, and G. Osinski, "Valley formation on early mars by subglacial and fluvial erosion," *Nature Geoscience volume*, vol. 13, pp. 663 – 668, 2020, https://doi.org/10.1038/s41561-020-0618-x.

[4] C. R. Webster, P. R. Mahaffy, S. K. Atreya, G. J. Flesch, M. A. Mischna, P.-Y. Meslin, K. A. Farley, P. G. Conrad, L. E. Christensen, A. A. Pavlov, J. Martín-Torres, M.-P. Zorzano, T. H. McConnochie, T. Owen, J. L. Eigenbrode, D. P. Glavin, A. Steele, C. A. Malespin, P. D. Archer, B. Sutter, P. Coll, C. Freissinet, C. P. McKay, J. E. Moores, S. P. Schwenzer, J. C. Bridges, R. Navarro-Gonzalez, R. Gellert, and M. T. Lemmon, "Mars methane detection and variability at gale crater," *Science, American Association for the Advancement of Science*, vol. 347, no. 0094-5765, pp. 415 – 417, 2015, https://doi.org/10.1126/science.1261713.

[5] NASA's Mars Exploration Program, "The red planet," https://mars.nasa.gov, 2021.

[6] NASA technical report Rapid (Explosive) Decompression Emergencies in Pressure-Suited Subjects, "Human body in vacuum," https://web.archive.org/web/20141014072430/http://imagine.gsfc.nasa.gov/docs/ask_astro/answers/970603.html, 1997.

[7] Dryden Flight Research Center, "A brief history of the pressure suit," https://web.archive.org/web/20160325173807/http://www.nasa.gov/centers/dryden/research/AirSci/ER-2/pshis.html, 2016.

[8] W. J. F. Koning, E. A. Romander, and W. Johnson, "Low reynolds number airfoil evaluation for the mars helicopter rotor," *AHS International 74th Annual Forum and Technology Display*, vol. Phonix, Arizone, USA, 2018, https://rotorcraft.arc.nasa.gov/Publications/files/Koning_Romander_Johnson_Low_Reynolds_Number_Airfoil_Evaluation_FINAL_ARC.pdf.

[9] T. Desert, J. Moschetta, and H. Bézard, "Aerodynamic design of a martian micro air vehicle," *7TH European Conference for Aeronautics and Aerospace Sciences (EUCASS)*, 2017, https://doi.org/10.13009/EUCASS2017-365.

[10] O. Kara, H. Karakas, and A. Karabeyoglu, "Hybrid rockets with mixed N_2O/CO_2 oxidizers for mars ascent vehicles," *Acta Astronautica*, vol. 175, no. 0094 - 5765, pp. 254 – 267, 2020, https://doi.org/10.1016/j.actaastro.2020.05.060.

[11] G. P. Sutton and O. Biblarz, *Rocket Propulsion Elements*, ser. 9th Edition. Wiley, Hoboken, NJ, 2016.

[12] M. Chiaverini and K. Kuo, *Fundamentals of Hybrid Rocket Combustion and Propulsion (Progress in Astronautics and Aeronautics)*, ser. 1st Edition. AIAA, March 15, 2007.

[13] B. McBride, M. J. Zehe, and S. Gordon, "The nasa cea (chemical equilibrium with applications," in *NASA Glenn Coefficients for Calculating Thermodynamic Properties of Individual Species*, NASA TP-2002-211556 2002.

[14] R. Gelain, *CFD Simulations of Self-Pressurized Nitrous Oxide Hybrid Rocket Motors*. University of Padova, Master Thesis, 2017.

[15] D. Altman and H. Holzman, *Overview and History of Hybrid Rocket Propulsion*, ser. 1st Edition. Fundamentals of Hybrid Rocket Combustion and Propulsion, AIAA, March 15, 2007.

[16] M. A. Karabeyoglu, "Chapter 1, introduction to rocket propulsion," in *AA 284a Advanced Rocket Propulsion, Stanford University*, 2017.

[17] R. Humble, H. Gary, and W. Larson, *Space Propulsion Analysis and Design*, ser. 1st Edition. McGraw Hill, 1995.

[18] SNC Sierra Nevada Corporation, https://www.sncorp.com/who-we-are/business-areas/space-systems/.

[19] Space Propulsion Group, https://www.spg-corp.com.

[20] Rocket Lab, https://www.rocketlabusa.com.

[21] A. Karabeyoglu, D. Altman, and B. Cantwell, "Combustion of liquefying hybrid propellants: Part 1, general theory," *Journal of Propulsion and Power*, vol. 18, no. 3, 2002, https://doi.org/10.2514/2.5975.

[22] A. Karabeyoglu, B. Cantwell, and J. Stevens, "Evaluation of homologous series of normalalkanes as hybrid rocket fuels," in *41st Joint Propulsion Conference and Exhibit*, July 2005, https://doi.org/10.2514/6.2005-3908.

[23] A. Karabeyoglu and U. Arıkan, "Evaluation of fuel additives for hybrid rockets and sfrj systems," in *50th Joint Propulsion Conference*, July 2014, https://doi.org/10.2514/6.2014-3647.

[24] A. Karabeyoglu, J. Dyer, J. Stevens, and B. Cantwell, "Modeling of N_2O decomposition events," in *44th Joint Propulsion Conference and Exhibit*, July 2008, https://doi.org/10.2514/6.2008-4933.

[25] A. J. Boiron and B. Cantwell, "Hybrid rocket propulsion and in-situ propellant production for future mars missions," in *49th Joint Propulsion Conference*, July 2013, https://doi.org/10.2514/6.2013-3899.

[26] I.Gökalp and E. Shafirovich, "The concept of a rocket engine using CO_2/metal propellant for mars sample return mission," in *3rd International Conference*, 10-13 October 2000.

[27] R. Zubrin, "Diborane/CO_2 rockets for use in mars ascent vehicles," in *31st Joint Propulsion Conference and Exhibit*, July 1995, https://doi.org/10.2514/6.1995-2640.

[28] Y. Li, C. Hu, X. Zhu, J. Hu, X.Hu, C. Li, and Y. Cai, "Experimental study on combustion characteristics of powder magnesium and carbon dioxide in rocket engine," *Acta Astronautica*, vol. 155, pp. 334 – 349, 2019, https://doi.org/10.1016/j.actaastro.2018.11.006.

[29] NIST Chemistry Webbook, https://webbook.nist.gov/chemistry/.

[30] A. Reina, G. Colombo, L. deLuca, F. Maggi, I. Lesniak, D. Lempert, and G. Manelis, "Magnesium and aluminum ignition in co2 atmosphere," 2009, XX Italian Association of Aeronautics and Astronautics (AIDAA) Congress.

[31] E. Shafivorich and A. Varna, "Metal-co2 propulsion for mars missions: Current status and opportunities," *AIAA Journal of Propulsion and Power*, vol. 24, no. 3, 2008, https://doi.org/10.2524/1.32635.

[32] S. Yuasa and H. Isoda, "Ignition and combustion of metals in a carbon dioxide stream," *Proceedings of the Twenty-Second International Symposium on Combustion, Combustion Inst., Pittsburgh, PA*, pp. 1635 – 1641, 2019, https://doi.org/10.1016/S0082-0784(89)80175-4.

[33] E. Shafirovich and U. I. Goldshleger, "Combustion of magnesium particles in co2/co mixtures," *Combustion, Science and Technology*, vol. 84, no. 1 - 6, pp. 33 – 43, 1992, https://doi.org/10.1080/00102209208951843.

[34] A. Abbud-Madrid, A. Modak, M. C. Branch, and J. W. Diley, "Combustion of magnesium with carbon dioxide and carbon monoxide at low gravity," *AIAA Journal of Propulsion and Power*, vol. 17, no. 4, 2001, https://doi.org/10.2514/2.5816.

[35] Nanokar (Nanomaterial Powder), https://nanomaterialpowder.com.

[36] Ege Nanotek, https://www.egenanotek.com.

[37] Silverson L5M High Shear Mixer, www.silverson.com/us/products/laboratory-mixers/.

[38] Perkin Elmer TGA4000, https://www.perkinelmer.com/product/tga-4000-system-100-240v-50-60hz-n5370210.

[39] B. J. Solomon, "Engineering model to calculate mass flow rate of a two-phase saturated fluid through an injector orifice," 2011, Utah State University, All Graduate Plan B and other Reports, https://digitalcommons.usu.edu/gradreports/110.

[40] S. A. Whitmore and S. N. Chandler, "Engineering model for self-pressurizing saturated N_2O propellant feed systems," *Journal of Propulsion and Power*, vol. 26, no. 4, 2010, https://doi.org/10.2514/1.47131.

[41] J.Dyer, G. Zilliac, A. K. A. Sadhwani, E.Doran, Z. Dunnand, and K. Lohner, "Modeling feed system flow physics for self-pressuring propellants," in *43rd Joint Propulsion Conference and Exhibit*, July 2007, https://doi.org/10.2514/6.2007-5702.

[42] B. S. Waxman, J. E. Zimmerman, , B. Cantwell, and G. Zilliac, "Mass flow rate and isolation characteristics of injectors for use with self-pressurizing oxidizers in hybrid rockets," in *49th Joint Propulsion Conference and Exhibit*, July 2013, https://doi.org/10.2514/6.2013-3636.

[43] SMS Tork Valves, https://www.smstork.com.

[44] GEMS Sensors and Control, https://www.gemssensors.com/product/valve.

[45] ifm Electronics, Germany, https://www.ifm.com.

[46] Omega Thermocouples, https://www.omega.com/en-us/thermocouple-types.

[47] National Instruments DAQ system, https://www.ni.com/en-tr/shop/data-acquisition.html.

[48] Hamlet Pipe and Fitting, https://www.ham-let.com.

[49] M. A. Karabeyoglu, B. J. Cantwell, and G. Zilliac, "Development of scalable space-time average regression rate expressions for hybrid rockets," *Journal of Propulsion and Power*, vol. 23, no. 4, 2007, https://doi.org/10.2514/1.19226.

[50] P. H. Carter, F. Mitlitsky, A. H. Weisberg, J. C. Whitehead, and R. W. Humble, "Design trade space for a mars ascent vehicle for a mars sample return mission," *Acta Astronautica*, vol. 45, no. 4 - 9, pp. 311 – 318, 1999, https://doi.org/10.1016/S0094-5765(99)00148-4.

[51] A. Karp, M. Redmond, B. Nakazono, D. Vaughan, R. Shotwell, G. Story, D. Jackson, and D. Young, "Technology development and design of a hybrid mars ascent vehicle concept," *IEEE Aerospace Conference, Big Sky, MT*, 2016, https://doi.org/10.1109/AERO.2016.750083.

[52] A. Karabeyoglu and B. Evans, "Development and testing of sp7 fuel for mars ascent vehicle application," *53rd Joint Propulsion Conference, Atlanta, GA*, 2017, https://doi.org/10.514/6.2017-48313.

Appendix A

SCALE UP (MMT) DATA RESULTS

A.1 MMT Aluminum Data

Table A.1: $Paraffin/Al/N_2O$ Regression Rate

Test	$\boldsymbol{CO_2}(\%)$	$\overline{\dot{\boldsymbol{G}}_{\boldsymbol{ox}}}$ $\boldsymbol{(kg/m^2s)}$	$\overline{\dot{\boldsymbol{r}}}$ $\boldsymbol{(mm/s)}$
MMT053	0	72.04	0.95
MMT054	0	63.32	1.06
MMT055	0	133.36	0.92
MMT056	0	146.58	0.97
MMT057	0	103.56	1.06
MMT063	0	165.34	0.91
MMT064	0	199.42	1.10
MMT065	0	150.93	1.18
MMT066	0	179.49	1.44
MMT067	0	219.25	1.31
MMT068	0	198.99	1.24
MMT069	0	270.31	1.34
MMT072	0	240.66	1.38

Table A.2: $Paraffin/Al/N_2O/CO_2$ Regression Rate

Test	$\boldsymbol{CO_2}(\%)$	$\overline{\dot{\boldsymbol{G}}_{\boldsymbol{ox}}}$ $(\boldsymbol{kg/m^2s})$	$\overline{\dot{\boldsymbol{r}}}$ $(\boldsymbol{mm/s})$
MMT008	21.14	84.27	1.14
MMT009	21.14	153.13	1.01
MMT010	21.14	141.19	1.05
MMT011	21.14	118.76	0.97
MMT017	16.65	147.31	0.90
MMT018	16.65	128.09	1.06
MMT019	16.65	90.45	1.03
MMT020	16.65	134.79	0.98
MMT021	16.65	133.56	0.86
MMT022	33.80	85.22	0.87
MMT023	33.80	107.51	1.16
MMT024	33.80	131.22	0.84
MMT025	33.80	90.31	0.88
MMT032	52.70	70.27	0.31
MMT037	51.81	157.33	0.86

Table A.3: $Paraffin/Al/N_2O$ Complete Test Results

Test	**CO_2** %	**$\overline{P}_{inj}$** **bar**	**$\overline{P}_{ch}$** **bar**	**μ_{comb}**	**$\overline{O/F}$**	**$\overline{\dot{m}}_{ox}$** **g/s**	**c_d**	**T_{ch}** **K**
MMT053	0	49.52	40.68	0.70	2.99	54.62	0.30	3249.5
MMT054	0	49.80	34.22	0.63	2.38	50.00	0.37	2724.1
MMT055	0	49.03	41.17	0.84	5.42	97.49	0.27	3572.3
MMT056	0	48.02	40.24	0.81	5.63	114.82	0.26	3561.7
MMT057	0	48.67	38.25	0.76	3.89	78.71	0.30	3495.2
MMT063	0	46.13	38.37	0.80	6.77	131.34	0.25	3489.6
MMT064	0	45.67	37.94	0.78	6.08	129.28	0.25	3531.5
MMT065	0	44.47	37.32	0.78	4.89	136.83	0.23	3567
MMT066	0	45.61	38.87	0.78	4.54	138.70	0.23	3560.7
MMT067	0	42.87	31.68	0.80	6.80	219.25	0.25	3465.1
MMT068	0	46.24	37.06	0.71	5.58	137.02	0.26	3554
MMT069	0	42.17	28.62	0.61	8.10	254.75	0.30	3366.6
MMT072	0	44.15	32.76	0.71	7.14	230.96	0.27	3451.5

Table A.4: $Paraffin/Al/N_2O$ Specific Impulse and Thrust

Test	$\boldsymbol{CO_2}$ (%)	$\boldsymbol{I_{sp}(s)}$	$\boldsymbol{T(N)}$
MMT053	0	136.92	99.79
MMT054	0	116.23	83.145
MMT055	0	163.75	187.5
MMT056	0	156.98	208.49
MMT057	0	150.24	149.06
MMT063	0	151.22	223.65
MMT064	0	149.21	220.61
MMT065	0	152.12	245.99
MMT066	0	152.60	253.56
MMT067	0	150.24	351.86
MMT068	0	137.49	218.10
MMT069	0	112.98	316.93
MMT072	0	133.04	343.53

Table A.5: $Paraffin/Al/N_2O/CO_2$ Complete Test Results

Test	$\mathbf{CO_2}$ %	$\overline{\mathbf{P}}_{\mathbf{inj}}$ **bar**	$\overline{\mathbf{P}}_{\mathbf{ch}}$ **bar**	$\boldsymbol{\mu_{comb}}$	$\overline{\mathbf{O/F}}$	$\overline{\dot{\mathbf{m}}}_{\mathbf{ox}}$ **g/s**	$\mathbf{c_d}$	$\mathbf{T_{ch}}$ **K**
MMT008	21.14	47.17	28.57	0.56	2.98	74.35	0.42	2659.7
MMT009	21.14	44.96	37.34	0.67	4.89	87.43	0.33	3130.5
MMT010	21.14	49.63	40.15	0.78	5.17	110.42	0.31	3164.3
MMT011	21.14	45.28	33.71	0.64	3.89	108.17	0.25	2947.1
MMT017	16.65	42.68	36.77	0.53	4.47	112.55	0.47	3196.4
MMT018	16.65	49.60	40.88	0.68	4.30	124.80	0.35	3175.2
MMT019	16.65	47.27	34.74	0.49	2.85	73.00	0.42	2757.9
MMT020	16.65	46.11	37.00	0.59	4.23	125.57	0.29	3158.2
MMT021	16.65	46.88	40.03	0.69	4.59	118.56	0.34	3217.6
MMT022	33.80	47.67	35.36	0.53	3.04	72.03	0.41	2135.8
MMT023	33.80	45.94	38.19	0.63	3.27	92.95	0.35	2336.7
MMT024	33.80	48.33	41.77	0.81	4.58	121.02	0.34	2647.9
MMT025	33.80	52.21	49.40	1.28	3.26	83.18	0.18	2335.6
MMT032	52.70	50.42	44.23	2.25	4.44	27.19	0.15	2576.7
MMT037	51.81	47.23	32.61	0.80	5.32	107.69	0.30	2657.6

Table A.6: $Paraffin/Al/N_2O/CO_2$ Specific Impulse and Thrust

Test	$\boldsymbol{CO_2}$ (%)	$\boldsymbol{I_{sp}(s)}$	$\boldsymbol{T(N)}$
MMT008	21.14	96.41	94.77
MMT009	21.14	119.53	124.10
MMT010	21.14	139.21	181.7
MMT011	21.14	113.73	152.55
MMT017	16.65	96.10	124.22
MMT018	16.65	124.23	188.11
MMT019	16.65	88.75	82.60
MMT020	16.65	108.09	165.11
MMT021	16.65	125.87	179.26
MMT022	33.80	104.06	83.24
MMT023	33.80	107.51	125.12
MMT024	33.80	132.60	193.21
MMT025	33.80	210.14	228.90
MMT032	52.70	336.35	104.99
MMT037	51.81	118.99	150.0

A.2 MMT Magnesium Data

Table A.7: $Paraffin/Mg/N_2O$ Regression Rate

Test	$\boldsymbol{CO_2}(\%)$	$\overline{\dot{\boldsymbol{G}}}_{\boldsymbol{ox}}$ $(\boldsymbol{kg/m^2s})$	$\overline{\dot{\boldsymbol{r}}}$ $(\boldsymbol{mm/s})$
MMT084	0	49.33	0.61
MMT085	0	45.36	0.53
MMT086	0	56.02	0.58
MMT104	0	149.31	1.01
MMT087	0	78.06	0.59

Table A.8: $Paraffin/Mg/N_2O/CO_2$ Regression Rate

Test	$\boldsymbol{CO_2}(\%)$	$\overline{\dot{\boldsymbol{G}}_{\boldsymbol{ox}}}$ $(\boldsymbol{kg/m^2s})$	$\overline{\dot{\boldsymbol{r}}}$ $(\boldsymbol{mm/s})$
MMT033	52.70	66.501	0.55
MMT035	51.81	143.40	0.94
MMT036	51.81	213.52	1.05
MMT041	64.628	120.16	0.59
MMT043	64.628	80.41	0.79
MMT044	64.628	95.66	0.77
MMT046	68.66	58.55	0.65
MMT047	68.66	74.10	0.66
MMT048	74.80	73.46	0.61
MMT073	34.76	95.91	0.79
MMT074	34.76	94.81	0.74
MMT088	45.34	74.00	0.61
MMT089	45.34	136.23	0.73
MMT090	45.34	54.66	0.68
MMT091	45.34	230.55	0.70
MMT092	53.09	176.52	0.73
MMT093	53.09	86.88	0.59
MMT094	53.09	180.94	1.14
MMT095	60.85	72.83	0.52
MMT096	60.85	54.86	0.62
MMT097	60.85	141.34	0.63
MMT098	60.85	209.11	0.79
MMT099	70.00	102.31	0.50
MMT100	70.00	98.20	0.80
MMT101	70.00	190.39	0.97

Table A.9: $Paraffin/Mg/N_2O$ Complete Test Results

Test	$\mathbf{CO_2}$ %	$\overline{\mathbf{P}}_{\mathbf{inj}}$ **bar**	$\overline{\mathbf{P}}_{\mathbf{ch}}$ **bar**	$\boldsymbol{\mu_{comb}}$	$\overline{\mathbf{O/F}}$	$\overline{\dot{\mathbf{m}}}_{\mathbf{ox}}$ **g/s**	$\mathbf{c_d}$	$\mathbf{T_{ch}}$ **K**
MMT084	0	50.21	40.58	1.37	2.76	32.94	0.19	3450.4
MMT085	0	47.32	43.7	1.58	2.99	31.42	0.18	3462.5
MMT086	0	48.70	47.52	1.79	3.21	36.32	0.13	3538.3
MMT087	0	48.01	47.04	2.28	4.26	48.07	0.10	3505.6
MMT104	0	42.56	29.70	0.63	5.16	108	0.32	3430

Table A.10: $Paraffin/Mg/N_2O$ Specific Impulse and Thrust

Test	$\boldsymbol{CO_2}$ (%)	$\boldsymbol{I_{sp}(s)}$	$\boldsymbol{T(N)}$
MMT084	0	256.92	112.96
MMT085	0	297.03	122.02
MMT086	0	337.94	157.78
MMT104	0	119.49	151.59
MMT087	0	424.92	247.08

Table A.11: $Paraffin/Mg/N_2O/CO_2$ Complete Test Results

Test	$\mathbf{CO_2}$ %	$\overline{\mathbf{P}}_{\mathbf{inj}}$ **bar**	$\overline{\mathbf{P}}_{\mathbf{ch}}$ **bar**	$\boldsymbol{\mu_{comb}}$	$\overline{\mathbf{O/F}}$	$\overline{\dot{\mathbf{m}}}_{\mathbf{ox}}$ **g/s**	$\mathbf{c_d}$	$\mathbf{T_{ch}}$ **K**
MMT033	52.70	50.08	45.20	0.94	3.09	47.10	0.35	2449.9
MMT035	51.81	49.29	40.02	0.74	5.03	101.38	0.37	2636
MMT036	51.81	48.10	37.82	0.86	6	116.53	0.32	2667.3
MMT041	64.62	43.15	33.91	0.70	5.83	77.31	0.45	2101.5
MMT043	64.62	51.57	39.59	0.84	2.99	64.42	0.35	1985.9
MMT044	64.62	51.76	39.29	0.91	3.02	59.30	0.32	1987.5
MMT046	68.66	50.51	40.68	0.99	2.37	44.79	0.33	1814.7
MMT047	68.66	52.09	45.67	1.09	2.98	57.74	0.32	1821.1
MMT048	74.79	46.20	33.48	0.94	2.63	41.83	0.31	1575
MMT073	34.76	44.67	44.36	1.34	3.48	95.92	0.18	3082.1
MMT074	34.76	48.76	44.42	1.24	3.63	80.03	0.22	3247.1
MMT088	45.34	49.22	47.25	1.94	2.963	61.46	0.13	2721.3
MMT089	45.34	48.43	39.70	0.94	5.17	136.23	0.25	2871.5
MMT090	45.34	51.48	45.96	1.13	2.187	43.24	0.23	2592.9
MMT091	45.34	47.50	36.27	0.82	7.79	215.91	0.30	2840.1
MMT092	53.09	43.27	35.64	0.98	6.12	161.86	0.27	2622.4
MMT093	53.09	48.29	42.56	0.83	3.55	66.28	0.37	2485.2
MMT094	53.09	46.49	39.29	1.18	4.64	158.38	0.22	2549.2
MMT095	60.85	44.49	34.96	1.16	3.37	54.10	0.20	2156.1
MMT096	60.85	47.10	44.67	1.14	2.150	44.4	0.25	2099.2
MMT097	60.85	47.84	41.61	1.25	5.25	124.57	0.23	2242.6
MMT098	60.85	46.52	33.86	0.93	6.93	204.65	0.29	2298.1
MMT099	70.00	43.18	30.77	0.89	5.14	78.17	0.30	1812.8
MMT100	70.00	44.54	31.86	1.08	3.40	84.42	0.24	1772.7
MMT101	70.00	47.14	30.49	0.89	6.19	150.22	0.28	1832.8

Table A.12: $Paraffin/Mg/N_2O/CO_2$ Specific Impulse and Thrust

Test	$\boldsymbol{CO_2}$ (%)	$\boldsymbol{I_{sp}(s)}$	$\boldsymbol{T(N)}$
MMT033	52.70	141.61	86.53
MMT035	51.81	110.99	132.19
MMT036	51.81	128.46	171.16
MMT041	64.628	90.94	80.72
MMT043	64.628	113.38	95.49
MMT044	64.628	1122.5	94.77
MMT046	68.66	129.90	80.9
MMT047	68.66	141.50	107.46
MMT048	74.80	113.78	64.36
MMT073	34.76	225.7	236.7
MMT074	34.76	209.14	209.14
MMT088	45.34	312.01	251.35
MMT089	45.34	147.12	234.42
MMT090	45.34	180.9	111.7
MMT091	45.34	125.79	300.3
MMT092	53.09	144.2	266.1
MMT093	53.09	124.29	103.44
MMT094	53.09	173.88	328.00
MMT095	60.85	160.83	110.5
MMT096	60.85	165.35	105.5
MMT097	60.85	171.5	249.2
MMT098	60.85	125.61	288.2
MMT099	70.00	108.48	99.2
MMT100	70.00	134.9	144.4
MMT101	70.00	107.65	184.08

Appendix B

THE THEORY OF RELATIVE ERROR ANALYSIS

Diameter ratio is defined as the ratio of the port diameter at the start of the thrust termination (at the valve closing) to the final grain port diameter at the end of the total burn. d_f is the final port diameter. The exponent n is found from the average mass flux versus regression rate relation.

$$\frac{d_{vc}}{d_f} = \left[1 - \left[\frac{2\,(2n+1)}{n}\right] Re^{-T}\right]^{1/(2n+1)} \tag{B.1}$$

d_i (initial grain diameter) comes from the grain measurement via calliper before the experiment. The total burn time, t_{burn}, is determined from the pressure time trace measured by DAQ system. Nondimensional variables, R *and* T depend on the characteristic time of the feed system (τ_{fs}) which is defined as follows.

$$R = 0.25\,(\tau_{fs}/t_{burn}) \left[1 + \frac{d_i}{d_f}\right]^2 \left[1 - \frac{d_i}{d_f}\right] \tag{B.2}$$

$$T = nt_f/\tau_{fs} \tag{B.3}$$

The characteristic time for the feed system is defined as,

$$\tau_{fs} = \frac{V_{feed}}{A_{inj} N_{inj} c^*_{exp} \Gamma^2} \tag{B.4}$$

Here V_{feed} is the volume of the feed system starting from the exit of the oxidizer main valve to the inlet of the rocket motor. A_{inj} is the injector area and N_{inj} is the number of injector holes. τ_{fs} is inversely proportional to the actual characteristic velocity of the oxidizer in vapor phase. Characteristic velocity is found by using Eq. 5.10. The nondimensional parameter Γ is found as,

$$\Gamma = \sqrt{\gamma}\left[\frac{2}{\gamma+1}\right]^{(\gamma+1)/2(\gamma+1)} \tag{B.5}$$

where the γ is the ratio of specific heats of the oxidizer taken as 1.3.

Relative error for the final port diameter at the valve closing (E_{dvc}) is found by using Eq. (B6). Relative error values related to E_R and E_T are selected as 1% based on the information on the measurement systems.

$$E_{dvc} = \sqrt{E_{df}^2 + (f_R E_R)^2 + (f_T E_T)^2} \tag{B.6}$$

E_{dvc} includes sensitivity parameters f_R and f_T are written in terms of R and T as follows,

$$f_R = 2R(1 - e^{-T})/n \tag{B.7}$$

$$f_T = f_R T e^{-T}/(1 - e^{-T}) \tag{B.8}$$

The relative error related to the final diameter of fuel grain (E_{df}) is found by Eq. (B9).

$$E_{df} = 0.5(1 + d_i/d_f)\sqrt{E_{\Delta M}^2 + E_\rho^2 + E_L^2} \tag{B.9}$$

The error in final diameter can be illustrated in terms of measurement errors in fuel grain ($E_{\Delta M}$), fuel density (E_ρ) and grain length (E_L). Relative errors of mass and length are taken as, 1% respectively due to measurement precision of calliper and scales. Fuel grain density has a 6.5% error due to void formation.

The relative error for the regression rate is found based on Eq. (B10). The relative error in regression rate is written in terms of port diameter at the thrust termination (at valve closing) (E_{dvc}), initial port diameter (E_{di}) and the burn time (E_{tburn}). Measurement errors in initial port diameter is taken as 1% based on the

sensitivity of the calliper. Burn time related error is taken as 0.1% according to pressure time traces measured from the data acquisition system.

$$E_{reg} = \sqrt{\left(E_{dvc}\frac{d_{vc}/d_i}{\frac{d_{vc}}{d_i}-1}\right)^2 + \left(E_{di}\frac{1}{\frac{d_{vc}}{d_i}-1}\right)^2 + (E_{tburn})^2} \tag{B.10}$$

Similarly, relative error in oxidizer mass flux is determined by using relative error in port diameter at valve closing, initial port diameter and the oxidizer flow rate, E_{Mox}.

$$E_{GOX} = \sqrt{\left(2E_{dvc}\frac{d_{vc}/d_i}{\frac{d_{vc}}{d_i}+1}\right)^2 + \left(\frac{2E_{di}}{\frac{d_{vc}}{d_i}+1}\right)^2 + (E_{Mox})^2} \tag{B.11}$$

The relative error due to oxidizer mass flow rate (E_{Mox}) is calculated by Eq. (B12). Oxidizer mass flow rate depends on relative errors in average feed pressure (E_{press}), injector diameter (E_{inj}), injector discharge coefficient (E_{cd}) and ambient temperature (E_{temp}).

$$E_{Mox} = \sqrt{E_{press}^2 + (2E_{inj})^2 + E_{cd}^2 + 0.5E_{temp}} \tag{B.12}$$

Relative error of the oxidizer mass depends on the mass measurement of scales and injector diameter due to manufacturing. Error due to temperature is negligible. Relative error in feed system pressure and flow losses is found from Eq. (B13).

$$E_{press} = \frac{0.5\% \times 50}{\overline{P_{inj}}} \tag{B.13}$$

Injector diameter error is taken as 0.5%. Injector diameter error is comes from the production of the brass material, while machining the injector hole with approximately 0.8 mm hole diameter. Discharge coefficient error is taken 0.5%.

Relative error in combustion efficiency (E_η) is also significant for the performance analysis. Combustion efficiency depend on actual (experimental) and theocratical

characteristic velocity. Experimental characteristic velocity error is found by Eq. (B14).

$$E_{c^*_{exp}} = \sqrt{E^2_{Pch} + 2E^2_{Dth} + E^2_{mox} + E^2_{mf} + E^2_{tburn}} \tag{B.14}$$

It is related to relative error in motor chamber pressure (E_{Pch}), nozzle throat diameter (E_{Dth}), oxidizer and fuel masses (E_{mox} *and* E_{mf}) and also burn time. Relative error for the chamber pressure depends on the sensor sensitivity and maximum sensor operating pressure of 70 bar, found by Eq. (B15).

$$E_{Pch} = \frac{0.5\% \times 70}{\overline{P_{ch}}} \tag{B.15}$$

Throat diameter error, oxidizer mass and fuel grain mass errors are considered as 1% due to caliper and scale sensitivities. Burn time error is taken as 0.1%.

Relative error for the theoretical characteristic velocity ($E_{c^*_{theo}}$) is found in Eq. (B16). Relative error in O/F ratio ($E_{\overline{O/F}}$) is the key parameter for the $E_{c^*_{theo}}$. The non-dimensional slope of the theoretical characteristic velocity with respect to O/F, $f'^{(\overline{O/F})}/f(\overline{O/F})$ is another factor for calculating $E_{c^*_{theo}}$.

$$E_{c^*_{theo}} = E_{\overline{OF}}\ f'^{(\overline{OF})}/f(\overline{OF}) \tag{B.16}$$

Relative error in O/F ratio is found by Eq. (B17). Oxidizer and fuel masses are two significant factors for the $E_{\overline{O/F}}$.

$$E_{\overline{O/F}} = \sqrt{E^2_{mox} + E^2_{mf}} \tag{B.17}$$

Therefore, relative error for the combustion efficiency is found in Eq. (B18).

$$E_\eta = \sqrt{E^2_{c^*_{exp}} + E^2_{c^*_{theo}}} \tag{B.18}$$

Appendix C

EARTH BASED MASS OPTIMIZATION

This chapter explains the derivations for the optimization process of M_{earth}/M_{pl}. Derivations are started with definition of delivered delta-V by using Eq. C.1. In this equation, Specific impulse value is found from CEA software with respect to O/F. g_0 is taken as 9.81 m/s^2.

$$\Delta V_{del} = I_{sp} g_0 \ln(\frac{M_{initial}}{M_{bo}}) \tag{C.1}$$

In the Eq. C.1, $M_{initial}/M_{bo}$ is defined as the mass ratio for the rocket. The mass ratio (η) also equals the following formula. In Eq. C.2, $M_{str} + M_{prop}$ is defined as rocket gross mass (M_{gross}).

$$\eta = \frac{M_{str} + M_{pl} + M_{prop}}{M_{str} + M_{pl}} \tag{C.2}$$

$$M_{str} + M_{prop} = M_{gross} \tag{C.3}$$

In addition, ϵ is the structural mass ratio for the rocket. In the optimization process, ϵ is taken as 0.20. Eq. C.4 shows the definition of the ϵ.

$$\epsilon = \frac{M_{str}}{M_{str} + M_{prop}} \tag{C.4}$$

Mass ratio in Eq. C.2 is substituted into the Eq. C.1.

$$\frac{M_{initial}}{M_{bo}} = \frac{M_{gross} + M_{pl}}{M_{gross}\epsilon + M_{prop}} \tag{C.5}$$

Therefore, the Eq. C.1 is formed as,

$$e^{\Delta V_{del}/Ispg_0} = \frac{M_{gross} + M_{pl}}{M_{gross}\epsilon + M_{prop}} \tag{C.6}$$

Optimization process needs substitution of gross and payload masses into the earth based mass. Substitution starts with the new form of Eq. C.6. Therefore, M_{gross}/Mpl is found as,

$$\frac{M_{gross}}{M_{pl}} = \frac{e^{\Delta V_{del}/Ispg_0} - 1}{1 - \epsilon e^{\Delta V_{del}/Ispg_0}} \tag{C.7}$$

The earth based mass M_{earth} is defined as in Eq. C.8. In this equation, M_f is the fuel grain mass, M_{ox} is the oxidizer mass. The minimization process is performed due to the mass fraction of the nitrous oxide and paraffin wax. Both compounds are taken from the Earth to the Mars. α_f refers the paraffin wax mass fraction. α_{ox} is the nitrous oxide mass fraction in the CO_2/N_2O oxidizer mixture.

$$M_{earth} = \alpha_f M_f + \epsilon M_{gross} + \alpha_{ox} M_{ox} \tag{C.8}$$

Optimization is performed with respect to ΔV_{del} and O/F ratio. Therefore, Eqs. C.9 - C.12 are substituted in to the Eq. C.8.

$$M_{prop} = M_f + M_{ox} = M_{gross}(1 - \epsilon) \tag{C.9}$$

Propellant mass is derived with respect to fuel and oxidizer masses. O/F ratios is used for derivations.

$$O/F = M_{ox}/M_f \tag{C.10}$$

Thus, both fuel and oxidizer masses are used as a function of oxidizer to fuel ratio and the gross mass. Eq. C.11 shows the fuel mass.

$$M_f = \frac{1}{1 + O/F}\,(1 - \epsilon)\,M_{gross} \tag{C.11}$$

Furthermore, Eq. C.12 shows the oxidizer mass as a function of O/F and M_{gross}.

$$M_{ox} = \frac{O/F}{1+O/F}\left(1-\epsilon\right)M_{gross} \tag{C.12}$$

Finally, Eqs. C.11 and C.12 are substituted into the Eq. C.8. Earth based mass fraction with respect to payload mass M_{earth}/M_{pl} is found as,

$$\frac{M_{earth}}{M_{pl}} = \left[\frac{e^{\Delta V_{del}/Ispg_0}-1}{1-\epsilon e^{\Delta V_{del}/Ispg_0}}\right]\left[\epsilon+\left[\frac{1-\epsilon}{1+O/F}\left(\alpha_f+\alpha_{ox}O/F\right)\right]\right] \tag{C.13}$$

In Eq. C.13 structural mass ratio (ϵ) is taken as 0.25. α_f is the paraffin wax mass fraction 0.2 or 0.4 due to the propellant combination. ΔV_{del} for single stage rocket is assumed as 1600 m/s. g_0 is 9.81 m/s^2. NASA CEA performs the iterations by using O/F and carbon dioxide mass fraction $(1-\alpha_{ox})$. Eq. C.13 uses nitrous oxide mass fraction that is α_{ox}. Fractions change between 20% and 90%. In addition, CEA takes I_{sp} values due to the oxidizer to fuel ratio for Mg80 based fuel grain.

Appendix D

2-DOF TRAJECTORY ANALYSIS

This section explains the flight distances of the proposed sounding rocket on Mars. Eq. D.1 - D.4 shows the flight parameters at the burnout.

$$\frac{dv}{dt} = \frac{T}{m} - \frac{D}{m} - gsin\gamma_{tvc} \tag{D.1}$$

$$\frac{d\gamma_{tvc}}{dt} = -\frac{1}{v}(g - \frac{v^2}{R_{mars}+h})vcos\gamma_{tvc} \tag{D.2}$$

$$\frac{dx}{dt} = \frac{R_{mars}}{R_{mars}+h}vcos\gamma_{tvc} \tag{D.3}$$

$$\frac{dh}{dt} = vsin\gamma_{tvc} \tag{D.4}$$

v is the burnout velocity, γ_{tvc} is the flight path angle, h is the height at the burnout. R_{mars} is the radius of the Mars which is 3389.5 km. In Eq. D.1, m is the current vehicle mass of the rocket ($m = M_{initial} - \dot{m}_{tot}t$). D/m term is the decleration due to the drag. Eq. D.5 calculates the drag force of D. C_d is assumed as 0.5. However, detailed drag coefficient analysis is needed for further studies. A_r is the cross sectional area of the proposed rocket ($A_r = 0.25 \times \pi d_r^2$). by using diameter of the rocket (d_r) as 0.28 meters. ρ_{mars} is the density of Martian atmosphere comes from the Eq. D.9.

$$D = 0.5 \times \rho_{mars} v^2 A_r C_d \tag{D.5}$$

In addition, $gsin\gamma_{tvs}$ term refers the loss due to the gravity of the Mars. g is the the local gravitational acceleration that is found by Eq. D.6. $g_{mars} = 3.712 m/s^2$ is the gravitational constant of the Mars at the sea level.

$$g = \frac{g_{mars}}{(1 + h/R_{mars})^2} \tag{D.6}$$

Atmospheric conditions of the Mars is stated as

$$T_{mars} = -31 - 0.000998 h_{mars} \tag{D.7}$$

$$P_{mars} = 0.699\ e^{-0.00009 h_{mars}} \tag{D.8}$$

$$\rho_{mars} = P_{mars}/(0.1921 \times (T_{mars} + 273.15)) \tag{D.9}$$

Atmospheric conditions are taken from NASA MarsGram 2010 Software. Temperature and pressure of the Martian atmosphere changes according to the altitude. Density of Martian atmosphere is highly dependent on both P_{mars} and T_{mars}.

Furthermore, flight trajectory of the sounding rocket depend on the thrust (T) and the burn time (t_{burn}). Thrust of the rocket is taken as 20 kN according to the CEA calculations. Specific impulse is taken as 270 seconds.

Burn time and propellant masses by using following equations. $n_s = 4.3$ is the structural coefficient. Rocket initial mass is taken as 240 kg.

$$M_{bo} = M_{initial}/n_s \tag{D.10}$$

Propellant mass is found as,

$$M_{prop} = M_{initial} - M_{bo} \tag{D.11}$$

Propellant flow rate is also required for the burn time.

$$\dot{m}_{prop} = \frac{T}{I_{sp} g_0} \tag{D.12}$$

Thus, flight (burn) time is calculated as,

$$t_{burn} = M_{prop}/\dot{m}_{prop} \tag{D.13}$$

In the 2-DOF analysis, the initial flight path angle (γ_0) is held at 75° between liftoff and pitchover. Pitchover begins at the altitude (h_p) 150 km with the flight path angle set at 74.9°.